

The Pennsylvania State University  
The Graduate School  
Department of Chemical Engineering

**SYNTHESIS AND CHARACTERIZATION OF POLYURETHANE IONOMERS**

A Dissertation in  
Chemical Engineering

by

Shih-Wa Wang

© 2011 Shih-Wa Wang

Submitted in Partial Fulfillment  
of the Requirements  
for the Degree of

Doctor of Philosophy

December 2011

The dissertation of Shih-Wa Wang was reviewed and approved\* by the following:

Ralph H. Colby  
Professor of Materials Science & Engineering and Chemical Engineering  
Thesis Advisor  
Chair of Committee

Janna Maranas  
Associate Professor of Chemical Engineering

Darrell Velegol  
Professor of Chemical Engineering

Melik C. Demirel  
Associate Professor of Engineering Science and Mechanics

James Runt  
Professor of Materials Science & Engineering

Andrew Zydney  
Walter L. Robb Chair and Professor of Chemical Engineering  
Head of the Department of Chemical Engineering

\*Signatures are on file in the Graduate School

## ABSTRACT

Applications such as lithium ion batteries and actuator membranes of ion-conducting polymers usually require both mechanical strength and ionic conductivity simultaneously. Throughout this thesis, PEO-based polyurethane ionomers are explored for achieving both good mechanical strength and high ionic conductivity. Polyurethane is an interesting material because it can have coexisting a mechanically strong hard phase and a fast relaxing soft phase, which can potentially have high conductivity. Anionic groups carboxylate and sulfonate are attached on the polyurethane chain either in the hard segment or soft segment to prepare single-ion conducting polyurethane ionomers that allow only cations to move under an applied electric field. Morphology, mechanical strength, ionic conductivity, thermal and dielectric properties are characterized to develop the structure-property relationships of these polyurethane ionomers.

Carboxylate-based polyurethane ionomers are prepared by using a low molar mass carboxylate diol that places the carboxylate groups in the hard segment. The effect of the counterions, from small sodium ions to large ionic liquid type counterions, is studied. It is found that with ionic groups in the hard segment, polyurethane ionomers do not microphase separate into hard and soft phases even with a 40wt% hard segment content. The glass transition temperature  $T_g$  decreases with increasing cation size because the distance between cation and anion increases and the Coulombic force decreases. The ionomers with lower  $T_g$  show a much higher ionic conductivity (up to 5 orders of magnitude) and the ionic conductivity is strongly coupled to polymer segmental relaxation. However, the modulus is also reduced because these ionomers do not

microphase separate and it is also found that more than 50% of the counterions are trapped in the hard segment and never conduct.

Polyurethane ionomers with sulfonate groups in the center of the soft segment are also synthesized by placing the sulfonate between poly(ethylene glycol) (PEG) spacers. It is found that with sulfonate groups in the soft segment and long enough PEG spacer ( $M_w > 600$ ), the polyurethane ionomers can microphase separate if there is more than 20wt% of hard segment, achieved by incorporating butane diol chain extender. The microphase separated ionomers are solids with modulus  $\sim$  MPa up to 200°C. We observe a lower soft phase  $T_g$  ( $\sim 5^\circ\text{C}$  independent of hard segment content) and higher ionic conductivity, are also detected compared to ionomers with carboxylate groups in the hard segment. The ionic conductivity is again found to strongly couple with polymer segmental relaxation. By placing the ionic groups in the soft segment, the problem of many ions being trapped in the hard segment is solved and all cations can respond to an applied electric field and contribute to ionic conductivity. Overall, the best ionomer obtained in this thesis has shear modulus of 4 MPa and ionic conductivity of  $2 \times 10^{-5}$  S/cm at 150 °C.

## TABLE OF CONTENTS

LIST OF FIGURES .....	vii
LIST OF TABLES .....	xi
ACKNOWLEDGEMENTS .....	xii
Chapter 1 Introduction .....	1
1.1 Motivation.....	1
1.2 Literature Review .....	3
1.2.1 Isocyanate chemistry .....	3
1.2.2 Strategies for polyurethane ionomer preparation .....	6
1.2.3 Morphology and glass transition .....	9
1.2.4 Mechanical properties .....	12
1.2.5 Dielectric properties and ionic conductivity.....	16
1.3 Hypothesis .....	16
1.4 References.....	17
Chapter 2 Counterion Dynamics in Polyurethane-Carboxylate Ionomers with Ionic Liquid Counterions .....	21
2.1 Introduction.....	21
2.2 Materials and experimental methods .....	23
2.2.1 Polyurethane and counterions synthesis and ionomers preparation .....	24
2.2.2 Experimental methods .....	27
2.3 Results and discussions.....	29
2.3.1 Glass Transition Temperature ( $T_g$ ).....	29
2.3.2 Rheology and morphology .....	33
2.3.3 Polymer Relaxation .....	36
2.3.4 Ionic conductivity.....	40
2.3.5 Electrode polarization (EP) .....	42
2.3.6 Concentrations of conducting ions and their mobility .....	46
2.3.7 Actuation and electrode polarization (EP) .....	49
2.3.8 EP model with Cole-Cole relaxation.....	53
2.4 Conclusion .....	57
2.5 References.....	59
Chapter 3 X-ray Scattering and Infrared Studies for Polyurethane Ionomers with Ions in the Hard Segment .....	62
3.1 Introduction.....	62
3.2 Materials and Experimental Methods.....	63
3.2.1 Materials .....	63

3.2.2 Experimental methods .....	64
3.3 Results and Discussions.....	65
3.3.1 X-ray scattering .....	65
3.3.2 Fourier transform infrared study (FTIR) .....	69
3.4 Summary and Future Work .....	75
3.5 Reference .....	76
Chapter 4 Structure-Property Relationship of Polyurethane Ionomers with Ions in the Soft Segment.....	79
4.1 Introduction.....	79
4.2 Materials and Experiment methods .....	81
4.2.1 Materials .....	81
4.2.2 Polyurethane (PU) ionomer synthesis .....	81
4.2.3 Experiment method .....	83
4.3 Results and Discussions.....	85
4.3.1 Chemical structure and thermal properties.....	85
4.3.2 Small angle X-ray scattering (SAXS) and morphology .....	87
4.3.3 Linear viscoelastic response .....	88
4.3.4 Dielectric relaxation spectroscopy (DRS) .....	93
4.4 Conclusion .....	111
4.5 References.....	112
Chapter 5 Microphase Separation in Polyurethane Ionomers.....	115
5.1 Introduction.....	115
5.2 Materials and Experimental Methods .....	116
5.2.1 Materials .....	116
5.2.2 Synthesis of polyurethane and polyester ionomers .....	117
5.2.3 Sample preparation and characterization.....	119
5.3 Results and Discussions.....	121
5.3.1 Thermal analysis and basic physical properties .....	121
5.3.2 Small angle X-ray scattering (SAXS) and morphology .....	123
5.3.3 Linear viscoelasticity.....	125
5.3.4 Dielectric properties and ionic conductivity.....	130
5.4 Conclusion .....	141
5.5 References.....	142
Chapter 6 Conclusion and Future Work .....	145
Appendix A NMR Spectra of Materials Prepared .....	153

## LIST OF FIGURES

Figure 1-1: Relationship between ionic conductivity and mechanical strength of PEO-based ion-containing homopolymers. ....	2
Figure 1-2: Reactions of isocyanate.....	4
Figure 1-3: Commonly used diisocyanate building blocks.....	5
Figure 1-4: Commonly used polyol building blocks. ....	6
Figure 1-5: Chemistry of attaching ionic groups to nitrogen on the urethane linkage.....	7
Figure 1-6: Examples of preparing ion-containing polyols .....	9
Figure 1-7: Hydrogen bonding in polyurethane ionomers.....	10
Figure 2-1: Chemical Structures of Polyurethane Anionomer and Cations Studied ...	24
Figure 2-2: $T_g$ from DSC as a function of (a) reciprocal size of corresponding acetate salts (assuming the same density $\rho$ of 1.0 g/cm <sup>3</sup> ) and (b) quadrupole energy at 0K in vacuum. Open symbols are cations containing ether oxygen .....	31
Figure 2-3: (a) Storage and loss modulus and $\tan \delta$ (solid curve) as function of $T/T_g$ at 1 rad/s. Dashed arrow indicates the shoulder of nonimidazolium ionomers. (b) Master curves of storage ( $G'$ , filled symbols) and loss ( $G''$ , open symbols) modulus as functions of frequency from time-temperature superposition of oscillatory shear data at various temperatures, shifted to $T_g + 30$ K. Inset: Cole-Cole plot of oscillatory shear data for all ionomers at various temperatures. ....	35
Figure 2-4: (a) Dielectric loss derivative spectra of $\text{Na}^+$ , $\text{Me}_4\text{N}^+$ , $(\text{EOc})_2\text{Me}(\text{MOE})\text{N}^+$ , $\text{Bu}_4\text{N}^+$ and $(\text{MOEOE})_3\text{MeN}^+$ ionomers at corresponding $T_g \pm 5$ K. Inset: Dielectric loss (solid symbol) and derivative (open symbol) spectra of $(\text{MOE})\text{MeIm}^+$ at $T_g$ (20 °C). (b) Dielectric loss derivative spectra of $\text{Na}^+$ , $\text{BuMeIm}^+$ , $(\text{MOE})\text{MeIm}^+$ , $\text{Bu}_4\text{P}^+$ and $\text{Bu}_3(\text{MOE})\text{P}^+$ at corresponding $T_g \pm 5$ K. ....	37
Figure 2-5: $\alpha$ -relaxation frequency as a function of temperature. Inset: $\alpha$ relaxation frequency as a function of $T_g$ normalized temperature. ....	39
Figure 3-1: Chemical structure of the neutral sample.....	63
Figure 3-2: Comparison of X-ray scattering spectra for neutral (black circle), acid form (light blue hexagon) and $\text{Na}^+$ (purple x) samples. ....	66

Figure 3-3: Spacing corresponding to the peak at $q \sim 7\text{nm}^{-1}$ .....	66
Figure 3-4: X-ray scattering spectra of $\text{Na}^+$ (purple x), $\text{Me}_4\text{N}^+$ (orange plus), $\text{MeBuIm}^+$ (cyan star), $\text{Bu}_4\text{N}^+$ (dark red diamond) and $\text{Bu}_4\text{P}^+$ (blue triangle) samples. ....	67
Figure 3-5: X-ray scattering spectra of $\text{Me}_4\text{N}^+$ (orange plus), $(\text{EOc})_2\text{Me}(\text{MOE})\text{N}^+$ (open green square), $\text{Bu}_4\text{N}^+$ (dark red diamond), $\text{Bu}_4\text{P}^+$ (blue triangle), $\text{Bu}_3(\text{MOE})\text{P}^+$ (olive green open triangle), and $(\text{MOEOE})_3\text{MeN}^+$ (red open circle) samples. ....	68
Figure 3-6: Linear scale wide angle X-ray scattering spectra.....	69
Figure 3-7: FTIR spectra of (from bottom to top) neutral (black), acid form (blue), $\text{Na}^+$ (purple), $\text{BuMeIm}^+$ (cyan) and $(\text{MOEOE})_3\text{MeN}^+$ (red) samples at $30^\circ\text{C}$ .....	70
Figure 3-8: Carbonyl stretching region of neutral (black), acid form (blue), $\text{Na}^+$ (purple), $\text{BuMeIm}^+$ (cyan) and $(\text{MOEOE})_3\text{MeN}^+$ (red) samples at $30^\circ\text{C}$ .....	71
Figure 3-9: N-H stretching region of neutral (black), acid form (blue), $\text{Na}^+$ (purple), $\text{BuMeIm}^+$ (cyan) and $(\text{MOEOE})_3\text{MeN}^+$ (red) samples at $30^\circ\text{C}$ .....	72
Figure 3-10: Ether group (C-O-C) region of neutral (black), acid form (blue), $\text{Na}^+$ (purple), $\text{BuMeIm}^+$ (cyan) and $(\text{MOEOE})_3\text{MeN}^+$ (red) samples at $30^\circ\text{C}$ .....	73
Figure 3-11: FTIR spectra of neutral sample from 30 to $100^\circ\text{C}$ at (a) N-H region and (b) C=O region.....	74
Figure 3-12: FTIR spectra of $\text{BuMeIm}^+$ sample from 25 to $100^\circ\text{C}$ at (a) N-H region and (b) C=O region.....	75
Figure 4-1: Chemical structure of SC-diols. In this chapter, n is 4, 9 or 13 with $M_n$ $= 248, 984$ or $1384$ .....	82
Figure 4-2: Chemical structure of SC-diol based polyurethane ionomers.....	83
Figure 4-3: Relationship between DSC $T_g$ and $\text{Na}^+/\text{EO}$ ratio.....	87
Figure 4-4: SAXS spectra of PU ionomers.....	88
Figure 4-5: Master curve of PU200s with $T_{\text{ref}} = 130^\circ\text{C}$ ( $T_g + 50^\circ\text{C}$ ). ....	90
Figure 4-6: Master curve of PU400s with $T_{\text{ref}} = 70^\circ\text{C}$ ( $T_g + 50^\circ\text{C}$ ). ....	91
Figure 4-7: Master curve of PU600s with $T_{\text{ref}} = 50^\circ\text{C}$ ( $T_g + 50^\circ\text{C}$ ). ....	92
Figure 4-8: Cole-Cole plot of $G'$ vs $G''$ of PU ionomers.....	92

Figure 4-9: Temperature step study for PU200s, PU400s, and PU600s at 1 rad/s. ....	93
Figure 4-10: Derivative spectra of (a) SC-diols; (b) PUs; (c) SC-diol600 based ionomers and PUD400 at $T_g + 20K$ . ....	95
Figure 4-11: Relaxation strength $\Delta\epsilon$ (Eq. 4-2) of $\alpha$ and $\alpha_2$ relaxation of polyurethane ionomers in this chapter and polyester sulfonate ionomers from ref <sup>42</sup> as a function cation/EO ratio. ....	97
Figure 4-12: (a) $\alpha$ and (b) $\alpha_2$ relaxation frequency as function of $T_g/T$ . ....	99
Figure 4-13: Molar ionic conductivity as function of (a) $1000/T$ and (b) $T_g/T$ . ....	103
Figure 4-14: Molar ionic conductivity as function of (a) $\alpha$ relaxation frequency and (b) $\alpha_2$ relaxation frequency. Inset: BNN plot of <i>molar conductance</i> as a function of $\Delta\epsilon_{\alpha}\omega_{\alpha}$ and <i>conductivity</i> as a function of $\Delta\epsilon_{\alpha_2}\omega_{\alpha_2}$ . ....	104
Figure 4-15: Temperature dependence of conducting ion concentration. ....	107
Figure 4-16: Relationship between activation energy and $Na^+/EO$ ratio. ....	108
Figure 4-17: (a) Temperature, (b) $\alpha$ relaxation and (c) $\alpha_2$ relaxation frequency dependence of cation mobility. ....	110
Figure 5-1: Chemical structure of SC-diol based PU ionomers. ....	118
Figure 5-2: Chemical structure of SC-diol based polyester ionomer. ....	118
Figure 5-3: DSC study for PU23 and PU32. ....	123
Figure 5-4: SAXS spectra of PU ionomer samples. Intensity was corrected by background and thickness. ....	125
Figure 5-5: Master curves of (a) PU10 ( $T_{ref} = 50^{\circ}C$ ), (b) PU23 and (c) PU32 with $T_{ref} = 60^{\circ}C$ . ....	127
Figure 5-6: Cole-Cole plot of (a) PU10 and (b) PU23 and PU32. ....	128
Figure 5-7: Dynamic temperature step study of PU ionomers at 1 rad/s. ....	129
Figure 5-8: (a) "Conduction-free" derivative spectra of ionomers with various hard segment content and sample preparation methods at $T = T_g + 20K (\pm 5K)$ . (b) Comparison of $\epsilon''$ and $\epsilon_{der}$ spectra and the best fit with power-law EP and two Havriliak-Nagami functions for hot pressed PU23 at $10^{\circ}C$ . ....	131
Figure 5-9: (a) $\alpha$ and (b) $\alpha^*$ relaxation frequency as a function of temperature. ....	133

Figure 5-10: (a) Ionic conductivity as a function of reciprocal temperature; (b) Molar conductivity as function of $\alpha$ -relaxation frequency.....	135
Figure 5-11: Normalized conducting ion concentration as a function of temperature. ....	138
Figure 5-12: Cation mobility as a function of $T_g/T$ . ....	140
Figure 6-1: Relationship between ionic conductivity and mechanical strength for PEO-based ion-containing homopolymers and PU23 and PU32 in Chapter 5. ....	147
Figure A-1: $^1\text{H-NMR}$ of sulfonated dimethyl fumarate in $\text{DMSO-d}_6$ . ....	153
Figure A-2: $^{13}\text{C-NMR}$ of sulfonated dimethyl fumarate in $\text{DMSO-d}_6$ . ....	154
Figure A-3: $^1\text{H-NMR}$ of SC-diol200 in $\text{DMSO-d}_6$ . ....	155
Figure A-4: $^{13}\text{C-NMR}$ of SC-diol200 in $\text{DMSO-d}_6$ . ....	155
Figure A-5: $^1\text{H-NMR}$ of SC-diol400 in $\text{DMSO-d}_6$ . ....	156
Figure A-6: $^{13}\text{C-NMR}$ of SC-diol400 in $\text{DMSO-d}_6$ . ....	156
Figure A-7: $^1\text{H-NMR}$ of SC-diol600 in $\text{DMSO-d}_6$ . ....	157
Figure A-8: $^{13}\text{C-NMR}$ of SC-diol600 in $\text{DMSO-d}_6$ . ....	157
Figure A-9: $^1\text{H-NMR}$ of PU200s in $\text{DMSO-d}_6$ . ....	158
Figure A-10: $^1\text{H-NMR}$ of PU400s in $\text{DMSO-d}_6$ . ....	158
Figure A-11: $^1\text{H-NMR}$ of PU600s/PU10 in $\text{DMSO-d}_6$ . ....	159
Figure A-12: $^1\text{H-NMR}$ of PU200sd400 in $\text{DMSO-d}_6$ . ....	159
Figure A-13: $^1\text{H-NMR}$ of PU600sd600 in $\text{DMSO-d}_6$ . ....	160
Figure A-14: $^1\text{H-NMR}$ of PUd400 in $\text{DMSO-d}_6$ . ....	160
Figure A-15: $^1\text{H-NMR}$ of PU23 in $\text{DMSO-d}_6$ . ....	161
Figure A-16: $^1\text{H-NMR}$ of PU32 in $\text{DMSO-d}_6$ . ....	161
Figure A-17: $^1\text{H-NMR}$ of PU40 in $\text{DMSO-d}_6$ . ....	162
Figure A-18: $^1\text{H-NMR}$ of PE in $\text{DMSO-d}_6$ . ....	162

## LIST OF TABLES

Table <b>1-1</b> : Examples of ion containing short diols (chain extenders) used in polyurethane ionomer synthesis that effectively place ions in the hard phase. ....	8
Table <b>1-2</b> : Literature glass transition temperature, mechanical strength and ionic conductivity data of various polyurethane ionomers.....	13
Table <b>2-1</b> : Cation-Anion Distance <sup>a</sup> , Glass Transition Temperature and Quadrupole Formation Energy $\Delta E_{\text{quadrupole}}$ <sup>b</sup> of the Ion Pair Calculated by ab initio at 0K in Vacuum. ....	27
Table <b>2-3</b> : Fitting Parameters for the Temperature Dependences of $\alpha$ -Relaxation Frequency (Eq. <b>2-2</b> ), Conducting Ion Content (Eq. <b>2-10</b> ) and Conducting Ion Mobility (Eq. <b>2-11</b> ).....	40
Table <b>2-4</b> : Summary of different methods to obtain conduction time scale and static dielectric constants .....	56
Table <b>4-1</b> : Basic physical properties of PU ionomers studied in this chapter. ....	85
Table <b>4-2</b> : Fitting parameters for the temperature dependence of $\alpha$ , $\alpha_2$ , and $\alpha_3$ relaxation frequency. ....	100
Table <b>4-3</b> : Fitting parameters for temperature dependence of conducting ion concentration (Eq. <b>4-11</b> ) and their mobility (Eq. <b>4-12</b> ). ....	107
Table <b>5-1</b> : Chemical composition of SC-diol based PU and polyester ionomers and their physical properties.....	121
Table <b>5-2</b> : Spacing between hard domains from SAXS. ....	125
Table <b>5-3</b> : VFT fitting parameters of $\omega_\alpha$ and $\omega_{\alpha^*}$ relaxations. ....	133
Table <b>5-4</b> : VFT fitting parameters of $\omega_\alpha$ and $\omega_{\alpha^*}$ relaxations with $T_0 = 202\text{K}$ . ....	134
Table <b>5-5</b> : Fitting parameters for conducting ion content (Eq. <b>5-11</b> ) and their mobility (Eq. <b>5-12</b> ). ....	139

## ACKNOWLEDGEMENTS

I thank my advisor Prof. Colby for all the direction and discussion. I thank Prof. Runt and Prof. Long for useful discussions. I also thank the group members for both a lot of help on research and friendship with especially thanks to Dr. Yanjie Wang, Dr. Wenjuan Liu and Dan King. Thank Dr. Jinqo Zhang, Dr. Sean Ramirez and Siwei Liang for advice in chemistry. Thank Dr. Wenqin (Sunny) Wang for taking X-ray spectra in Chapter 3. Thank Kyle Hart and Meredith Muskovich for taking FTIR data. Thank Matt Green for molecular weight determination. Thank all the friends in Steidle and Fenske.

I thank my husband Jack and my family in Taiwan. Without their understanding and absolute support, I will not be able to finish my degree. I also like to thank my guinea pigs Riceball and Teaegg for their company in my life in Penn State.

## Chapter 1

### Introduction

#### 1.1 Motivation

Since P. V Wright discovered the solvation ability of poly(ethylene oxide) (PEO) for alkali metal ions in 1973<sup>1</sup>, polymer electrolytes are believed to have great potential for flexible and easily processable ion conducting applications such as lithium ion batteries<sup>2-4</sup> and ionic actuators<sup>5</sup>. Generally, ionic conductivity in these polymer electrolyte systems is controlled by their glass transition temperature  $T_g$  and ion transport is strongly coupled to polymer segmental relaxation<sup>2, 6</sup>. From this point of view, the low  $T_g$  nature of PEO provides fast segmental relaxation for ion transport. However, PEO at the same time causes poor mechanical strength (as shown in Figure **1-1**), which is also very important in lithium ion batteries and actuators<sup>7</sup>. For a 10 $\mu$ m thick ( $d = 10\mu\text{m}$ ) actuator film operated under 4V with a 2 cm<sup>2</sup> cross section area and 10% strain, it requires 10<sup>-4</sup> S/cm for a response time of 2s (Eq. **1-1**;  $v$  is ion velocity,  $E$  is electric field,  $V$  is voltage,  $\mu$  is ion mobility and  $\sigma$  is ionic conductivity) and modulus of 5MPa to generate 1N force (Eq. **1-2**;  $\sigma_s$  is stress,  $A$  is cross section area,  $E$  is modulus and  $\epsilon$  is strain.). To achieve both good ionic conductivity and mechanical strength, crosslinked polymer gels and block copolymers are common solutions<sup>8-10</sup>.

$$t : \frac{d}{v} = \frac{d}{\mu E} = \frac{d^2}{\mu V} : \frac{1}{\mu} : \frac{1}{\sigma} \quad (1-1)$$

$$F : \sigma_s A : E \varepsilon \quad (1-2)$$

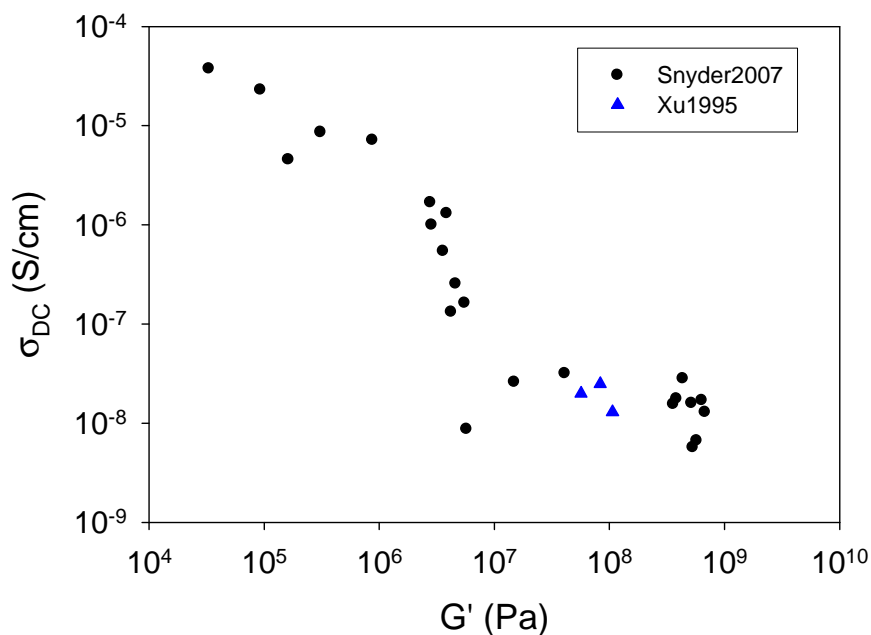


Figure 1-1: Relationship between ionic conductivity and mechanical strength of PEO-based ion-containing homopolymers.<sup>7,11</sup>

Here, instead of crosslinked gel or block copolymers, polyurethane ionomers are proposed as an alternative solution. The urethane linkage in polyurethane, which is both a hydrogen bonding donor and acceptor, can act as a physical crosslink and help polyurethane to microphase separate into hard and soft domains. With microphase separation, the high  $T_g$  hard phase can provide good mechanical strength while the soft phase still has low  $T_g$  and potentially good conductivity. In this thesis, polyurethane ionomers with various ionic groups in both hard segment and soft segment were synthesized and their structure-property relationships with a variety of counterions will be discussed.

## 1.2 Literature Review

### 1.2.1 Isocyanate chemistry

Polyurethanes can be prepared by reacting diisocyanate and polyol (diol) with or without catalyst, depending on the reactivity of the diisocyanate and polyol used. Besides hydroxyl group, isocyanate can also react with other functional groups containing active protons such as amines to make polyureas. The chemical reactions involving isocyanate are summarized in Figure 1-2<sup>12-16</sup>. The reactivity depends strongly on the type of the active proton, structures of both R and R'. Generally, the reactivity is as following: amines >> alcohols ~ water >> carboxylic acids > thiols ~ phenols. For R', steric hindrance also plays an important role: aliphatic amine >> aromatic amine > 1° alcohol > 2° alcohol and the reactions with 3° alcohol usually do not happen.<sup>17, 18</sup> Note that the reactivity between isocyanate and water (producing urea) is very similar to that of isocyanate and alcohol (producing urethane). This fact makes the synthesis of pure polyurethane very sensitive to the presence of moisture in polyols, solvents, reactors and atmosphere, often resulting in low molecular weight from stoichiometric imbalance in this polycondensation reaction. Generally, a slight excess of isocyanate charged to the reaction, especially in large scale synthesis, is a very common procedure to deal with this issue.

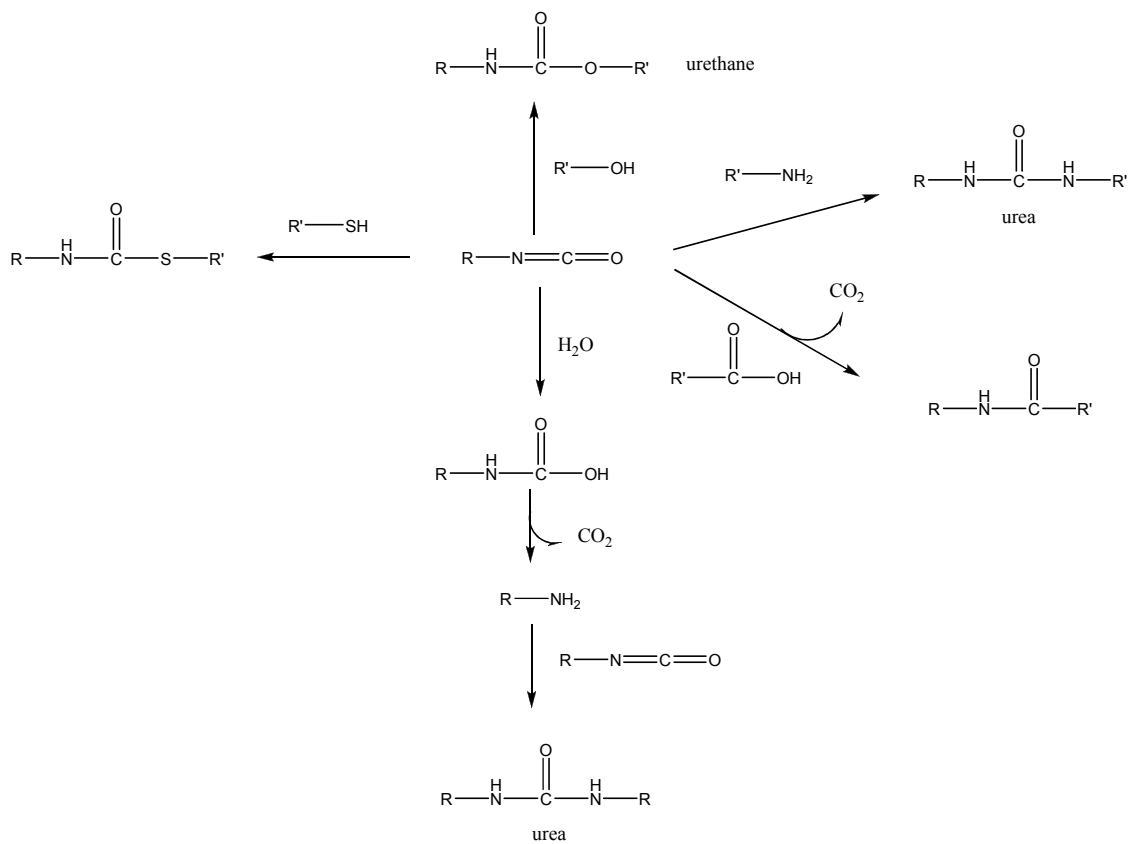


Figure 1-2: Reactions of isocyanate.<sup>12-16</sup>

---

Based on the desired properties, various diisocyanates and polyols can be used. Figure 1-3 and Figure 1-4 show some commonly used diisocyanates and polyols. Polyurethanes can be made to be very soft or hard as a rock, depending on their chemical makeup.

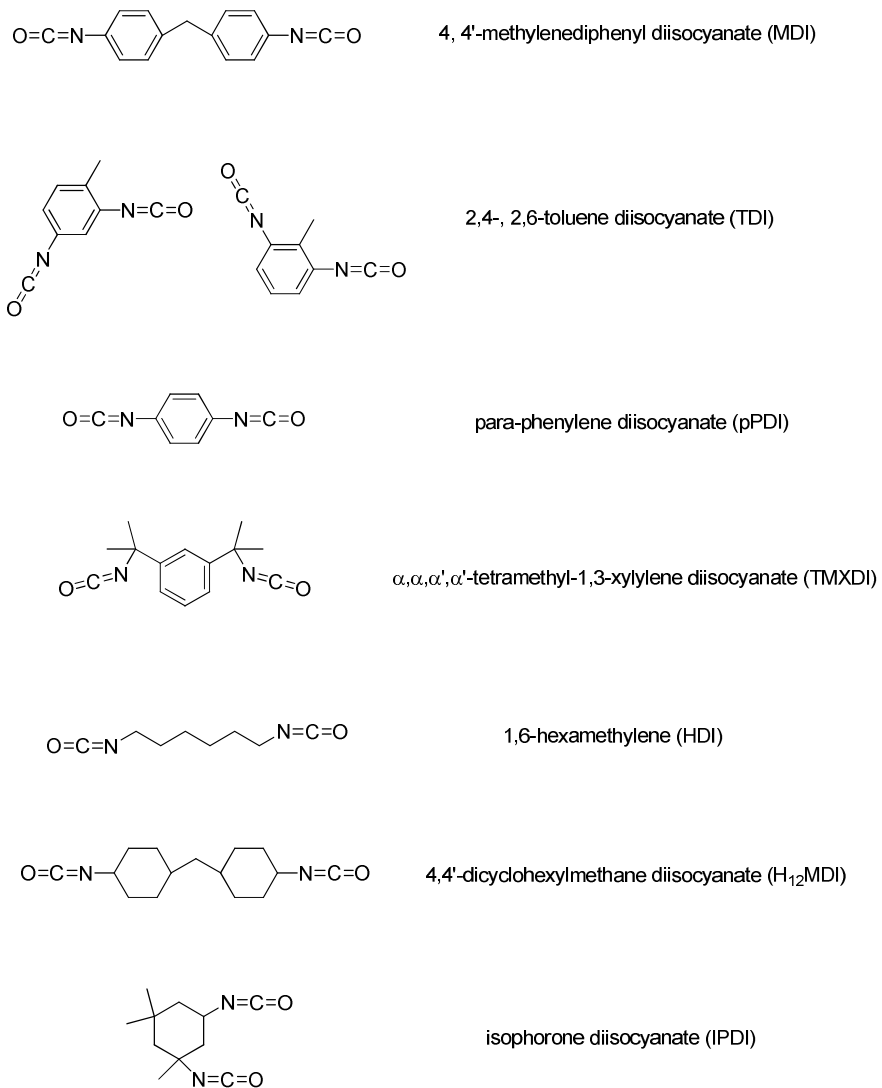


Figure 1-3: Commonly used diisocyanate building blocks.

---

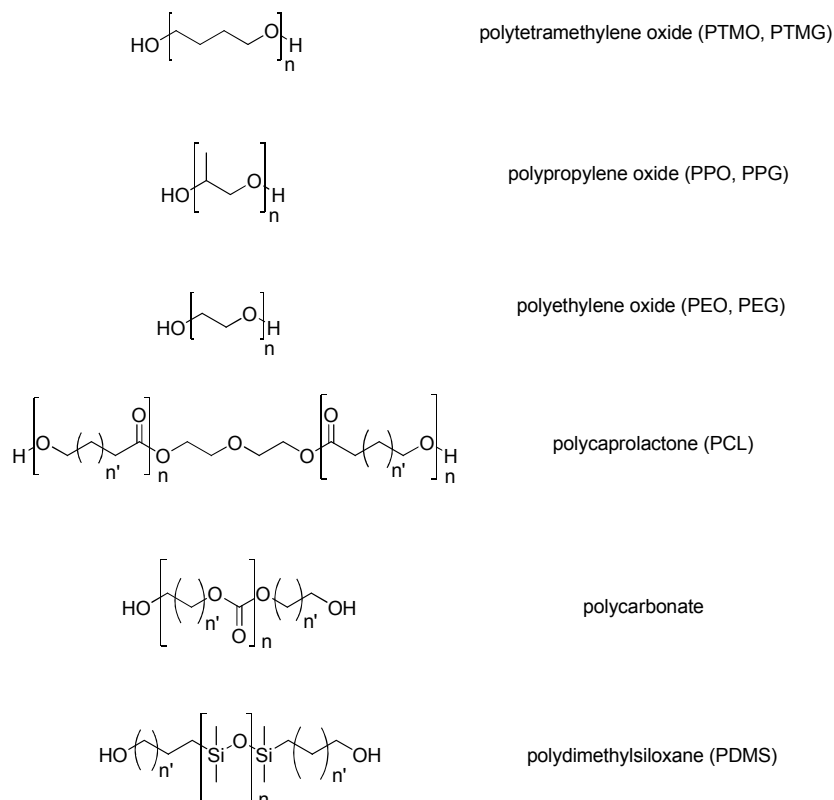


Figure 1-4: Commonly used polyol building blocks.

---

### 1.2.2 Strategies for polyurethane ionomer preparation

Various methods for polyurethane ionomer synthesis have been developed that utilize different chemistry. Here, these methods are categorized into three groups based on where the ionic groups are placed.

**A. Modifying the urethane linkage with an ionic group.** This method involves post-polymerization modification of the urethane linkage, after a neutral polyurethane was made. The chemistry is shown in Figure 1-5.<sup>19-21</sup> Attention should be taken that this method removes the proton on the nitrogen, which is a hydrogen bond donor and plays an important role in microphase separation into hard and soft phases. Polyurethane ionomers

prepared by this method may still show ion aggregates but are less likely to have good microphase separation between hard and soft phases.<sup>22, 23</sup>

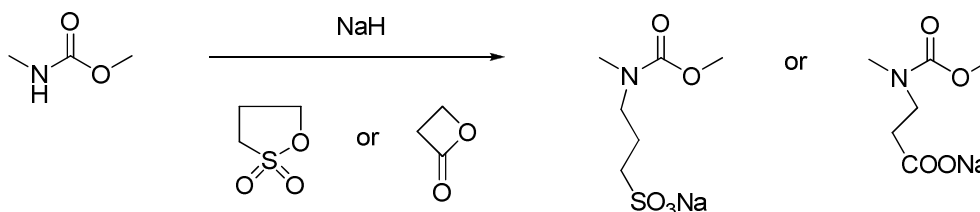
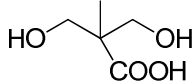
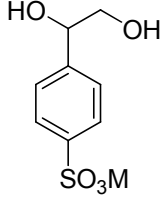
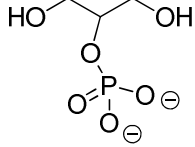
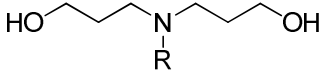
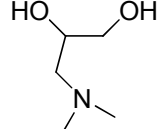


Figure 1-5: Chemistry of attaching ionic groups to nitrogen on the urethane linkage.

---

**B. Attaching ionic group in the hard segment by using an ion containing chain extender (short ionic diol).** This may be the easiest method to incorporate ionic groups into polyurethanes. By this method, it is possible to prepare polyurethane anionomer, cationomer and zwitterionomers with good control of ion content.<sup>24, 25</sup> Table 1-1 gives some examples of ion containing diols that can be used for polyurethane ionomer synthesis. Besides diols, short ion-containing diamines are also used for polyurethane-urea ionomer synthesis.

Table 1-1: Examples of ion containing short diols (chain extenders) used in polyurethane ionomer synthesis that effectively place ions in the hard phase.

Structure	Reference
	26-28
	29
	30
	23, 31, 32
	33

\*Tertiary amine containing diols are usually first reacted with diisocyanate producing a neutral polyurethane and then further quaternized to prepare cationomer or zwitterionomer (with negatively charged quaternization agent).

**C. Attaching ionic group in the soft segment by preparing ion containing polyols (long ionic diol).** Instead of using a short ion-containing diol, this method utilizes long ion-containing diol (polyol). Compared to short ion-containing diols, ion containing polyols are much less common and there are none commercially available. The simplest method to prepare ion-containing polyols is utilizing ionic diesters to connect two polyol molecules with the ion-containing group at the center.<sup>34-39</sup> The chemistry is shown in Figure 1-6. Since polyurethane is synthesized through polycondensation process, accurate stoichiometry between hydroxyl (from both polyols and chain extenders) and isocyanate groups is crucial for product molecular weight.

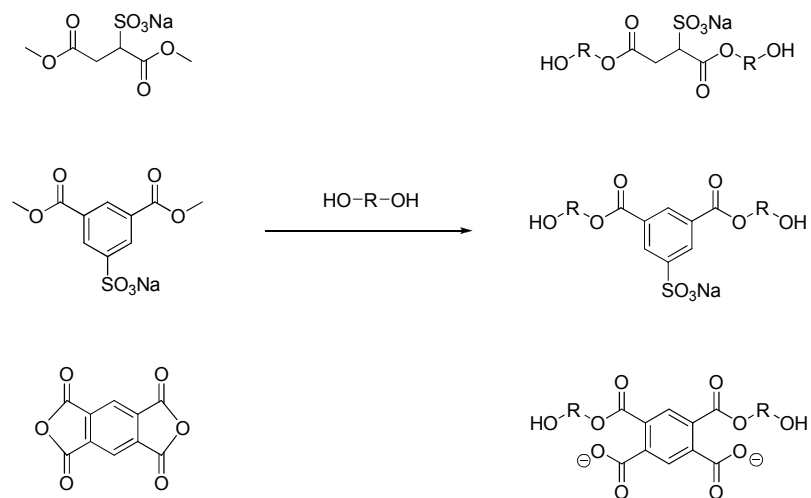


Figure 1-6: Examples of preparing ion-containing polyols.<sup>34, 36, 38</sup>

---

### 1.2.3 Morphology and glass transition

Urethane linkages tend to hydrogen bond to each other and promote microphase separation. However, urethane linkages can also interact with other groups (Figure 1-7) in the polymer and the microphase separation is usually not complete. Various techniques have been used to characterize polyurethane morphology. Directly investigating the presence of microphases can be done by X-ray scattering<sup>40-43</sup>, AFM<sup>44, 45</sup> and TEM<sup>46, 47</sup>. FTIR is generally used to probe hydrogen bonding which is the driving force for microphase separation.<sup>48, 49</sup> Glass transition of hard and soft phases can be found by DSC<sup>50</sup> and DMA<sup>45</sup>. Linear viscoelasticity is very sensitive to the local microphase structure in polymers and very useful to show evidence of microphase separation.<sup>51, 52</sup>

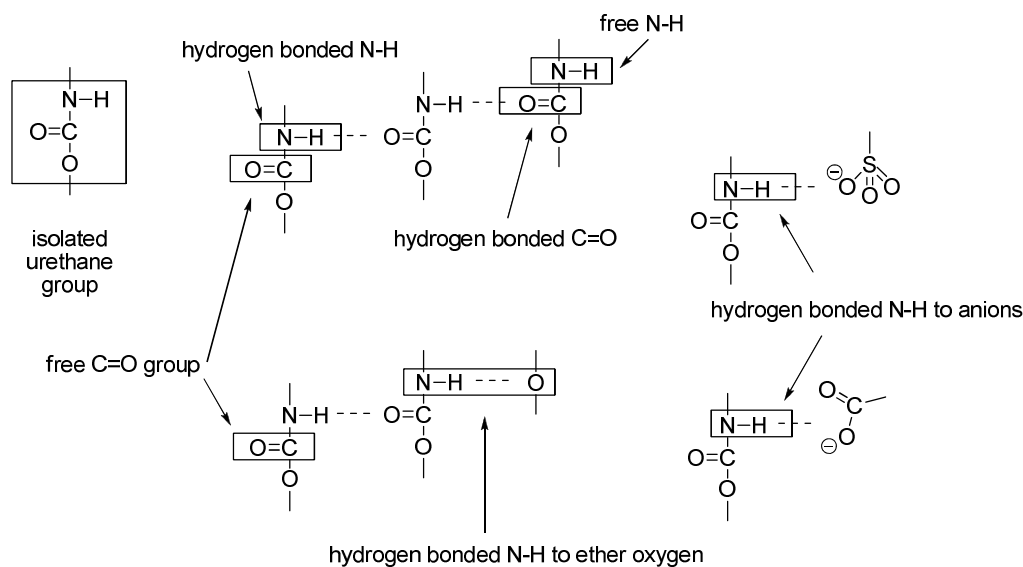


Figure 1-7: Hydrogen bonding in polyurethane ionomers.<sup>22, 48</sup>

For neutral polyurethanes, microphase separation between hard and soft segment is basically controlled by the symmetry of the diisocyanate, the hard segment content and its compatibility with the soft segment. Generally, more symmetric diisocyanate and higher hard segment content leads to better microphase separation.<sup>49, 53-55</sup> For the soft segment, the polyol type is the most important aspect, while the length<sup>51</sup> can sometimes have significant influence. Polyols containing ether oxygen, which can act as hydrogen bond acceptor, or other functional groups that interact with the urethane linkage, tend to interrupt hydrogen bonding between hard segments and reduce microphase separation.<sup>48, 56-58</sup> Besides effects of the chemical structure, it was also found that kinetic factors are very critical in microphase separation,<sup>59, 60</sup> there is no such thing as an equilibrium microphase structure for this class of materials.

The presence of ions makes the system even more complicated and the effect on morphology strongly depends on chemical composition. For PEO-based polyurethane ionomers, due to the strong interaction of PEO with both urethane linkages and ions,

more hard and soft phase mixing, fewer ion aggregates and increased  $T_g$  are usually observed with increasing ion content.<sup>11,28, 61-63</sup> On the other hand, hard/soft microphase separation may be reduced by the presence of ions in PTMO-based polyurethanes but ion aggregates were usually observed because PTMO does not solvate cations as well as PEO. Both Cooper and Pissis groups found that the scattering in SAXS studies are mainly from ion aggregates instead of hard/soft microphase separation.<sup>21, 27, 36, 42, 43</sup> Meanwhile, better phase mixing between hard and soft segment happens for anions competing for hydrogen bonds to the urethane linkage<sup>21,22</sup> or steric hindrance from large ionic groups in the hard segment<sup>64</sup>.

Visser and Cooper reported that both morphology and  $T_g$  are mainly controlled by the nature of the soft segment. The effect of anion type is relatively minor but shows a trend of ionomers having slightly more ion aggregates and lower  $T_g$  with sulfonate groups than with carboxylate groups.<sup>20, 65</sup> Yu reported that the presence of ions always helps hard and soft segment mixing but placing ions in the soft segment (type C in previous section) improves phase mixing compared to placing ions in the hard segment (type B).<sup>66, 67</sup> As for the type of counterions, Al-Salah et al<sup>26</sup> reported  $T_g$  is proportional to (counterion charge/distance between cation and anion) as reported in other ionomers by Eisenberg.<sup>68, 69</sup> However, there are also other literature that report  $T_g$  is almost independent of counterion type.<sup>19, 27, 70</sup> In these papers, strong ion aggregates were found (no ion aggregates discussion in Chen et al<sup>70</sup> but polysiloxane is generally considered hydrophobic and incompatible with metal salts) so we can expect that only a small amount of ions are dissolved in the soft segment (or soft phase if there is microphase separation) making  $T_g$  relatively independent of ion size/type. Unfortunately, Al-Salah et

al did not report the morphology but it is more likely that there are more ions dissolved in their soft phase so  $T_g$  is more sensitive to ion size/type. However, soft segment type is still the main factor determining  $T_g$  of the soft phase.

#### **1.2.4 Mechanical properties**

Hydrogen bonds between hard segments act as physical crosslinks and make the hard phase have high  $T_g$  and high modulus, so the mechanical properties of polyurethane strongly depends on the morphology. Besides microphase separation between hard and soft phase, crystallinity of both hard and soft phases also helps in improving mechanical strength.<sup>53</sup> Table **1-2** summarizes some literature data of various polyurethane ionomers. It is clear that  $T_g$  does not decide the mechanical strength since most of the time,  $T_g$  measured by DSC is of the soft phase, which is not the phase controlling mechanical strength. The hard phase  $T_g$  is often not seen/reported by DSC. The general trend is that the presence of ions helps to improve mechanical strength from the Coulombic interaction between ions acting as physical crosslinks, if there is no significant change in morphology.

Table 1-2: Literature glass transition temperature, mechanical strength and ionic conductivity data of various polyurethane ionomers.

Diisocyanate	Polyol <sup>1</sup>	HS content <sup>2</sup> (wt%)	Ion attach method <sup>3</sup>	Fixed ion	Counterion (wt%)	T <sub>g</sub> (°C) <sup>4</sup>	Young's modulus (MPa) <sup>5</sup>	E' (MPa) <sup>5</sup>	σ (μS/cm) <sup>6</sup>	Ref
TDI	PTMO	32	A	-SO <sub>3</sub> <sup>-</sup>	Na <sup>+</sup> (1.35)	-68	25			19
		41			Cs <sup>+</sup> (1.18)	-69	3			
		34			Ca <sup>2+</sup> (0.68)	-70	23			
		36			Zn <sup>2+</sup> (0.67)	-69	8.6			
	PPO	19	A	-SO <sub>3</sub> <sup>-</sup>	Na <sup>+</sup> (0.81)	-61*	20			
MDI	PTMO	41	A	-SO <sub>3</sub> <sup>-</sup>	Na <sup>+</sup> (1.29)	-52		140		21
		33			(1.11)	-71		100		
		21			(0.77)	-78		29		
		15			(0.56)	-78		18		
MDI	PEO	43	A	-SO <sub>3</sub> <sup>-</sup>	Na <sup>+</sup> (0.57)	-14	170		0.020	11
		44			(0.67)	-12	250		0.025	
		48			(1.05)	-3	320		0.013	
MDI	PTMO	48	Neutral	-SO <sub>3</sub> <sup>-</sup>	(0)	-30	30			22
		49	A		Na <sup>+</sup> (0.15)	-24	27			
		50			(0.30)	-28	29			
		51			(0.44)	-36	31			
		52			(0.54)	-44	150			
MDI	PTMO	48	Neutral	-SO <sub>3</sub> <sup>-</sup>	(0)	-46	21			61
		52	A		Na <sup>+</sup> (0.57)	-46	130			
	PEO	48	Neutral		(0)	-23	23			
		52	A		Na <sup>+</sup> (0.57)	6	2.1			
TDI	PTMO	31	A	-SO <sub>3</sub> <sup>-</sup>	Na <sup>+</sup> (1.30)		54			20
		27		-COO <sup>-</sup>	Na <sup>+</sup> (1.45)		56			
	PPO	31		A	-SO <sub>3</sub> <sup>-</sup>		Na <sup>+</sup> (1.31)			

	PEO	25 32 26	A	-COO <sup>-</sup> -SO <sub>3</sub> <sup>-</sup> -COO <sup>-</sup>	Na <sup>+</sup> (1.33) Na <sup>+</sup> (1.37) Na <sup>+</sup> (1.42)		4.8 21 Too weak			
MDI	PTMO	50 50 51 52	B	-COO <sup>-</sup>	H <sup>+</sup> Li <sup>+</sup> (0.97) Na <sup>+</sup> (0.96) K <sup>+</sup> (0.94)	1 -51 -52 -51	7.5 190 170 170			27
IPDI	PEO	20  34 52	B	-COO <sup>-</sup> & -SO <sub>3</sub> <sup>-</sup>	Li <sup>+</sup> (0.26)  (1.00) (1.20)	-55  -50 -50			0.4 0.5 0.6	28
MDI	PCL	30 30	B	-COO <sup>-</sup>	H <sup>+</sup> TEA <sup>+</sup> (0.29)		210 270			71
MDI	PECH <sup>7</sup>	35 38	Neutral B		(0) Na <sup>+</sup> (0.78)	32 47		500 1000		72
MDI	PEO	49 40 30	C	-SO <sub>3</sub> <sup>-</sup>	Na <sup>+</sup> (0.52) (0.43) (0.32)	6 -7 -30			0.0224 0.227 1.02	73
MDI	PEO	22 22	C	-COO <sup>-</sup>	H <sup>+</sup> Na <sup>+</sup> (0.48)				0.76 0.27	62
	PTMO	22 22	C	-COO <sup>-</sup>	H <sup>+</sup> Na <sup>+</sup> (0.48)				0.08 0.0025	
MDI	PEO	7.5 16 22	C	-COO <sup>-</sup>	Na <sup>+</sup> (0.55) (0.50) (0.46)	-44 -44 -28			0.13 0.044 0.27	63
	PTMO	11 22	C	-COO <sup>-</sup>	Na <sup>+</sup> (0.76) (0.67)	-67 -59			0.04 0.00075	
MDI	PTMO	20 28 35	C	-COO <sup>-</sup>	Na <sup>+</sup> (0.68) (0.61) (0.55)	-59 -55 -59			0.011 0.0022 0.00065	37

		45			(0.47)	-55			0.00015	
IPDI	PEO	14	C	-PhSO <sub>3</sub> <sup>-</sup>	Li <sup>+</sup> (0.61)	-20			0.03	34
		13			Na <sup>+</sup> (0.60)	-16			0.06	

<sup>1</sup>See Figure 1-3.

<sup>2</sup>Hard segment content.

<sup>3</sup>See section 1.2.2.

<sup>4</sup>Measured by DSC. Soft phase T<sub>g</sub> if microphase separated. (\*Measured by DMA)

<sup>5</sup>At room temperature.

<sup>6</sup>Ionic conductivity at room temperature.

<sup>7</sup>PECH: poly(epoxy chloropropane)

---

### 1.2.5 Dielectric properties and ionic conductivity

Compared to studies on mechanical properties, studies on ionic conductivity are scarce. Most of them have ionic conductivity less than 1  $\mu\text{S}/\text{cm}$  near room temperature. Very few papers discuss both mechanical strength and ionic conductivity. Xu and Yang<sup>11</sup> report a PEO-based  $\text{NaSO}_3$  system with 250 MPa and  $2.5 \times 10^{-8}$  S/cm at room temperature.

Besides ionic conductivity, dielectric relaxation spectroscopy (DRS) has been applied to study dielectric properties of polyurethane ionomers. DRS can be used for probing polymer relaxation as well as ion polarization (which is related to ion state and transport).<sup>34, 36, 74</sup> Microphase separated polyurethanes can have an extra Maxwell-Wagner-Sillars (MWS) interfacial polarization originating from different mobility of ions (impurities if neutral polyurethanes) in hard and soft phases.<sup>75, 76</sup> Unfortunately, MWS in polyurethane can sometimes overlap with the  $\alpha$  relaxation and the two are difficult to separate.<sup>77, 78</sup> For these cases, thermally stimulated depolarization current (TSDC) measurements may be a better tool for clear distinguishing between MWS and other relaxations.<sup>74, 79, 80</sup>

### 1.3 Hypothesis

This literature review suggests that microphase separation of polyurethane can show good mechanical strength through hydrogen bonded hard phase while keeping a low  $T_g$  soft phase. The hypothesis of this thesis is that by tailoring the composition of

polyurethane ionomers, a polymeric material, with both good mechanical strength from the hard phase and good ionic conductivity through the soft phase, can be prepared for actuator or lithium ion battery applications.

#### 1.4 References

1. Fenton, D. E.; Parker, J. M.; Wright, P. V. *Polymer* **1973**, 14, 589.
2. Meyer, W. H. *Advanced Materials* **1998**, 10, (6), 439-448.
3. Quartarone, E.; Mustarelli, P.; Magistris, A. *Solid State Ionics* **1998**, 110, 1-14.
4. Goodenough, J. B.; Kim, Y. *Chemistry of Materials* **2010**, 22, 587-603.
5. Shahinpoor, M.; Bar-Cohen, Y.; Simpson, J. O.; Smith, J. *Smart Materials and Structures* **1998**, 7, (6), R15-R30.
6. Borodin, O.; Smith, G. D. *Macromolecules* **2006**, 39, 1620-1629.
7. Snyder, J. F.; Carter, R. H.; Wetzel, E. D. *Chemistry of Materials* **2007**, 19, 3793-3801.
8. Stephens, P. J.; Devlin, F. J.; Chabalowski, C. F.; Frisch, M. J. *Journal of Physical Chemistry* **1994**, 98, (45), 11623-11627.
9. Song, J. Y.; Wang, Y. Y.; Wan, C. C. *Journal of Power Sources* **1999**, 77, 183-197.
10. Gomez, E. D.; Panday, A.; Feng, E. H.; Chen, V.; Stone, G. M.; Minor, A. M.; Kisielowski, C.; Downing, K. H.; Borodin, O.; Smith, G. D.; Balsara, N. P. *Nano Letters* **2009**, 9, (3), 1212-1216.
11. Xu, H.-S.; Yang, C.-Z. *Journal of Polymer Science: Part B: Polymer Physics* **1995**, 33, 745-751.
12. Sorenson, W. R. *Journal of Organic Chemistry* **1959**, 24, (7), 978-980.
13. Xiao, H.; Xiao, H. X.; Frisch, K. C.; Malwitz, N. *High Performance Polymers* **1994**, 6, 235-239.
14. Satchell, D. P. N.; Satchell, R. S. *Chemical Society Reviews* **1975**, 4, 231-250.
15. Saunders, J. H.; Slocombe, R. J. *Chemical Reviews* **1948**, 43, (2), 203-218.
16. Arnold, R. G.; Nelson, J. A.; Verbanc, J. J. *Chemical Reviews* **1957**, 57, (1), 47-76.
17. Pannone, M. C.; Macosko, C. W. *Journal of Applied Polymer Science* **1987**, 34, (7), 2409-2432.
18. Rand, L.; Thir, B.; Reegen, S. L.; Frisch, K. C. *Journal of Applied Polymer Science* **1965**, 9, 1787-1795.
19. Ding, Y. S.; Register, R. A.; Yang, C.-z.; Cooper, S. L. *Polymer* **1989**, 30, 1204-1212.
20. Visser, S. A.; Cooper, S. L. *Macromolecules* **1991**, 24, 2576-2583.
21. Lee, D.-C.; Register, R. A.; Yang, C.-Z.; Cooper, S. L. *Macromolecules* **1988**, 21, 1005-1008.

22. Grasel, T. G.; Cooper, S. L. *Journal of Biomedical Materials Research* **1989**, 23, (3), 311-338.
23. Hwang, K. K. S.; Speckhard, T. A.; Cooper, S. L. *Journal of Macromolecular Science - Physics* **1984**, B23, 153-174.
24. Ramesh, S.; Radhakrishnan, G. *Journal of polymer materials* **1999**, 16, (2), 135-153.
25. George, M. H.; Arshady, R.; Kakati, D. K.; Al-Shahib, W.; Gosain, R., Polyurethane ionomers. In *Polymeric Materials Encyclopedia*, CRC Press, Inc.: 1996; pp 6968-6979.
26. Al-Salah, H. A.; Frisch, K. C.; Xiao, H. X.; Jr., J. A. M. *Journal of Polymer Science: part A: Polymer Chemistry* **1987**, 25, 2127-2137.
27. Yang, C.-Z.; Grasel, T. G.; Bell, J. L.; Register, R. A.; Cooper, S. L. *Journal of Polymer Science: part B: Polymer Physics* **1991**, 29, 581-588.
28. Wen, T.-C.; Wang, Y.-J.; Cheng, T.-T.; Yang, C.-H. *Polymer* **1999**, 40, 3979-3988.
29. Lam, P. K. H.; George, M. H.; Barrie, J. A. *Polymer* **1989**, 30, (12), 2320-2323.
30. Kakati, D. K.; George, M. H. *Polymer* **1993**, 34, (20), 4319-4324.
31. Dieterich, D.; Keberle, W.; Witt, H. *Angewandte Chemie International Edition* **1970**, 9, (1), 40-50.
32. Chen, S.-A.; Chan, W.-C. *Journal of Polymer Science: Part B: Polymer Physics* **1990**, 28, (9), 1499-1514.
33. Goddard, R. J.; Cooper, S. L. *Macromolecules* **1995**, 28, 1401-1406.
34. Fragiadakis, D.; Dou, S.; Colby, R. H.; Runt, J. *Macromolecules* **2008**, 41, 5723-5728.
35. Wei, X.; Yu, X. *Journal of Polymer Science: part B: Polymer Physics* **1997**, 35, 225-232.
36. Shilov, V. V.; Shevchenko, V. V.; Pissis, P.; Kyritsis, A.; Georgoussis, G.; Gomza, Y. P.; Nesin, S. D.; Klimenko, N. S. *Journal of Non-Crystalline Solids* **2000**, 275, 116-136.
37. Shilov, V. V.; Shevchenko, V. V.; Pissis, P.; Kyritsis, A.; Georgoussis, G.; Gomza, Y. P.; Nesin, S. D.; Klimenko, N. S. *Molecular Crystals and Liquid Crystals* **2001**, 361, 269-274.
38. Wang, X.; Li, H.; Tang, X.; Chang, F.-C. *Journal of Polymer Science Part B- Polymer Physics* **1999**, 37, 837-845.
39. Bao, L.-H.; Lan, Y.-J.; Zhang, S.-F. *Journal of Polymer Research* **2006**, 13, 507-514.
40. Bonart, R.; Muller, E. H. *Journal of Macromolecular Science, Physics* **1974**, B10, (1), 177-189.
41. Bonart, R.; Muller, E. H. *Journal of Macromolecular Science - Physics* **1974**, B10, (2), 345-357.
42. Ding, Y. S.; Register, R. A.; Yang, C. Z.; Cooper, S. L. *Polymer* **1989**, 30, (7), 1213-1220.
43. Lee, D.-C.; Register, R. A.; Yang, C.-Z.; Cooper, S. L. *Macromolecules* **1988**, 21, 998-1004.

44. Sheth, J. P.; Klinedinst, D. B.; Pechar, T. W.; Wilkes, G. L.; Yilgor, E.; Yilgor, I. *Macromolecules* **2005**, 38, (24), 10074-10079.
45. Choi, T.; Weksler, J.; Padsalgikar, A.; Runt, J. *Polymer* **2009**, 50, 2320-2327.
46. Li, C.; Cooper, S. L. *Polymer* **1990**, 31, (1), 3-7.
47. Taylor, F. E.; Laity, P. R.; Wong, S. S.; Norris, K.; Khunkamchoo, P.; Cable, M.; Andrews, G.; Johnson, A. F.; Cameron, R. E. *Microscopy and Microanalysis* **2006**, 12, (2), 151-155.
48. Coleman, M. M.; Skrovanek, D. J.; Hu, J.; Painter, P. C. *Macromolecules* **1988**, 21, 59-65.
49. Yilgor, I.; Yilgor, E.; Guler, I. G.; Ward, T. C.; Wilkes, G. L. *Polymer* **2006**, 47, (11), 4105-4114.
50. Kazmierczak, M. E.; Fornes, R. E.; Buchanan, D. R.; Gilbert, R. D. *Journal of Polymer Science Part B-Polymer Physics* **1989**, 27, (11), 2189-2202.
51. Velankar, S.; Cooper, S. L. *Macromolecules* **1998**, 31, 9181-9192.
52. Velankar, S.; Cooper, S. L. *Macromolecules* **2000**, 33, 395-403.
53. Sheth, J. P.; Klinedinst, D. B.; Wilkes, G. L.; Yilgor, I.; Yilgor, E. *Polymer* **2005**, 46, 7317-7322.
54. Blackwell, J.; Nagarajan, M. R.; Hoitink, T. B. *Polymer* **1982**, 23, (7), 950-956.
55. Leung, L. M.; Koberstein, J. T. *Macromolecules* **1986**, 19, 706-713.
56. Lee, D. W.; Lee, S. H.; Kim, S. C.; Char, K. H.; Park, J. H.; Bae, Y. H. *Journal of Polymer Science Part B-Polymer Physics* **2003**, 41, (20), 2365-2374.
57. Bogart, J. W. C. V.; Bluemke, D. A.; Cooper, S. L. *Polymer* **1981**, 22, 1428-1438.
58. Hernandez, R.; Weksler, J.; Padsalgikar, A.; Choi, T.; Angelo, E.; Lin, J. S.; Xu, L. C.; Siedlecki, C. A.; Runt, J. *Macromolecules* **2008**, 41, (24), 9767-9776.
59. Chu, B.; Gao, T.; Li, Y.; Wang, J.; Desper, C. R.; Byrne, C. A. *Macromolecules* **1992**, 25, 5724-5729.
60. Li, Y.; Gao, T.; Chu, B. *Macromolecules* **1992**, 25, 1737-1742.
61. Silver, J. H.; Marchant, J. W.; Cooper, S. L. *Journal of Biomedical Materials Research* **1993**, 27, (11), 1443-1457.
62. Polizos, G.; Kyritsis, A.; Pissis, P.; Shilov, V. V.; Shevchenko, V. V. *Solid State Ionics* **2000**, 136, 1139-1146.
63. Polizos, G.; Georgoussis, G.; Kyritsis, A.; Shilov, V. V.; Shevchenko, V. V.; Gomza, Y. P.; Nesin, S. D.; Klimenko, N. S.; Wartewig, S.; Pissis, P. *Polymer International* **2000**, 49, 987-992.
64. Williams, S. R.; Wang, W.; Winey, K. I.; Long, T. E. *Macromolecules* **2008**, 41, 9072-9079.
65. Visser, S. A.; Cooper, S. L. *Polymer* **1992**, 33, (18), 3790-3796.
66. Chen, H.; Chen, D.; Fan, Q.; Yu, X. *Journal of Applied Polymer Science* **2000**, 76, 2049-2056.
67. Wei, X.; He, Q.; Yu, X. *Journal of Applied Polymer Science* **1998**, 67, 2179-2185.
68. Eisenberg, A. *Macromolecules* **1971**, 4, (1), 125-128.
69. Eisenberg, A.; Kim, J.-S., *Introduction to Ionomers*. Wiley-Interscience: 1998.
70. Chen, L.; Yu, X.; Yang, C.-Z. *Chinese Journal of Polymer Science* **1996**, 14, (4), 295-303.

71. Kim, B. K.; Lee, S. Y.; Lee, J. S.; Baek, S. H.; Choi, Y. J.; Lee, J. O.; Xu, M. *Polymer* **1998**, 39, (13), 2803-2808.
72. Ding, J.; Xue, G.; Yang, C.; Chen, R. *Journal of Applied Polymer Science* **1992**, 45, 1087-1092.
73. Wang, X. L.; Wang, L.; Li, H.; Tang, X. Z.; Chang, F. C. *Journal of Applied Polymer Science* **2000**, 77, (1), 184-188.
74. Pissis, P.; Polizos, G., Molecular dynamics and ionic conductivity studies in polyurethane thermoplastic elastomers. In *Handbook of condensation thermoplastic elastomers*, Fakirov, S., Ed. Wiley-VCH: 2005; pp 381-429.
75. North, A. M.; Reid, J. C.; Shortall, J. B. *European Polymer Journal* **1969**, 5, 565-573.
76. North, A. M.; Reid, J. C. *European Polymer Journal* **1972**, 8, 1129-1138.
77. Kanda, D. H. F.; Nagashima, H. N.; Malmonge, J. A.; Sakamoto, W. K.; Chierice, G. O. *Journal of materials science* **2008**, 43, 5436-5440.
78. Pissis, P.; Kanapitsas, A.; Savelyev, Y. V.; Akhranovich, E. R.; Privalko, E. G.; Privalko, V. P. *Polymer* **1998**, 39, (15), 3431-3435.
79. Tsonos, C.; Apekis, L.; Viras, K.; Stepanenko, L.; Karabanova, L.; Sergeeva, L. *Journal of Macromolecular Science - Physics* **2000**, 39, (2), 155-174.
80. Tsonos, C.; Apekis, L.; Zois, C.; Tsonos, G. *Acta Materialia* **2004**, 52, 1319-1326.

## Chapter 2

### Counterion Dynamics in Polyurethane-Carboxylate Ionomers with Ionic Liquid Counterions

#### 2.1 Introduction

Many applications of polymer ion conductors simultaneously require high ionic conductivity and high modulus. Lithium ion battery separator membranes and ion-transport actuators are two high-profile examples. Polyethylene glycol (PEG or PEO) and PEO-based polymer electrolytes have been the mainstream research focus since 1973 because of their excellent ability to solvate cations.<sup>1-3</sup> Although PEO-based homopolymer electrolytes have reasonable ionic conductivities, many of them suffer from poor mechanical strength due to the low glass-transition temperature ( $T_g$ ) of PEO.<sup>4</sup> Ionic conductivity benefits from the fast segmental motion of low  $T_g$  materials but the modulus is at best the plateau modulus of the polymer melt ( $\sim 1 \times 10^6$  Pa). With single-phase systems, ionic conductivity increases and modulus decreases as  $T_g$  is lowered, resulting in a correlation (trade-off) between modulus and conductivity.<sup>4</sup>

To obtain materials with simultaneous high modulus and high conductivity, polymers that spontaneously microphase separate into hard domains (high modulus) and soft domains that transport ions, are needed. Block copolymers have been used<sup>5,6</sup> but here we focus on segmented copolymers. Polyurethane (PU) ionomers can be quite interesting candidates, as their microphase separation can allow a hard phase that provides high modulus to coexist with a continuous soft phase that transports ions. Various strategies

have been used to attach ionic groups to polyurethanes.<sup>7-10</sup> Different metal cations can change  $T_g$  and morphology. The modulus can reach  $1 \times 10^7$  to  $1 \times 10^9$  Pa even far above the  $T_g$  of the soft phase when attaching ionic groups in the hard segment.<sup>11-13</sup> In terms of ionic conductivity,  $1 \times 10^{-7}$  to  $1 \times 10^{-8}$  S/cm at room temperature has been achieved for  $\text{Li}^+$  or  $\text{Na}^+$  counterions, with modulus of  $1 \times 10^8$  Pa when replacing the urethane proton with a sulfonated group in the hard segment.<sup>14</sup>

However, unlike the many studies of mechanical properties of PU ionomers,<sup>7,8</sup> conductivity and dielectric studies are less common and more focusing on varying metal counterions.<sup>15</sup> Dielectric relaxation spectroscopy (DRS) has proved to be a very useful tool for PU ionomer studies.<sup>16,17</sup> Combined with thermal and mechanical tests, DRS allows understanding of both microphase separation and dipole/polymer chain relaxation in the soft phase, as well as ionic conductivity.<sup>17-19</sup>

In this paper, PEG with  $M_n = 600$  (~13 repeating units) and  $M_w/M_n < 1.2$  was chosen as the soft segment because of its famous ability to solvate cations<sup>1-3</sup> and being short enough to inhibit crystallization. About 2 orders of magnitude higher ionic conductivity has been reported for PEO- than poly(tetramethylene oxide)-based PU ionomers.<sup>18,20</sup> Para-Phenylene diisocyanate (pPDI) was used as the hard segment because its symmetry facilitates microphase separation.<sup>21,22</sup> Carboxylic acid containing diol was used as the chain extender, effectively placing the ionic group between two pPDI segments. By varying from the small alkali metal  $\text{Na}^+$  to large multiatom cations like ammonium, imidazolium and phosphonium, we hope to understand how both the counterion size and species affect the morphology,  $T_g$ , conductivity, dielectric constant, conducting ion content and mobility in PU ionomers, with particular consideration of

their utility for ionic actuators. A principal finding is that these materials do not microphase separate in the conventional sense but counterions are trapped by the pPDI-carboxylate-pPDI segments, unable to participate in ionic conduction.

## 2.2 Materials and experimental methods

Para-phenylene diisocyanate (pPDI), 2,2-bis(hydroxymethyl)butyric acid (DMBA), sodium hydroxide, 4-methylmorpholine, iodomethane, tris[2-(2-methoxyethoxy)ethyl]amine, tetrabutylammonium hydroxide-30 hydrate ( $\text{Bu}_4\text{N}^+\text{-OH}$ ), tributyl phosphine, tetrabutylphosphonium hydroxide (40 wt % aqueous solution) ( $\text{Bu}_4\text{P}^+\text{-OH}$ ), N-methylimidazole and butyl-methyl-imidazolium chloride ( $\text{BuMeIm}^+\text{-Cl}$ ) were purchased from Aldich. Tetramethylammonium hydroxide-5 hydrate ( $\text{Me}_4\text{N}^+\text{-OH}$ ) was purchased from Fluka. Polyethylene glycol (PEG,  $M_n = 600$  and  $M_w/M_n < 1.2$  from the manufacturer and confirmed by aqueous SEC and  $^1\text{H}$  NMR in  $\text{DMSO-d}_6$ ) and 2-bromoethyl methyl ether were purchased from TCI America, Inc. Anhydrous N,N-dimethylformamide (DMF) and diethyl ether were purchased from EMD. Anionic ion-exchange resin Amberlite IRA-400 was purchased from Alfa Aesar. pPDI was purified by sublimation at  $80\text{ }^\circ\text{C}$  under vacuum as in literature.<sup>21</sup> PEG 600 was vacuum-dried at  $80\text{ }^\circ\text{C}$  for at least 24 h before use. All other chemicals were used as received.

### 2.2.1 Polyurethane and counterions synthesis and ionomers preparation

**Carboxylic Acid Containing Polyurethane (PU) Synthesis.** pPDI, PEG 600 and DMBA with the molar ratio of 2:1:1 were dissolved in anhydrous DMF and reacted at 60 °C. The chemical structure of the product polyurethane is shown in Figure 2-1. It is a random segmented copolymer with pPDI segments between PEG 600 and carboxylic acid sections. The reaction was monitored by FTIR until the isocyanate peak (~2200  $\text{cm}^{-1}$ ) disappears (in 4-5 h). Synthesized products were precipitated in diethyl ether 3 times and dried at 80 °C under vacuum. The final purification was done by dialysis after neutralization to make the carboxylate ionomers, which are water-soluble.

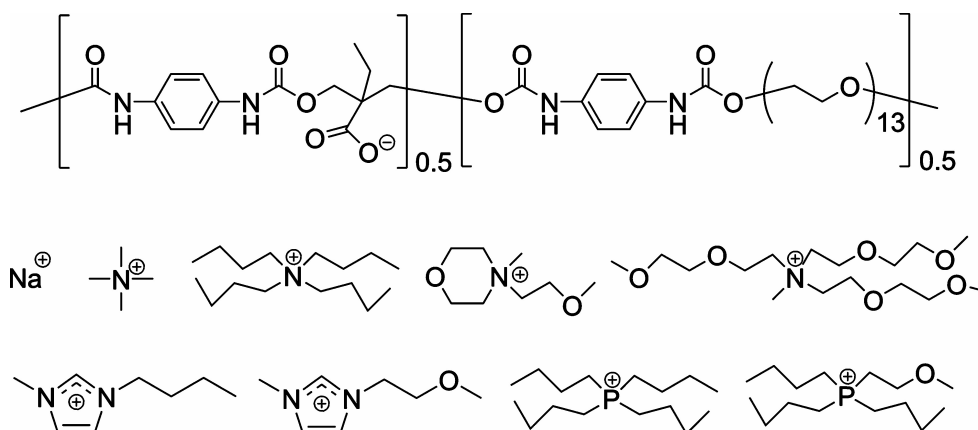


Figure 2-1: Chemical Structures of Polyurethane Anionomer and Cations Studied:  $\text{Na}^+$ ,  $\text{Me}_4\text{N}^+$ ,  $\text{Bu}_4\text{N}^+$ ,  $(\text{EOc})_2\text{Me}(\text{MOE})\text{N}^+$ ,  $(\text{MOEOE})_3\text{MeN}^+$ ,  $\text{BuMeIm}^+$ ,  $(\text{MOE})\text{MeIm}^+$ ,  $\text{Bu}_4\text{P}^+$ ,  $\text{Bu}_3(\text{MOE})\text{P}^+$  (from left to right, top to bottom)

**Counterion Synthesis.** *Tris[2-2(methoxyethoxy)ethyl]methyl Ammonium Iodide* ( $(\text{MOEOE})_3\text{MeN}^+\text{-I}$ ). *Tris[2-2(methoxyethoxy)ethyl]amine* and 50% excess of iodomethane were dissolved in toluene and charged into a round-bottom flask in an ice bath. The mixture was allowed to reach room temperature and react overnight. The

product was a dark yellow liquid that phase separated from the raw material and was purified by extraction with toluene then dried at 70 °C under vacuum.  $^1\text{H}$  NMR ( $\text{D}_2\text{O}$ ):  $\delta$  3.17 (s, 3H,  $-\text{N}^+-\text{CH}_3$ ); 3.33 (s, 9H,  $-\text{O}-\text{CH}_3$ ); 3.58, 3.59 (d, 12H,  $-\text{O}-\text{CH}_2\text{CH}_2-\text{O}-$ ); 3.69 (s, 6H,  $\text{N}^+-\text{CH}_2-\text{CH}_2-\text{O}-$ ); 3.91 (s, 6H,  $-\text{N}^+-\text{CH}_2-\text{CH}_2-\text{O}-$ ).

*N*-(2-methoxyethyl)-*N*-methylmorpholinium Bromide ( $(\text{EOc})_2\text{Me}(\text{MOE})\text{N}^+-\text{Br}$ ). 2-Bromoethyl methyl ether and 100% excess *N*-methylmorpholinium were reacted at 70 °C overnight. The product was dissolved in methanol and recrystallized in an excess of acetone. The white crystal product was then dried at 70 °C under vacuum.  $^1\text{H}$  NMR ( $\text{D}_2\text{O}$ ):  $\delta$  3.19 (s, 3H,  $-\text{N}^+-\text{CH}_3$ ); 3.31 (s, 3H,  $-\text{O}-\text{CH}_3$ ); 3.4-3.5 (m, 4H,  $-\text{N}^+-\text{CH}_2-\text{CH}_2-\text{O}-$ ); 3.97 (s, 4H,  $-\text{N}^+-\text{CH}_2-\text{CH}_2-\text{O}-$ ); 3.66 (s, 2H,  $-\text{N}^+-\text{CH}_2-\text{CH}_2-\text{O}-\text{CH}_3$ ); 3.85 (s, 2H,  $-\text{N}^+-\text{CH}_2-\text{CH}_2-\text{O}-\text{CH}_3$ ).

(2-Methoxyethyl)-tributylphosphonium Bromide ( $\text{Bu}_3(\text{MOE})\text{P}^+-\text{Br}$ ). Tributyl phosphine and 2-bromoethyl methyl ether with 10% excess were reacted at 80 °C for 1 day. The product was washed with a large amount of diethyl ether 3 times and vacuum dried at 70 °C.  $^1\text{H}$  NMR ( $\text{DMSO}-d_6$ ):  $\delta$  0.92 (t, 9H,  $-\text{CH}_3$ ); 1.3-1.5 (m, 12H,  $-\text{P}^+-\text{CH}_2-\text{CH}_2-\text{CH}_2-\text{CH}_3$ ); 2.2 (t, 6H,  $-\text{P}^+-\text{CH}_2-\text{CH}_2-\text{CH}_2-\text{CH}_3$ ); 2.6 (m, 2H,  $-\text{P}^+-\text{CH}_2-\text{CH}_2-\text{O}-$ ); 3.3 (s, 3H,  $-\text{O}-\text{CH}_3$ ); 3.6 (m, 2H,  $-\text{CH}_2-\text{O}-$ ).

*Methoxyethyl Methyl Imidazolium Bromide* ( $(\text{MOE})\text{MeIm}^+-\text{Br}$ ). *N*-methylimidazole and 20% excess 2-bromoethyl methyl ether were reacted at 40 °C for 1 day. The product was washed and recrystallized in diethyl ether and dried at 70 °C under vacuum.  $^1\text{H}$  NMR ( $\text{DMSO}-d_6$ ): 3.27 (s, 3H,  $-\text{N}-\text{CH}_3$ ); 3.68 (t, 2H,  $-\text{N}-\text{CH}_2-\text{CH}_2-\text{O}-$ ); 3.88 (s, 3H,  $-\text{O}-\text{CH}_3$ ); 4.36 (t, 2H,  $-\text{N}-\text{CH}_2-\text{CH}_2-\text{O}-$ ); 7.7 (d, 2H,  $-\text{N}-\text{CH}=\text{CH}-\text{N}-$ ); 9.16 (t, 1H,  $-\text{N}-\text{CH}-\text{N}-$ ).

**Ion exchange, Purification, and Molecular Weight.** The ammonium and phosphonium salts above were ion exchanged with Amberlite IRA-400 ion-exchange resin to prepare hydroxide aqueous solutions and stored in a refrigerator for later use. The concentration was determined by titration with 0.1N HCl standard solution.

One gram of the carboxylic acid containing polyurethane was dissolved in the counterion- hydroxide aqueous solution (with 10% excess hydroxide to ensure 100% neutralization) and then dialyzed in a dialysis cassette (MW cutoff = 2000) in deionized water for 1 week to remove any extra ions. The product was then dried at 70 °C under vacuum. The dried PU ionomers are fully water-soluble. The ionomer with counterion structures and some physical properties are summarized in Figure 2-1 and Table 2-1. The ionomer has  $M_w = 12000$ ,  $M_n = 8400$ ,  $M_w/M_n = 1.4$  (polystyrene equivalent molar masses) determined by size exclusion chromatography with 0.01 M LiBr DMF solution as the mobile phase. This number agrees with the estimation ( $M_n = 9000$ , ~ 9 repeating units with  $M_{w,hard\ segment} = 410$  and  $M_{w,soft\ segment} = 600$ ) by  $^1H$  NMR. The cation to ether oxygen ratio is 1/13.

Table 2-1: Cation-Anion Distance<sup>a</sup>, Glass Transition Temperature and Quadrupole Formation Energy  $\Delta E_{\text{quadrupole}}$ <sup>b</sup> of the Ion Pair Calculated by ab initio at 0K in Vacuum.

	$[M/(d N_{\text{av}})]^{1/3}$ (Å)	$T_g$ (K)	$\Delta E_{\text{quadrupole}}$ (kJ/mol)
Na <sup>+</sup>	5.1	323	1400
Me <sub>4</sub> N <sup>+</sup>	6.0	308	930
BuMeIm <sup>+</sup>	6.9	304	880
(MOE)MeIm <sup>+</sup>	6.9	298	890
(EO <sub>c</sub> ) <sub>2</sub> Me(MOE)N <sup>+</sup>	7.0	291	860
Bu <sub>4</sub> N <sup>+</sup>	7.9	289	820
Bu <sub>4</sub> P <sup>+</sup>	8.1	273	790
Bu <sub>3</sub> (MOE)P <sup>+</sup>	8.1	284	790
(MOEOE) <sub>3</sub> MeN <sup>+</sup>	8.7	267	900

<sup>a</sup>Cation-anion distance is calculated from the molar mass of the cation acetate salt, assuming density  $\rho = 1 \text{ g/cm}^3$ . <sup>b</sup> $\Delta E_{\text{quadrupole}}$  is defined as the energy difference between the quadrupole state and 2 free cations plus 2 free anions at 0 K in vacuum.

### 2.2.2 Experimental methods

**Ab initio Calculation.** In this study, ab initio calculations were employed to determine interaction energies of quadrupoles (Table 2-1), and the charge distribution of cations (Table 2-2). All calculations were performed using density functional theory methods with the Gaussian 03 software package. Exchange and correlation were included using the hybrid-GGA B3LYP functional.<sup>23-26</sup> Dipole moments of polar solvents and energy of interactions of polar solvents with ions agree with vapor phase data<sup>27</sup> for the basis set used.

Table 2-2: Charge Distribution of  $\text{Bu}_4\text{P}^+$ ,  $\text{Bu}_4\text{N}^+$  and  $\text{BuMeIm}^+$  from *ab initio* Calculation.

	center (P or N)	$\alpha\text{-CH}_2$	$\beta\text{-CH}_2$	$\text{CH}_3$	$\text{CH}=\text{CH}$	$\text{CH}$
$\text{Bu}_4\text{P}^+$	1.1	-0.2	0	-	-	-
$\text{Bu}_4\text{N}^+$	-0.5	0.3	0	-	-	-
$\text{BuMeIm}^+$	-0.3, -0.3	0.4	0	0.4	0.2	0.4

**Differential Scanning Calorimetry (DSC).** The calorimetric glass transition temperature  $T_g$  was measured using a Seiko Instruments SSC/5200 (Table 2-1). All samples were dried at 75 °C under vacuum for 2 days before measurement.  $T_g$  was obtained from the change in heat capacity during the second heating at a heating rate of 10 K/min under dry nitrogen purge after cooling from 80 °C at 10 K/min.

**Rheology.** Linear viscoelastic response was probed in oscillatory shear using a Rheometrics RDS-II. All samples were dried at 75 °C under vacuum for 2 days and then molded to ~1 mm thick pellets with diameter of either 4 mm (for  $\text{Na}^+$ ,  $\text{Me}_4\text{N}^+$ ,  $\text{BuMeIm}^+$ , and  $(\text{MOE})\text{-MeIm}^+$ ) or 7.9mm(for all other samples) at 80 °C under vacuum for 20 min. The temperature step data were collected every 1 °C from 30 to 80 °C at 1 rad/s with 60 s soak time.

**Dielectric Relaxation Spectroscopy (DRS).** Samples were dried at 75 °C under vacuum for 1 day to remove moisture and then sandwiched between two 20 mm diameter freshly polished brass electrodes with 50-100  $\mu\text{m}$  silica fiber spacers. The prepared cells were annealed in the vacuum oven for an additional 24 h at 75 °C under vacuum. Dielectric (impedance) spectra were measured using a Novocontrol GmbH Concept 40 broadband dielectric spectrometer in the frequency range of  $1 \times 10^{-2}$  to  $1 \times 10^7$  Hz with 0.1 V amplitude. Samples were annealed at 80 °C in the equipment for 1 h and then

allowed to reach equilibrium with temperature for at least 30 min before each isothermal measurement.

## 2.3 Results and discussions

### 2.3.1 Glass Transition Temperature ( $T_g$ )

As described in the literature, different metal cations can have very different impact on  $T_g$ , depending on the chemical composition of the PU ionomers.<sup>11,28</sup> In our system, only one  $T_g$  has been seen and  $T_g$  decreases dramatically with increasing cation size. Figure 2-2(a) shows  $T_g$  as a function of inverse size of corresponding cation-acetate salts (assuming all the salts have the same density of 1 g/cm<sup>3</sup>). The precursor acid form PU has  $T_g = 23$  °C. Introduction of small sodium ions increases the  $T_g$  to 47 °C. The increase of  $T_g$  with alkali metal counterions is common,<sup>29</sup> possibly originating from some combination of (1) mixing soft and hard segment and (2) the Coulombic force between cations and anions acting as physical cross-links. The PEO soft segment is well-known for its ability to solvate cations so it is not surprising that the presence of sodium cations in the hard segment helps mix the soft and hard segment, increasing the  $T_g$ . Simultaneously, with Na<sup>+</sup> counterions, many ion pairs associate, which also increases  $T_g$ . Other evidence of phase mixing in the Na-ionomer is that it has much higher  $T_g$  than a PEG600 based polyester ionomer PEG600-Na<sup>+</sup> ( $T_g = -5$  °C) with similar ion concentration.<sup>30</sup> Although nonionic PU with pPDI hard segment tends to microphase

separate,<sup>21</sup> there is no evidence from our DSC study for microphase separation in both the acid form precursor and the ionomers.

It is clear in Figure 1a that  $T_g$  scales inversely with cation acetate salt size. Similar phenomena with various metal ions have also been observed in different ionomer systems.<sup>28,31,32</sup> Ion pairs associate to form physical cross-links and  $T_g$  reflects the energy required to separate associated ion pairs.<sup>31,33</sup> Larger cations have a longer distance between the positive and negative charge and require much less energy to separate them, originating from Coulomb's law:  $E \sim e^2/d$ , where  $e$  and  $-e$  are charges carried by cation and anion and  $d$  is the distance between two charges. The lower interaction energy results in reduced  $T_g$  with an apparent inverse correlation with the ion size. Meanwhile, lower  $T_g$  also indicates fewer ionic cross-links<sup>11,12</sup> also due to weaker Coulombic interaction.

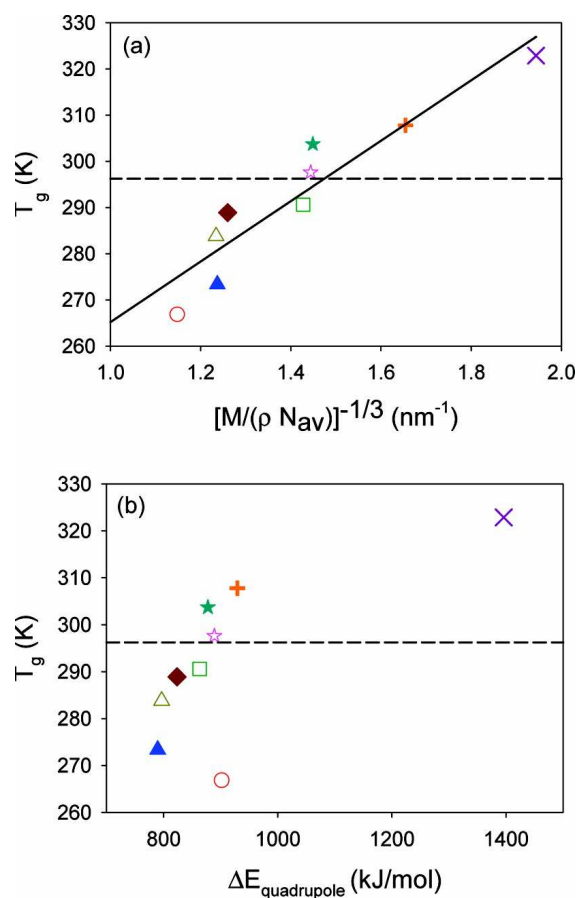


Figure 2-2:  $T_g$  from DSC as a function of (a) reciprocal size of corresponding acetate salts (assuming the same density  $\rho$  of 1.0 g/cm<sup>3</sup>) and (b) quadrupole energy at 0K in vacuum. Open symbols are cations containing ether oxygen. Solid symbols are cations without ether oxygen. Purple X is Na<sup>+</sup>; orange plus is Me<sub>4</sub>N<sup>+</sup>; cyan solid star is BuMeIm<sup>+</sup>; pink open star is (MOE)MeIm<sup>+</sup>; green open square is (EOc)<sub>2</sub>Me(MOE)N<sup>+</sup>; dark red solid diamond is Bu<sub>4</sub>N<sup>+</sup>; blue solid triangle is Bu<sub>4</sub>P<sup>+</sup>; olive green open triangle is Bu<sub>3</sub>(MOE)P<sup>+</sup>; red open circle is (MOEEOE)<sub>3</sub>MeN<sup>+</sup>; dash line is acid form for the reference; solid line is fitting result of equation  $T_g = 200 + 65.4 [M/(\rho N_{av})]^{-1/3}$ .

$T_g$  as a function of quadrupole energy (energy required to break quadrupoles) from ab initio calculation is also plotted in Figure 2-2(b). It shows similar results as Figure 2-2(a) since quadrupole energy is strongly affected by counterion size due to Coulombic force. It is interesting that (MOEEOE)<sub>3</sub>MeN<sup>+</sup> has the lowest  $T_g$ . The quadrupole energy of (MOEEOE)<sub>3</sub>MeN<sup>+</sup> is not the lowest (an outlier in Figure 2-2(b)),

possibly because this energy is calculated at 0K under vacuum without consideration of any entropy contribution, which might be more important for (MOEOE)<sub>3</sub>MeN<sup>+</sup> due to its three much longer side chains.

Note also that tetrabutylphosphonium (Bu<sub>4</sub>P<sup>+</sup>) has T<sub>g</sub> 20K lower than tetrabutylammonium (Bu<sub>4</sub>N<sup>+</sup>) despite similar size and chemical structure. This is due to the different electronegativity<sup>34</sup> of the nitrogen and phosphorus atoms in these two cations. Table 2-2 shows the charge distribution of three classes of cations we study in this paper: Bu<sub>4</sub>P<sup>+</sup>, Bu<sub>4</sub>N<sup>+</sup>, and BuMeIm<sup>+</sup>. The phosphorus atom at the center of Bu<sub>4</sub>P<sup>+</sup> carries positive charge (+1.1e) because it is less electronegative than carbon and leaves the outer atoms to share -0.1e, whereas the nitrogen atom in Bu<sub>4</sub>N<sup>+</sup> is more electronegative than carbon and carries negative charge (-0.5e) and leaves the surrounding atoms sharing +1.5e. The negatively charged outer layer of Bu<sub>4</sub>P<sup>+</sup> provides better shielding of the positive charge at the center from anions, resulting in weaker Coulombic force and lower T<sub>g</sub> (the two phosphonium cations have the smallest quadrupole energy in Table 2-1 for the same reason). For Bu<sub>4</sub>N<sup>+</sup>, the more positively charged molecule surface has stronger attraction with anions and thus has higher T<sub>g</sub>. For imidazolium, although the nitrogen atom still is weakly negative like ammonium, the steric structure is very different. The nearly flat structure of the imidazole ring makes most of the atoms exposed to anions have a shorter effective distance compared to the tetrahedral ammonium and phosphonium, raising T<sub>g</sub> of the ionomers with imidazolium counterions relative to the similar sized (EOc)<sub>2</sub>Me(MOE)N<sup>+</sup> ammonium. It is also interesting that attachment of ether-oxygen containing alkyl chains to the counterions have different effects on T<sub>g</sub>: T<sub>g</sub> is suppressed in ammonium and imidazolium but raised in

phosphonium, again because of the the electronegativity of C, O, N, and P and different charge distributions. Ether-oxygen makes the adjacent carbon more positively charged which changes the surface charge distribution of phosphonium and increases  $T_g$ . In ammonium and imidazolium, where carbon atoms already carry positive charges, ether oxygens provide some shielding from anions and decrease  $T_g$ .

### 2.3.2 Rheology and morphology

Storage and loss modulus  $G'$  and  $G''$  and  $\tan \delta$  in temperature sweeps at 1 rad/s as functions of  $T/T_g$  are plotted in Figure 2-3(a). As expected, ionomers with larger counterions have smaller  $G'$  and  $G''$ .<sup>35,36</sup> Only  $\text{Na}^+$ ,  $\text{Me}_4\text{N}^+$ ,  $\text{BuMeIm}^+$ ,  $(\text{MOE})\text{MeIm}^+$ ,  $\text{Bu}_3(\text{MOE})\text{P}^+$  and  $(\text{MOEOE})_3\text{MeN}^+$  data are shown. Other samples have similar behavior with  $\text{Bu}_3(\text{MOE})\text{P}^+$  and  $(\text{MOEOE})_3\text{MeN}^+$  and were omitted for clarity. Imidazolium-based ionomers show different character than the other ionomers.  $\text{BuMeIm}^+$  and  $(\text{MOE})\text{MeIm}^+$  ionomers both have a clear glass transition peak in  $\tan \delta$  as most homogeneous polymers do, while the  $(\text{MOE})\text{MeIm}^+$  ionomer also has a small shoulder at higher temperature. On the other hand,  $\text{Na}^+$ , ammonium and phosphonium ionomers show a glass transition peak at slightly higher  $T/T_g$  with a very broad shoulder at higher temperature. The shoulder-like behavior of PU usually indicates microphase separation.<sup>37,38</sup> However, no microphase separation peaks were observed in SAXS measurement for all ionomers (and the acid form precursor; data not shown) while time-temperature superposition works perfectly (Figure 2-3(b)) and these both suggest there is no discrete microphase separation. All ionomers collapse into the same curve in a Cole-Cole plot in the Figure 2-

**3(b)** inset, also suggesting no discrete microphase separation.<sup>39</sup> We believe the broad shoulder in our system is from various local environments<sup>40</sup> (i.e., various concentrations of pPDI-carboxylate-pPDI/cation segment) resulting in a wide distribution of relaxation times instead of discrete microphase separation. It is also interesting that imidazolium ionomers are more homogeneous than all other ionomers. This is perhaps due to the acidic protons on the ring of imidazolium that are hydrogen bond donors.<sup>41</sup> These can interrupt the hydrogen bonding between urethane linkages more than other counterions as well as have stronger interaction with ether oxygens on PEO segments. Meanwhile, acidity of the protons on the ring can be slightly reduced by having ether oxygen containing tails<sup>41,42</sup> and this perhaps explains why (MOE)MeIm<sup>+</sup> has a small shoulder in  $\tan \delta$  compared to BuMeIm<sup>+</sup>. The local environment differences also impact the amount of counterions available under electric field and we will discuss this later.

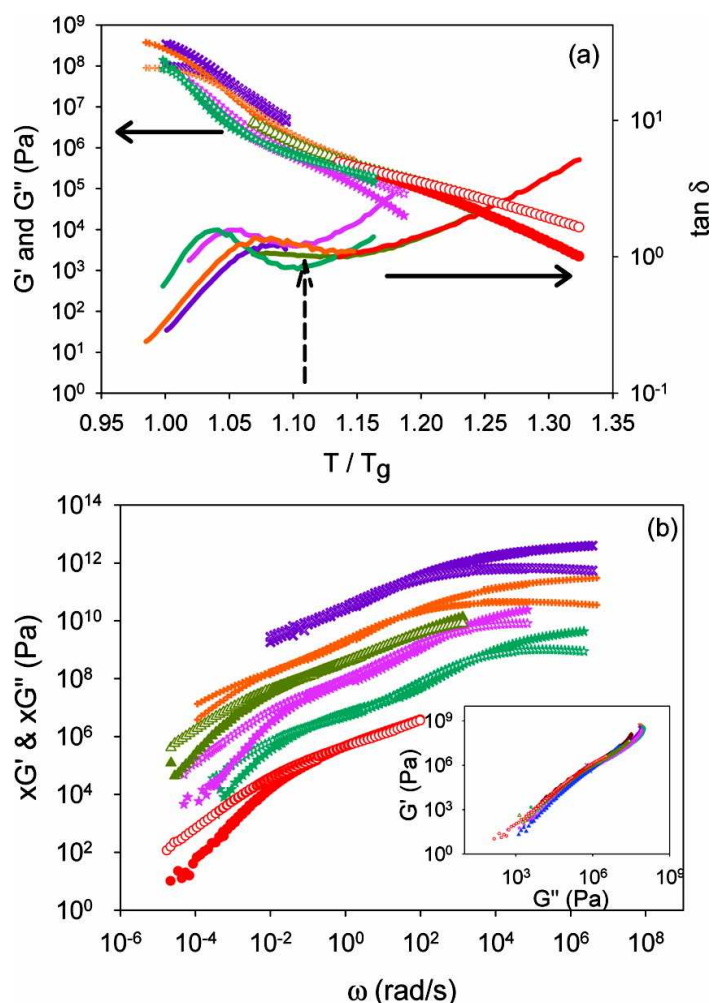


Figure 2-3: (a) Storage and loss modulus and  $\tan \delta$  (solid curve) as function of  $T/T_g$  at 1 rad/s. Dashed arrow indicates the shoulder of nonimidazolium ionomers. (b) Master curves of storage ( $G'$ , filled symbols) and loss ( $G''$ , open symbols) modulus as functions of frequency from time-temperature superposition of oscillatory shear data at various temperatures, shifted to  $T_g + 30$  K. Inset: Cole-Cole plot of oscillatory shear data for all ionomers at various temperatures. Purple X is  $\text{Na}^+$  ( $x = 8000$ ); orange plus is  $\text{Me}_4\text{N}^+$  ( $x = 500$ ); cyan star is  $\text{BuMeIm}^+$  ( $x = 10$ ); pink star is  $(\text{MOE})\text{MeIm}^+$  ( $x = 100$ ); dark red diamond is  $\text{Bu}_4\text{N}^+$ ; blue triangle is  $\text{Bu}_4\text{P}^+$ ; olive green triangle is  $\text{Bu}_3(\text{MOE})\text{P}^+$  ( $x = 300$ ); red circle is  $(\text{MOEOE})_3\text{MeN}^+$  ( $x = 1$ );  $\text{Bu}_4\text{N}^+$ ,  $\text{Bu}_4\text{P}^+$  and  $(\text{EOc})_2\text{Me}(\text{MOE})\text{N}^+$  are not shown for clarity.

### 2.3.3 Polymer Relaxation

The dielectric loss spectra of ionomers are usually dominated by conduction and electrode polarization (EP) in the low frequency region, which can mask the relaxation. Instead of analyzing dielectric loss directly, the common method to remove the pure-loss conductivity contribution is to plot the derivative dielectric loss spectra using the following formula derived from the Kramers-Kronig relation, since  $\epsilon'(\omega)$  and  $\epsilon''(\omega)$  must be the real and imaginary parts of the same complex function<sup>16,19,43,44</sup> (Eq. 2-1)

$$\epsilon_{der}(\omega) = -\frac{\pi}{2} \frac{\partial \epsilon'(\omega)}{\partial \ln \omega} \quad (2-1)$$

Figure 2-4 shows the dielectric loss derivative spectra of PU ionomers with different cations, at their  $T_g$ . From high to low frequency, the first peak of  $\epsilon_{der}$  corresponds to the  $\alpha$  (segmental) relaxation, which is revealed by the derivative analysis, and then the rapid increase at lower frequency is EP.  $\epsilon_{der}$  and the dielectric loss  $\epsilon''$  are compared in the Figure 2-4(a) inset. It is surprising that the  $\alpha$ -relaxation at  $T_g$  does not occur at the same frequency for larger cations ( $Bu_4N^+$ ,  $Bu_4P^+$ ,  $Bu_3(MOE)P^+$ , and  $(MOEOE)_3MeN^+$ , which has the lowest  $T_g$ ) This implies the polymer chain relaxation does not determine the  $T_g$  measured with DSC. Instead,  $T_g$  is more strongly correlated with the cation-anion interaction (see Figure 2-2). Besides the  $\alpha$ -relaxation peak frequency, the shape of the peak also depends on cation. In Figure 2-4, only  $Na^+$  (purple X) and  $Me_4N^+$  (orange plus) have clear, roughly symmetric peaks, whereas the other cations have asymmetric peaks or merely a shoulder on the high-frequency side of EP.

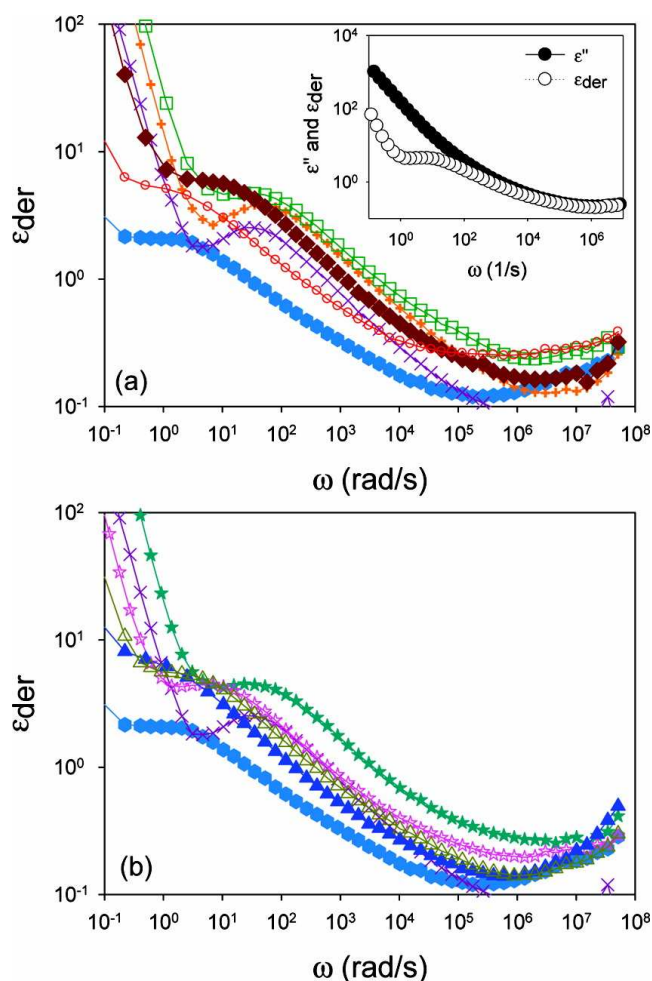


Figure 2-4: (a) Dielectric loss derivative spectra of  $\text{Na}^+$ ,  $\text{Me}_4\text{N}^+$ ,  $(\text{EOc})_2\text{Me}(\text{MOE})\text{N}^+$ ,  $\text{Bu}_4\text{N}^+$  and  $(\text{MOEOE})_3\text{MeN}^+$  ionomers at corresponding  $T_g \pm 5$  K. Inset: Dielectric loss (solid symbol) and derivative (open symbol) spectra of  $(\text{MOE})\text{MeIm}^+$  at  $T_g$  (20 °C). (b) Dielectric loss derivative spectra of  $\text{Na}^+$ ,  $\text{BuMeIm}^+$ ,  $(\text{MOE})\text{MeIm}^+$ ,  $\text{Bu}_4\text{P}^+$  and  $\text{Bu}_3(\text{MOE})\text{P}^+$  at corresponding  $T_g \pm 5$  K. Purple X is  $\text{Na}^+$ ; orange plus is  $\text{Me}_4\text{N}^+$ ; cyan solid star is  $\text{BuMeIm}^+$ ; pink open star is  $(\text{MOE})\text{MeIm}^+$ ; green open square is  $(\text{EOc})_2\text{Me}(\text{MOE})\text{N}^+$ ; dark red solid diamond is  $\text{Bu}_4\text{N}^+$ ; blue solid triangle is  $\text{Bu}_4\text{P}^+$ ; olive green open triangle is  $\text{Bu}_3(\text{MOE})\text{P}^+$ ; red open circle is  $(\text{MOEOE})_3\text{MeN}^+$ ; light blue solid hexagon is the acid form (nonionic polymer).

In Figure 2-4, the  $\alpha$  peak height of  $\text{Na}^+$  is significantly smaller than others which gives some insight about the local hydrogen bonded pPDI-carboxylate-pPDI segment and

soft segments. The magnitude of the  $\alpha$ -relaxation in  $\epsilon_{\text{der}}$  represents the concentration of dipoles that can respond to the electric field.<sup>16,17</sup>

Figure 2-5 shows the  $\alpha$ -relaxation peak frequency,  $\omega_{\alpha}$ , as a function of inverse temperature with the inset plotted as a function of  $T_g/T$ .  $\omega_{\alpha}$  is determined as the frequency where  $\epsilon_{\text{der}}$  has its peak by fitting the  $\alpha$ -peak with the Havriliak-Negami equation<sup>16</sup> after removing the contribution of electrode polarization. The inset of Figure 2-5 shows that the calorimetric  $T_g$  is not directly related to polymer segmental relaxation. It can be seen that the smaller cations show slower  $\alpha$ -relaxation due to more and/or stronger association of ion pairs with each other and with urethane linkages. On the other hand, the presence of ether oxygens on the cations accelerates the  $\alpha$ -relaxation, except in phosphonium cations.

The temperature dependence of the  $\alpha$ -relaxation follows the Vogel-Fulcher-Tammann (VFT) equation (solid curves in Figure 2-5) (Eq. 2-2):

$$\omega(T) = \omega_0 \exp\left(\frac{-DT_0}{T - T_0}\right) \quad (2-2)$$

where  $\omega_0$  is the unconstrained (high T) frequency,  $T_0$  is the Vogel temperature, and D is a parameter related to fragility. Table 2-3 summarizes the VFT fitting parameters for the  $\alpha$  relaxation frequency. There is no correlation between calorimetric  $T_g$  and the  $\alpha$ -relaxation Vogel temperature  $T_0$ . It is worth to note that the data can also be fit using a common  $T_0 = 202$  K with  $R^2 \geq 0.99$ . The Vogel temperature  $T_0$  in our PU ionomer system is similar to other PEG600-based polyester ionomers<sup>43,45</sup> even though our PU ionomers have much higher  $T_g$  in DSC. This again confirms that the  $\alpha$ -relaxation that we

see is corresponding to PEO segmental motion, while the calorimetric  $T_g$  is restricted by the cross-link-like ion pair interactions. Nonionic glass-forming liquids and polymers have larger  $D$  (lower fragility) associated with stronger intermolecular interactions.<sup>46</sup> Consequently, it is not surprising that  $D$  increases as counterions get smaller and interact with both carboxylate anion and PEO ether oxygen more strongly.

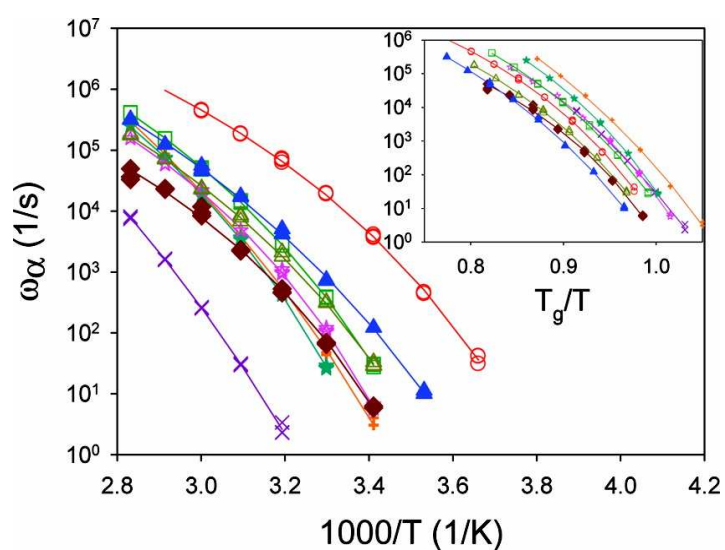


Figure 2-5:  $\alpha$ -relaxation frequency as a function of temperature. Inset:  $\alpha$  relaxation frequency as a function of  $T_g$  normalized temperature. Purple X is  $\text{Na}^+$ ; orange plus is  $\text{Me}_4\text{N}^+$ ; cyan solid star is  $\text{BuMeIm}^+$ ; pink open star is  $(\text{MOE})\text{MeIm}^+$ ; green open square is  $(\text{EOc})_2\text{Me}(\text{MOE})\text{N}^+$ ; dark red solid diamond is  $\text{Bu}_4\text{N}^+$ ; blue solid triangle is  $\text{Bu}_4\text{P}^+$ ; olive green open triangle is  $\text{Bu}_3(\text{MOE})\text{P}^+$ ; red open circle is  $(\text{MOEOE})_3\text{MeN}^+$ . Solid line is best fitting for VFT equation (Eq. 2-2).

Table 2-3: Fitting Parameters for the Temperature Dependences of  $\alpha$ -Relaxation Frequency (Eq. 2-2), Conducting Ion Content (Eq. 2-10) and Conducting Ion Mobility (Eq. 2-11)

	$[M/(d N_{av})]^{1/3}$	$\alpha$ -relaxation		conducting ion content		conducting ion mobility					
		$T_g$	$T_0$	D	$\omega_0$	$p_0$	Ea (kJ/mol)	$T_0$	$T_g-T_0$	D	$\log \mu_0$
Na <sup>+</sup>	5.1	323	203	16.2	13.5	18*	10*	263	60	3.5	1.9
Me <sub>4</sub> N <sup>+</sup>	6.0	308	214	9.87	12.1	18.7	5.9	241	67	5.0	0.7
BuMeIm <sup>+</sup>	6.9	304	228	7.63	11.5	21.1	16	247	57	10.3	3.8
(MOE)MeIm <sup>+</sup>	6.9	298	233	5.18	9.56	19.5	11	242	56	4.0	1.5
(EOc) <sub>2</sub> Me(MOE)N <sup>+</sup>	7.0	291	225	6.18	10.3	19.5	12	234	56	4.5	0.9
Bu <sub>4</sub> N <sup>+</sup>	7.9	289	206	9.42	10.5	19.2	11	218	71	7.0	0.2
Bu <sub>4</sub> P <sup>+</sup>	8.1	273	177	15.8	12.5	19.0	12	205	68	7.7	-0.3
Bu <sub>3</sub> (MOE)P <sup>+</sup>	8.1	284	239	4.73	8.79	18.8	8.8	221	63	6.0	0.3
(MOEOE) <sub>3</sub> MeN <sup>+</sup>	8.7	267	202	7.39	10.7	19.0	7.3	205	62	6.3	0.4

\* Uncertainty of the fitting for Na<sup>+</sup> is higher than other samples due to limited amount of data points (50 – 80 °C).

### 2.3.4 Ionic conductivity

Temperature dependence of DC ionic conductivity ( $\sigma_{DC}$ , where the ionic conductivity is independent of frequency) is plotted in Figure 2-6(a). It is clear that samples with lower  $T_g$  have higher conductivity. At the same time, the presence of ether oxygens on the cations (open symbols in all figures) increases ionic conductivity (compared to cations with only alkyl chains) for ammonium and imidazolium counterions but not for phosphonium counterions (Bu<sub>4</sub>P<sup>+</sup> and Bu<sub>3</sub>(MOE)P<sup>+</sup>), which is due to the different effect on  $T_g$  discussed above. Figure 2-6(b) inset plots DC ionic conductivity against  $T_g/T$ , which collapses data compared to Figure 2-6(a) but roughly a factor of 40 spread in  $\sigma_{DC}$  remains. It is generally accepted in the literature that ion conduction in PEG-based polymer electrolytes is strongly coupled with polymer chain

relaxation.<sup>2,19,43,47</sup> DC conductivity is plotted against  $\alpha$ -relaxation frequency in Figure 2-6(b), where data naturally separate into two groups:  $\text{Na}^+$  and all other cations. All the ammonium, imidazolium, and phosphonium counterion ionomers have DC ionic conductivity connected to  $\alpha$ -relaxation frequency divided by temperature ( $\omega_\alpha/T$ ) as expected by the Debye-Stokes-Einstein equation (Eq. 2-3):

$$\frac{\sigma_{DC}}{\omega_\alpha/T} = 1.09 \times 10^{-9} \frac{\text{SsK}}{\text{cm-rad}} \quad (2-3)$$

shown as the upper solid line in Figure 5b. The fact that Eq. 2-3 applies to all counterions other than  $\text{Na}^+$  suggests they have similar concentrations of conducting counterions. The fact that  $\sigma_{DC}$  is a factor of 6 lower for  $\text{Na}^+$  suggests that the pPDI-carboxylate-pPDI segments may trap most of the  $\text{Na}^+$  and this will be discussed further when we quantify conducting ion content.

The slope of 1 in Figure 2-6(b) means the ion conduction is regulated by PEO segmental motion. Note that all the samples should contain the same amount of ions since they are prepared from the same acid form precursor but the actual amount of the cations that are really accessible in the matrix might be lower and change with temperature. It is interesting that we do not observe decoupling (slope lower than unity in Figure 2-6(b)) as observed in our previous study<sup>43</sup> of PEG-based polyester ionomers. From Barton-Nakajima-Namikawa relation,  $\sigma_{DC} \sim \Delta\epsilon_\alpha \omega_\alpha$ , where  $\Delta\epsilon_\alpha$  is the strength (magnitude) of  $\alpha$ -relaxation.<sup>55</sup> In our ionomers,  $\Delta\epsilon_\alpha$  is nearly independent of temperature (data not shown) resulting  $\sigma_{DC} \sim \omega_\alpha$  (since temperature range is small here, the effect of T can be negligible). This is why no decoupling was observed here.

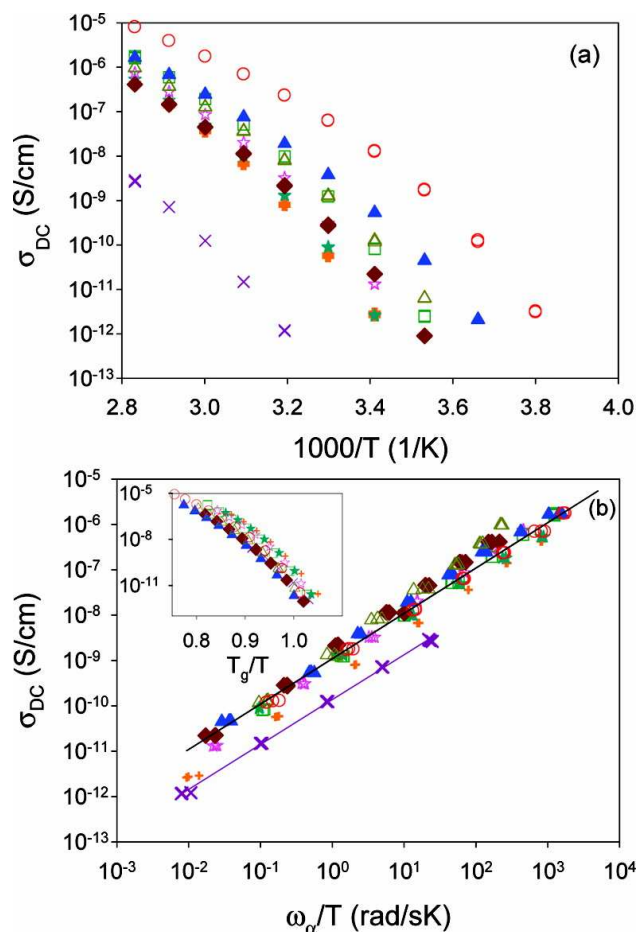


Figure 2-6: DC conductivity as function of (a)  $1000/T$ , (b)  $\alpha$ -relaxation frequency/temperature; inset,  $T_g/T$ . Purple X is  $\text{Na}^+$ ; orange plus is  $\text{Me}_4\text{N}^+$ ; cyan solid star is  $\text{BuMeIm}^+$ ; pink open star is  $(\text{MOE})\text{MeIm}^+$ ; green open square is  $(\text{EOc})_2\text{Me}(\text{MOE})\text{N}^+$ ; dark red solid diamond is  $\text{Bu}_4\text{N}^+$ ; blue solid triangle is  $\text{Bu}_4\text{P}^+$ ; olive green open triangle is  $\text{Bu}_3(\text{MOE})\text{P}^+$ ; red open circle is  $(\text{MOEOE})_3\text{MeN}^+$ .

### 2.3.5 Electrode polarization (EP)

DC conductivity ( $\sigma_{\text{DC}}$ ) of any single-ion conductor is simply the product of charge, mobility ( $\mu$ ) and number density ( $p$ ) of ions participating in conduction (Eq. 2-4):

$$\sigma_{\text{DC}} = e\mu p \quad (2-4)$$

where  $e$  is the elementary charge (of all monovalent cations). Although all “nontrapped” counterions in the soft phase eventually contribute equally to conduction, our interest here is the number density of conducting ions in a given instant in time, and their mobility. We make use of an electrode polarization (EP) model (Macdonald/Coelho model)<sup>19,30,48,49</sup> that integrates the Poisson-Boltzmann equation to obtain the double layer profile of counterions at each electrode, using as a boundary condition the instantaneous conducting ion concentration far from the electrode, effectively determining  $p$ , with  $\mu$  then calculated from Eq. 2-4.

The basic idea is that by using blocking electrodes the ions are allowed to polarize/accumulate near the electrodes at low frequency. The polarization of ions has two characteristics: (1) a significant increase of dielectric constant ( $\epsilon'$ ) due to the increased effective capacitance resulting from storing counterions at the electrodes and (2) a decrease of ionic conductivity ( $\sigma'$ ) due to the compensation of voltage by polarized ions (Figure 2-12(a)). Two important time scales can be defined to characterize EP (Eq. 2-5 and Eq. 2-6):

$$\tau_{\sigma} \equiv \frac{\epsilon_s \epsilon_0}{\sigma_{DC}} \quad (2-5)$$

$$\tau_{EP} \equiv \frac{\epsilon_{EP} \epsilon_0}{\sigma_{DC}} \quad (2-6)$$

Here  $\tau_{\sigma}$  is the time scale of conduction (where counterion mean square displacement becomes diffusive) and  $\tau_{EP}$  is the time scale for full electrode polarization.  $\epsilon_s$  is the static (low frequency) dielectric constant of the sample,  $\epsilon_{EP}$  is the dielectric constant when electrode polarization is complete and  $\epsilon_0$  is the vacuum permittivity. The

Macdonald/Coelho model assumes that EP can be described by a simple Debye relaxation so the loss tangent peak can be fit to Eq. 2-7

$$\tan \delta = \frac{\varepsilon''}{\varepsilon'} = \frac{\omega \tau_{EP}}{1 + \omega^2 \tau_{\sigma} \tau_{EP}} \quad (2-7)$$

to obtain  $\tau_{\sigma}$  and  $\tau_{EP}$  (the peak frequency corresponds to the onset of electrode polarization, the geometric mean of  $\tau_{\sigma}$  and  $\tau_{EP}$ ). Static dielectric constant can then be obtained from Eq. 2-5. By assuming that all anions are fixed on the polymer backbone and unable to move in the field, with no salt contaminants (single-ion conductors) the instantaneous conducting ion concentration and their mobility can be obtained (Eq. 2-8 and Eq. 2-9):

$$\mu = \frac{eL^2 \tau_{\sigma}}{4\tau_{EP}^2 kT} \quad (2-8)$$

$$p = \frac{\sigma_{DC}}{e\mu} = \frac{4\sigma_{DC} \tau_{EP}^2 kT}{e^2 L^2 \tau_{\sigma}} \quad (2-9)$$

where L is the sample thickness. Figure 2-7 displays the loss tangent data for different samples at  $T_g + 20K$  fit to Eq. 2-7. All the samples have the same  $\tan\delta$  shape, indicating that the polarization process does not change with different cations. As observed previously for single-ion conductors<sup>19,30,43</sup> the loss tangent data are somewhat broader than the Debye relaxation of Eq. 2-7, but the fitting provides robust measures of  $\tau_{\sigma}$  and  $\tau_{EP}$ , from which mobility and conducting ion content are calculated using Eq. 2-8 and Eq. 2-9, and  $\varepsilon_s$  is calculated using Eq. 2-5. Although the origins of the broader-than-Debye polarization are likely polymer/ion relaxation underneath EP, we fit EP to the broader Cole-Cole relaxation function<sup>48,50,51</sup> in section 2.3.8, resulting in better fits and

similar  $\tau_\sigma$ ,  $\tau_{EP}$ ,  $p$ , and  $\mu$ . Note that trapped counterions never participate in conduction and EP so they have no contribution to  $\sigma_{DC}$  and conducting ion content  $p$ , whereas all nontrapped counterions contribute to  $\sigma_{DC}$  beyond  $\tau_\sigma$ . Among the nontrapped counterions, conducting ion content  $p$  are the ones participating ionic conductivity in an instantaneous snapshot and they exchange with other nontrapped counterions beyond  $\tau_\sigma$  when conducting.

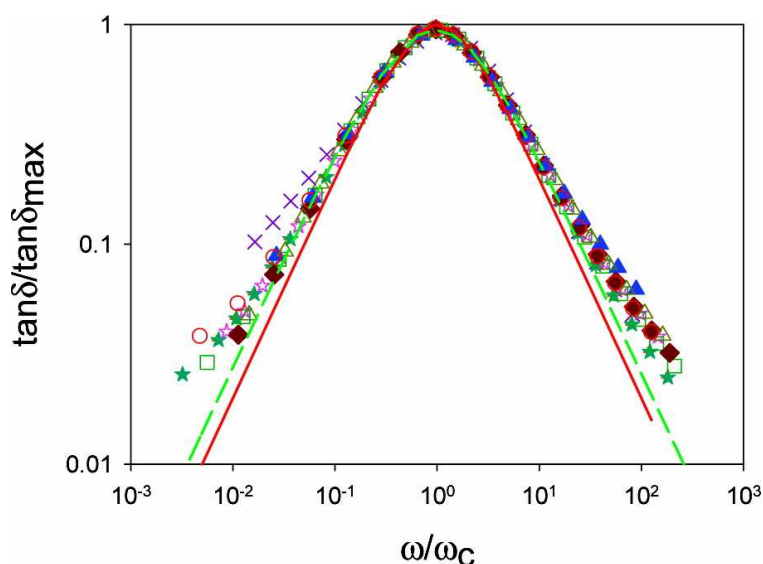


Figure 2-7: Fitted  $\tan\delta$  peak with Eq. 2-7 at  $T_g + 20$  K for different cations. X and Y axis are normalized with the peak value of  $\tan\delta$  and the geometric mean of  $\tau_\sigma$  and  $\tau_{EP}$ . Purple X is  $\text{Na}^+$ ; orange plus is  $\text{Me}_4\text{N}^+$ ; cyan solid star is  $\text{BuMeIm}^+$ ; pink open star is  $(\text{MOE})\text{MeIm}^+$ ; green open square is  $(\text{EOc})_2\text{Me}(\text{MOE})\text{N}^+$ ; dark red solid diamond is  $\text{Bu}_4\text{N}^+$ ; blue solid triangle is  $\text{Bu}_4\text{P}^+$ ; olive green open triangle is  $\text{Bu}_3(\text{MOE})\text{P}^+$ ; red open circle is  $(\text{MOEOE})_3\text{MeN}^+$ ; red solid line is best fitting for Eq. 2-7; green dashed line is best fitting for Eq. 2-22.

Eq. 2-5 provides a method to determine static dielectric constant  $\epsilon_s$ . In our system, the acid form precursor and  $\text{Na}^+$  ionomer have  $\epsilon_s = 14$  near room temperature while all other ionomers have higher  $\epsilon_s$ , which are between 20 to 30 (see Figure 2-12(b) in section 2.3.8). Some counterions form ion pairs (which have strong dipoles) with the carboxylate

and increase  $\epsilon_s$ <sup>43</sup>, whereas  $\text{Na}^+$  has too strong Coulombic interaction and the majority of  $\text{Na}^+$  are trapped in pPDI-carboxylate-pPDI segment, resulting in the same dielectric constant as the acid form precursor.

### 2.3.6 Concentrations of conducting ions and their mobility

Conducting ion concentrations are plotted as a function of inverse temperature in Figure 2-8. The temperature dependence of conducting ion concentration calculated from Eq. 2-9 obeys an Arrhenius equation as shown in Figure 2-8 (Eq. 2-10):

$$p = p_0 \exp\left(\frac{-E_a}{kT}\right) \quad (2-10)$$

where  $p_0$  is the conducting ion concentration at infinite temperature and  $E_a$  is an activation energy; these parameters are shown in Table 2-3. Note that although the total ion concentration is about  $6 \times 10^{20} \text{ cm}^{-3}$ , the “actual” amount of ions contributing to ionic conduction at any given time is much smaller and thermally activated, as reported previously.<sup>19,30,43,52</sup> (Here, we believe the conducting ions are triple ions instead of single ions.<sup>43,53</sup>) The activation energy decreases with increasing cation size as expected, except for  $\text{Na}^+$  and  $\text{Me}_4\text{N}^+$ . As discussed in the rheology section, our PU ionomers do not truly microphase separate but have local environments with different amount of pPDI-carboxylate-pPDI segments. The fact that  $p_0$  is smaller than  $6 \times 10^{20} \text{ cm}^{-3}$  indicates some of the counterions interact with these pPDI-carboxylate-pPDI segments too strongly to participate ionic conduction and the ratio  $p_0/6 \times 10^{20} \text{ cm}^{-3}$  tells us the fraction of counterions that are not trapped in these pPDI-carboxylate-pPDI rich local environments.

The observation that  $\text{Na}^+$  and  $\text{Me}_4\text{N}^+$  samples have much lower  $p_0$  and  $E_a$  suggest that the majority of ions are either trapped in pPDI-carboxylate-pPDI segments or aggregated, with few actually conducting.

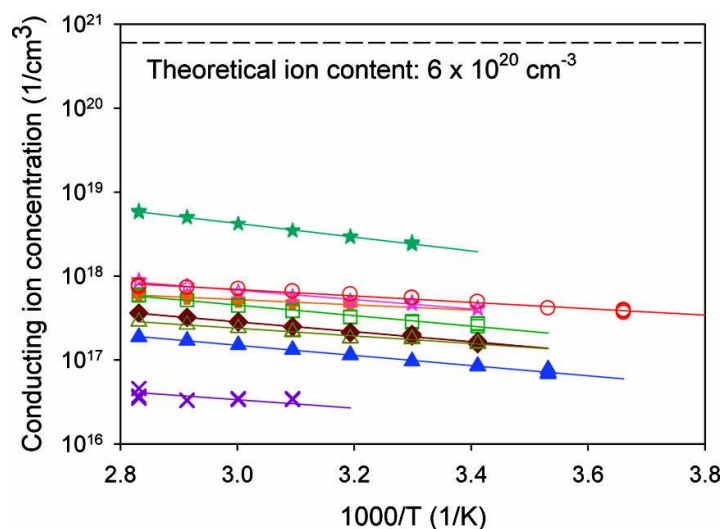


Figure 2-8: Conducting ion concentrations as functions of  $1000/T$ . Purple X is  $\text{Na}^+$ ; orange plus is  $\text{Me}_4\text{N}^+$ ; cyan solid star is  $\text{BuMeIm}^+$ ; pink open star is  $(\text{MOE})\text{MeIm}^+$ ; green open square is  $(\text{EOc})_2\text{Me}(\text{MOE})\text{N}^+$ ; dark red solid diamond is  $\text{Bu}_4\text{N}^+$ ; blue solid triangle is  $\text{Bu}_4\text{P}^+$ ; olive green open triangle is  $\text{Bu}_3(\text{MOE})\text{P}^+$ ; red open circle is  $(\text{MOE})_3\text{MeN}^+$ ; solid lines are the best fits to the Arrhenius equation (Eq. 2-10).

In our system  $p_0$ , the amount of conducting counterions at infinite temperature, which we interpret to be the nontrapped ions participating in conduction at any temperature, is generally less than the total ion content  $6 \times 10^{20} \text{ cm}^{-3}$  except the  $\text{BuMeIm}^+$  ionomer. This is consistent with our previous discussion of morphology in the rheology section: most counterions except  $\text{BuMeIm}^+$  are trapped in pPDI-carboxylate-pPDI segments.

Figure 2-9(a) plots mobility of the conducting ions against  $T_g/T$ , which is similar to the Figure 2-5 inset and Figure 2-6(b) inset. Like the  $\alpha$ -relaxation frequency, the mobility has a VFT temperature dependence (Eq. 2-11):

$$\mu = \mu_0 \exp\left(\frac{-DT_0}{T - T_0}\right) \quad (2-11)$$

and plotting against  $T_g/T$  merely reduces the data sets to a roughly one decade wide band. The solid curves in Figure 8 are fits of Eq. 2-11 with parameters summarized in Table 2-3. Unlike the  $\alpha$ -relaxation frequency, Vogel temperature  $T_0$  for mobility has a strong correlation with calorimetric  $T_g$  ( $T_g - T_0 \approx 65$  K).

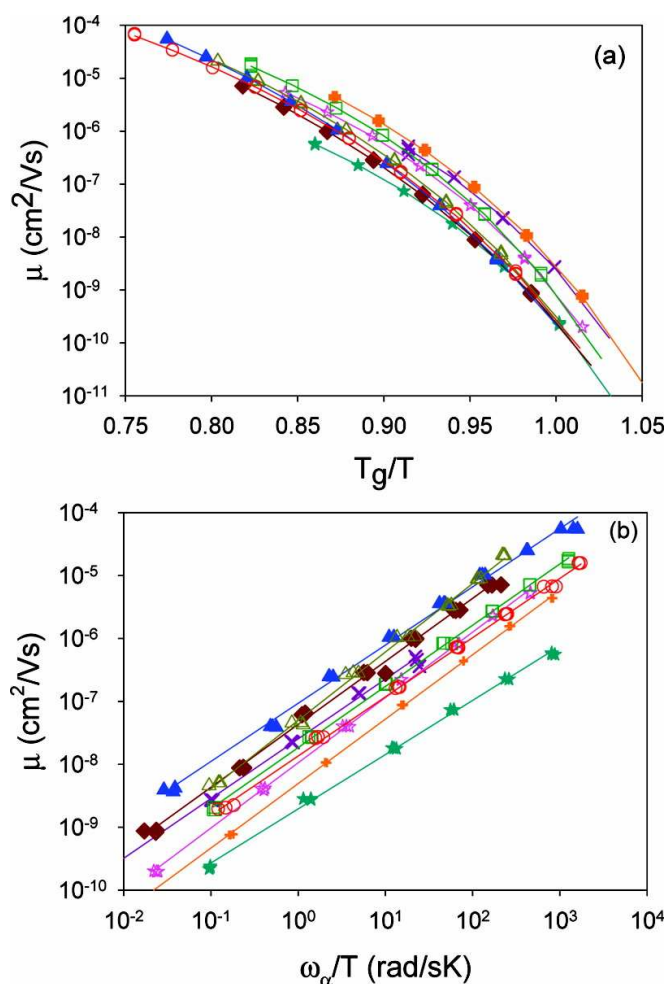


Figure 2-9: Cation mobility as function of (a)  $T_g/T$  (b)  $\alpha$  relaxation frequency/temperature. Purple X is  $\text{Na}^+$ ; orange plus is  $\text{Me}_4\text{N}^+$ ; cyan solid star is  $\text{BuMeIm}^+$ ; pink open star is  $(\text{MOE})\text{MeIm}^+$ ; green open square is  $(\text{EOc})_2\text{Me}(\text{MOE})\text{N}^+$ ; dark red solid diamond is  $\text{Bu}_4\text{N}^+$ ; blue solid triangle is  $\text{Bu}_4\text{P}^+$ ; olive green open triangle is  $\text{Bu}_3(\text{MOE})\text{P}^+$ ; red open circle is  $(\text{MOEOE})_3\text{MeN}^+$ ; solid lines are the best fit power laws.

Figure 2-9(b) shows the correlation of  $\alpha$ -relaxation frequency and conducting ion mobility, showing a slight decoupling (slope  $\sim 0.88$ -1.0). The origin of decoupling was generally considered as ion “hopping” transport under an electric field.<sup>43,54</sup> Figure 2-9(b) fails to collapse the data as well as Figure 2-6(b). A simple interpretation stems from the fact that all ions that are not trapped in pPDI-carboxylate-pPDI segments participate in conduction beyond  $\tau_\sigma$  and  $\omega_\alpha^{-1}$ . All non-trapped ions contribute equally to conduction. The average mobility is simply proportional to  $\sigma_{DC}$  and explains why the correlation between  $\sigma_{DC}$  and  $\omega_\alpha$  in Figure 2-6(b) works so well. In this scenario, the ionomer with sodium counterions simply has much more of  $\text{Na}^+$  trapped, with about 1/6 fewer ions participating in conduction. In contrast, more of the larger counterions participate in conduction with much less or no counterions trapped. The apparent slope somewhat smaller than unity in Figure 2-9(b) then is simply caused by the Arrhenius temperature dependence of instantaneous conducting ion content in Figure 2-8.

### 2.3.7 Actuation and electrode polarization (EP)

The Macdonald/Coelho EP model allows us to obtain the electrode polarization time scale  $\tau_{EP}$ , which is proportional to the electrode spacing  $L$  (sample film thickness).<sup>30</sup> A material property relevant for actuation,  $\tau_{EP}/L$  can be obtained from Eq. 2-5, Eq. 2-8 and Eq. 2-9: (Eq. 2-12)

$$\frac{\tau_{EP}}{L} = \frac{1}{\mu} \sqrt{\frac{\epsilon_S \epsilon_0}{4pkT}} \quad (2-12)$$

For fast actuation, ion-conducting membranes require small  $L$  and high conducting ion content  $p$  with high mobility  $\mu$ .

Actuation can be modeled as an equivalent resistor-capacitor circuit, with the time scale for polarization (or charging)  $\tau_{EP} = RC$ , where  $R$  is the resistance and  $C$  is the capacitance of the equivalent circuit. The actuation is created on time scale  $\tau_{EP}$  by a build-up of conducting ions in the Stern layer (within the Debye length of the electrode). The charge built up in the Stern layer  $Q$  can be described as a function of applied voltage:  $Q = CV = \tau_{EP}V/R$ , and the charge accumulation per unit electrode surface area  $A$  (charge density) can be calculated (Eq. 2-13)

$$\frac{Q}{A} = \frac{\tau_{EP}V}{RA} = \frac{\tau_{EP}V}{A} \frac{\sigma_{DC}A}{L} = \frac{\tau_{EP}}{L} V \sigma_{DC} \quad (2-13)$$

Hence, the charge density at the electrode is determined by the product of the material property  $\tau_{EP}/L$  and conductivity  $\sigma_{DC}$ . Combining Eq. 2-12 and Eq. 2-13, the charge density at the electrode can be rewritten as a function of conducting ion content  $p$  and static dielectric constant  $\epsilon_s$  (Eq. 2-14)

$$\frac{Q}{A} = Ve \sqrt{\frac{\epsilon_s \epsilon_0 p}{4kT}} \quad (2-14)$$

Increase of conducting ion content and/or static dielectric constant can increase the charge density of polarizing ions and therefore increases the strain in the actuator. If we consider the strain of the actuator to be induced by the volume change as the result of counterion accumulation at the electrode, then a dimensionless parameter relevant to the strain can be estimated by multiplying polarizing charge density by cation volume  $V_{\text{cation}}$  divided by electrode spacing  $L$  (Eq. 2-15)

$$\frac{QV_{cation}}{AeL} : V_{cation} \epsilon_s^{1/2} p^{1/2} \quad (2-15)$$

Figure 2-10(a) shows the volume of all polarized cations divided by membrane volume as a function of temperature with electrode spacing  $L$  of 100  $\mu\text{m}$ . The Na-ionomers would make poor actuators because of the small size and lower conducting ion content of  $\text{Na}^+$ . Ionic liquid counterions should have strain 30-100\_larger than  $\text{Na}^+$ . It is not surprising that the trend is similar to conducting ion content  $p$  in Figure 2-8 from its dependence on  $p^{1/2}$ . However, in Figure 2-10(a)  $(\text{MOEOE})_3\text{MeN}^+$  and  $\text{BuMeIm}^+$  have similar highest value unlike in Figure 2-8, suggesting the importance of counterion size for generating strain.

Eq. 2-13 and Eq. 2-14 also allow us to test the linear response assumption of the Macdonald/Coelhomodel. This model assumes that the build-up of ions near the electrode is sufficiently small that there is no interaction between ions polarized near the electrode. Nonlinear electrode polarization will occur when polarizing ions start to interact with each other - when they are separated by the Bjerrum length on the electrode surface (where their Coulomb repulsion equals to thermal energy, Eq. 2-16).

$$l_B = \frac{e^2}{4\pi\epsilon_0\epsilon_s kT} \quad (2-16)$$

The relevant dimensionless parameter,  $Ql_B^2/(Ae)$  the ions polarized per squared Bjerrum length, should be smaller than unity to ignore nonlinear effects and utilize the Macdonald/Coelho model to estimate conducting ion content (Eq. 2-17)

$$\frac{Ql_B^2}{Ae} = \frac{\tau_{EP} V \sigma_{DC} l_B^2}{Le} = \frac{\tau_{EP} e V \sigma_{DC} l_B}{4\pi\epsilon_0\epsilon_s kTL} < 1 \quad (2-17)$$

or (Eq. 2-18)

$$\frac{Ql_B^2}{Ae} = Vl_B^2 \sqrt{\frac{\epsilon_s \epsilon_0 p}{4kT}} = \frac{eV}{kT} \sqrt{\frac{pl_B^3}{16\pi}} < 1 \quad (2-18)$$

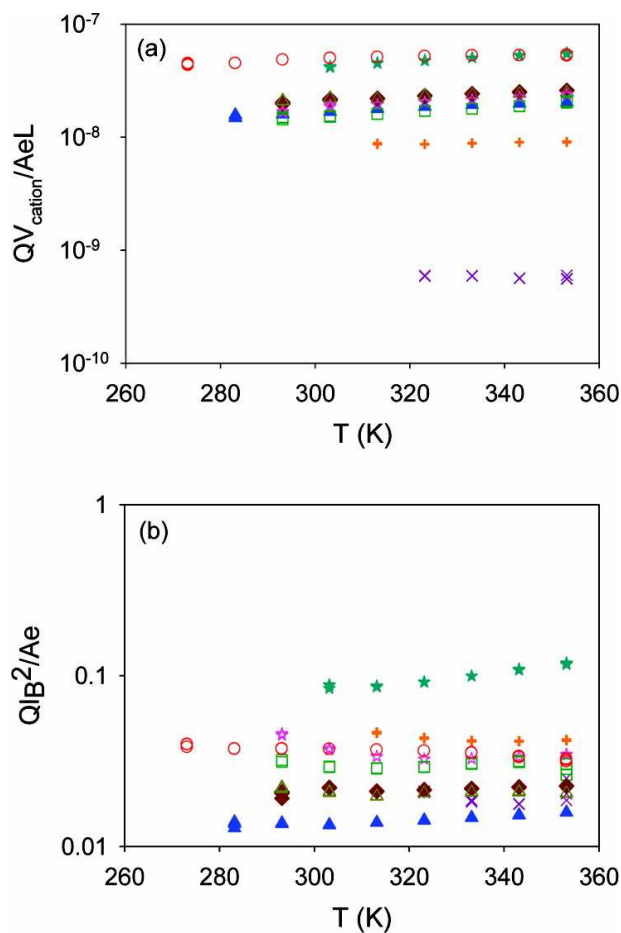


Figure 2-10: (a) Dimensionless strain relevant parameter (Eq. 2-15) as a function of temperature with electrode spacing of 100  $\mu\text{m}$  and assuming cations have density of 1  $\text{g}/\text{cm}^3$ . (b) Dimensionless charge density parameter (Eq. 18) as a function of temperature. The fact that  $Ql_B^2/Ae < 1$  suggests linear EP response. Purple X is  $\text{Na}^+$ ; orange plus is  $\text{Me}_4\text{N}^+$ ; cyan solid star is  $\text{BuMeIm}^+$ ; pink open star is  $(\text{MOE})\text{MeIm}^+$ ; green open square is  $(\text{EOc})_2\text{Me}(\text{MOE})\text{N}^+$ ; dark red solid diamond is  $\text{Bu}_4\text{N}^+$ ; blue solid triangle is  $\text{Bu}_4\text{P}^+$ ; olive green open triangle is  $\text{Bu}_3(\text{MOE})\text{P}^+$ ; red open circle is  $(\text{MOEOE})_3\text{MeN}^+$ .

Figure 2-10(b) shows this dimensionless parameter as a function of temperature. For all ionomers studied in this paper,  $Ql_B^2/Ae$  is in the range of 0.1 to 0.01, which is well below 1. This verifies that our ionomer system is in the linear region with 0.1 V applied, through the temperature range we study and justifies the linear assumption of the Macdonald/Coelho EP model we use to separate the conductivity into instantaneous conducting ion content  $p$  and their mobility  $\mu$ . Figure 2-10(a) also shows why real actuators require added ions, larger voltages and thinner films in the strongly nonlinear EP range for actuation, as the strains of order  $1 \times 10^{-8}$  at 0.1 V will not be observable.

### 2.3.8 EP model with Cole-Cole relaxation

Broader spectra than Debye prediction (Figure 2-7) are commonly observed for electrode polarization of ionomers.<sup>30,43,50,51</sup> Cole and Cole introduced a parameter  $\alpha$  to the Debye equation to allow a description of broadened relaxations that maintain symmetry on a log frequency scale,<sup>51</sup> (Eq. 2-19)

$$\epsilon_{EP}^* = \epsilon_s + \frac{\epsilon_{EP} - \epsilon_s}{1 + (i\omega\tau_0)^{1-\alpha}} \quad (2-19)$$

where  $0 < \alpha < 1$ . It is identical to the Debye equation when  $\alpha = 0$ . So  $\epsilon'$ ,  $\epsilon''$  and loss tangent  $\tan \delta$  can be derived<sup>16,51</sup> (Eq. 2-20, Eq. 2-21 and Eq. 2-22)

$$\epsilon_{EP}' = \epsilon_s + \frac{(\epsilon_{EP} - \epsilon_s) \left[ 1 + (\omega\tau_0)^{1-\alpha} \sin\left(\frac{1}{2}\alpha\pi\right) \right]}{1 + 2(\omega\tau_0)^{1-\alpha} \sin\left(\frac{1}{2}\alpha\pi\right) + (\omega\tau_0)^{2(1-\alpha)}} \quad (2-20)$$

$$\varepsilon_{EP}'' = \frac{(\varepsilon_{EP} - \varepsilon_s)(\omega\tau_0)^{1-\alpha} \cos(\frac{1}{2}\alpha\pi)}{1 + 2(\omega\tau_0)^{1-\alpha} \sin(\frac{1}{2}\alpha\pi) + (\omega\tau_0)^{2(1-\alpha)}} \quad (2-21)$$

$$\tan \delta = \frac{\varepsilon_{EP}''}{\varepsilon_{EP}'} = \left[ \frac{1}{(\omega\tau_0)^{1-\alpha} \cos(\frac{1}{2}\alpha\pi)} + \tan(\frac{1}{2}\alpha\pi) + \frac{\tau_\sigma}{\tau_{EP}} \frac{(\omega\tau_0)^{1-\alpha}}{\cos(\frac{1}{2}\alpha\pi)} \right]^{-1} \quad (2-22)$$

by the assumption  $\varepsilon_{EP} \gg \varepsilon_s$ .<sup>30</sup> The fitting is shown in Figure 2-7 (green dashed line). Note that  $\tau_0$  here is not the relaxation time in Eq. 2-7. Time scales of conduction  $\tau_\sigma$  and electrode polarization  $\tau_{EP}$  can be obtained by the fact that the maximum in  $\tan\delta$  is at the geometric mean of  $\tau_\sigma$  and  $\tau_{EP}$ . Eq. 2-23 gives the relationship between  $\tau_0$ ,  $\tau_\sigma$  and  $\tau_{EP}$ :

$$\tau_0 = \tau_\sigma^{\frac{\alpha}{2(\alpha-1)}} \tau_{EP}^{\frac{\alpha-2}{2(\alpha-1)}} \quad (2-23)$$

Figure 2-11 shows the comparison of  $\tau_\sigma$  and  $\tau_{EP}$  obtained by Eq. 2-7 and Eq. 2-23. It is interesting how well they agree with each other because the EP relaxations are only slightly broader than Debye, but  $\tau_{EP}$  increases slightly and  $\tau_\sigma$  decreases slightly with the broader Cole-Cole spectrum, as expected. For simplicity,  $\tau_\sigma$  and  $\tau_{EP}$  discussed in this paper are obtained by Eq. 2-7. Note that time temperature superposition does not apply to EP and the ratio  $\tau_{EP}/\tau_\sigma$  increases with temperature, due to the fact that conducting ion content weakly increases with temperature.

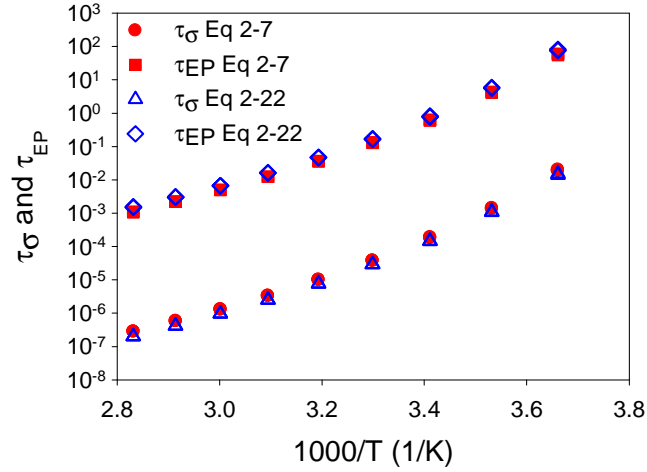


Figure 2-11: Comparison of  $\tau_\sigma$  and  $\tau_{EP}$  obtained from Eq. 2-7 (solid symbols) and Eq. 2-22 (open symbols) with  $\alpha = 0.007$ .

Static dielectric constant  $\epsilon_s$  is generally defined as the high frequency plateau of  $\epsilon'(\omega)$  spectra before electrode polarization begins, as shown in Figure 2-12(a). However, the exact value of the  $\epsilon'(\omega)$  plateau is rather difficult to be identified in ionomers because of the nonflat nature of  $\epsilon'(\omega)$  just before EP, indicating underlying relaxations. Several ways to determine  $\epsilon_s$  are summarized in Table 2-4 and the corresponding time scale and  $\epsilon_s$  are shown in panels a and b in Figure 2-12. Note that the time scales of ion conduction ( $\tau_\sigma$ , Eq. 2-5) and EP ( $\tau_{EP}$ , Eq. 2-6) are correlated by the fact that the peak frequency of  $\tan \delta$  is the geometric mean of these two time scales (Eq. 2-24).

$$\tau_{\tan \delta, \max} = \sqrt{\tau_\sigma \tau_{EP}} \quad (2-24)$$

Among the various measures of diffusivemotion of counterions (see Table A-1),  $\tau_{\sigma, \tan \delta} \sim \tau_{\sigma, \epsilon'} > \tau_{\sigma, \sigma''} > \tau_{\sigma, M''} > \tau_{\sigma, \sigma'}$  and  $\epsilon_{s, \tan \delta} \sim \epsilon_{s, \epsilon'} > \epsilon_{s, \sigma''} > \epsilon_{s, M''} > \epsilon_{s, \sigma'}$ .  $\tau_\sigma$  and  $\epsilon_s$  calculated from  $M''$  and  $\sigma''$  have much smaller value than other methods and are less suitable in our system. Notice that  $\epsilon_{s, M''}$  and  $\epsilon_{s, \sigma'}$  are even smaller than the dielectric constant of the acid form of

our polyurethane which is less likely because the ionomer form has much stronger dipole than the acid form (1.77 D) from *ab initio* calculations. For discussions in this paper, we adopt the static dielectric constant from fitting  $\tan \delta$  to the Debye function (Eq. 2-7) because it has good agreement with the  $\epsilon_s$  obtained from the plateau value before EP begins by subtracting the EP contribution ( $\sim \omega^n$ ) from  $\epsilon'(\omega)$ , and is more robust.

Table 2-4: Summary of different methods to obtain conduction time scale and static dielectric constants

Conduction time scale	Static dielectric constant	Physical meaning of the time scale	Method	Ref
$\tau_{\sigma, \tan \delta}$	$\epsilon_{S, \tan \delta}$	diffusive conduction	Eq(5) and (7)	30
$\tau_{\sigma, \epsilon'}$	$\epsilon_{\sigma, \epsilon'}$	diffusive conduction	Directly obtained from the plateau region of $\epsilon' - \omega^n$	
$\tau_{\sigma, \sigma''}$	$\epsilon_{\sigma, \sigma''}$	EP completed at $\sigma''_{\min} = \sigma''(\tau_{EP})$	$\sigma''_{\min} = \sigma''(\tau_{EP})$ and Eq (A-6)	55
$\tau_{\sigma, M''}$	$\epsilon_{\sigma, M''}$	hopping conduction	$M''_{\max} = M''(\tau_{\sigma, M''})$	55
$\tau_{\sigma, \sigma'}$	$\epsilon_{\sigma, \sigma'}$	hopping conduction	$\sigma'(\tau_{\sigma, \sigma'}) = 2\sigma_{DC}$	56

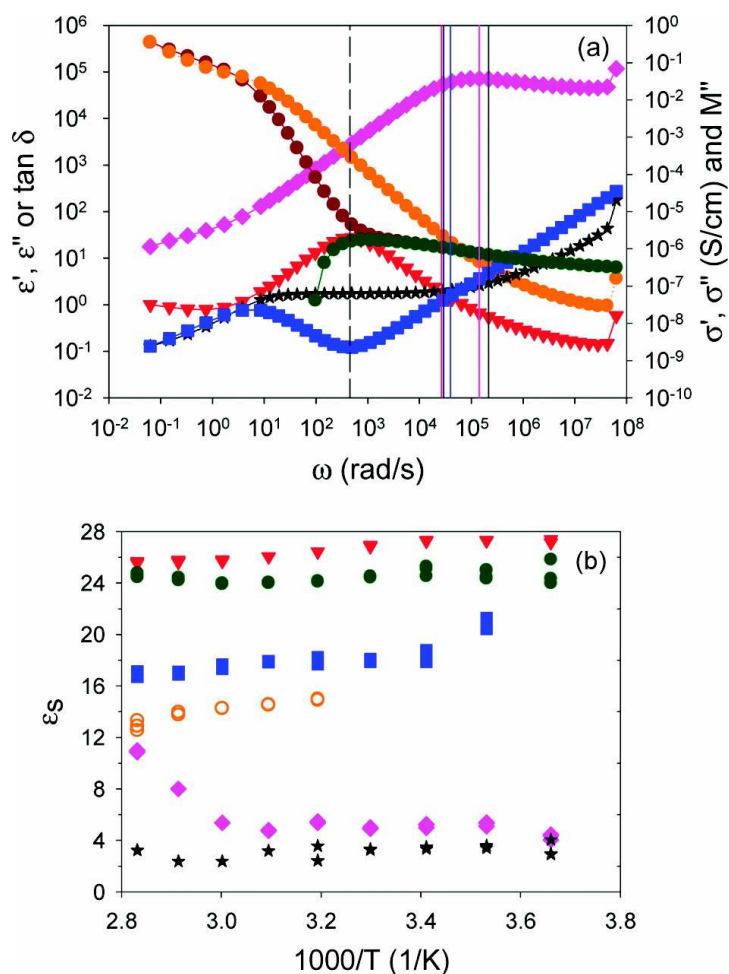


Figure 2-12: (a) Dielectric spectra for  $(\text{MOEOE})_3\text{MeN}^+$  at 30 °C. Left y axis: dark red circle is  $\epsilon'$ ; orange circle is  $\epsilon''$ ; red triangle is  $\tan \delta$ ; green circle is  $\epsilon'$  with EP subtracted as a power law. Right y axis: black star is  $\sigma'$ ; blue square is  $\sigma''$ ; pink diamond is  $M''$ . In the order of increasing frequency, the dashed line is the geometric mean of  $\tau_\sigma$  and  $\tau_{\text{EP}}$ ; red line is  $\tau_{\sigma, \tan \delta}$ ; green line is  $\tau_{\sigma, \epsilon'}$ ; blue line is  $\tau_{\sigma, \sigma''}$ ; pink line is  $\tau_{\sigma, M''}$ ; black line is  $\tau_{\sigma, \sigma'}$ . (b) Comparison of  $\epsilon_s$  obtained by different method: red triangle is  $\epsilon_{s, \tan \delta}$ ; green circle is  $\epsilon_{s, \epsilon'}$ ; blue square is  $\epsilon_{s, \sigma''}$ ; pink diamond is  $\epsilon_{s, M''}$ ; black star is  $\epsilon_{s, \sigma'}$ ; orange open circle is  $\epsilon_s$  for the acid form for reference.

## 2.4 Conclusion

Influence of various cationic counterions on both thermal and dielectric properties of PEO-based polyurethane carboxylate ionomers has been studied. Size and species of

cations play important roles. Generally, larger cations result in lower  $T_g$  because of weaker Coulombic attraction with anions.

Ionic conductivity in these single-ion conductors is strongly correlated with  $\alpha$ -relaxation frequency of PEO. This implies ion conduction is strongly coupled with polymer segmental relaxation, as expected for ionomers with strong solvation interaction between the polymer and counterions. Electrode polarization at low frequencies is used to determine conducting ion concentration and mobility. Conducting ion mobility shows VFT behavior with strong correlations to both polymer chain relaxation and  $T_g$ , while the conducting ion concentration has an Arrhenius temperature dependence. We found that significant amounts of counterions are trapped by pPDI-carboxylate-pPDI segments, with only small portions contributing to ionic conductivity. From the observed Arrhenius temperature dependence of instantaneous conducting ion content, about 90% of the counterions are trapped in pPDI-carboxylate-pPDI segment for most of the ionomers except BuMeIm<sup>+</sup>, which has almost no trapped counterions and Na<sup>+</sup>, which has more than 98% trapped. At any instantaneous snapshot, the Na<sup>+</sup> sample has fewer than 0.01% conducting ions. Me<sub>4</sub>N<sup>+</sup> has about 0.1% conducting and all other larger cations have 0.1-1% of the cations conducting. Unfortunately, while pPDI strongly microphase separates in neutral polyurethane,<sup>21</sup> interaction with ions and PEO prevents discrete microphase separation in pPDI-PEO-ionomers. Consequently the modulus is too low for these materials to be useful as ionic actuators.

We have proven that larger counterions lower  $T_g$  and boost ion conductivity, with our custom-synthesized ammonium with three ethylene oxide tails having by far the highest ionic conductivity. That counterion shows great promise for ionic actuators,

which need large counterions for large strain and high ionic conductivity for fast response. To further improve conductivity, large phosphonium cations with a suitable amount of ether oxygen atoms attached in a high dielectric constant ion solvating polymer matrix is the direction to increase both conducting ion concentration and cation mobility.

## 2.5 References

1. Fenton, D. E.; Parker, J. M.; Wright, P. V. *Polymer* **1973**, 14, 589.
2. Meyer, W. H. *Adv. Mater.* **1998**, 10, 439–448.
3. Gadjourova, Z.; Andreev, Y. G.; Tunstall, D. P.; Bruce, P. G. *Nature* **2001**, 412, 520–523.
4. Snyder, J. F.; Carter, R. H.; Wetzel, E. D. *Chem. Mater.* **2007**, 19, 3793–3801.
5. Singh, M.; Odusanya, O.; Wilmes, G. M.; Eitouni, H. B.; Gomez, E. D.; Patel, A. J.; Chen, V. L.; Park, M. J.; Fragouli, P.; Iatrou, H.; Hadjichristidis, N.; Cookson, D.; Balsara, N. P. *Macromolecules* **2007**, 40, 4578–4585.
6. Gomez, E. D.; Panday, A.; Feng, E. H.; Chen, V.; Stone, G. M.; Minor, A. M.; Kisielowski, C.; Downing, K. H.; Borodin, O.; Smith, G. D.; Balsara, N. P. *Nano Lett.* **2009**, 9, 1212–1216.
7. Ramesh, S.; Radhakrishnan, G. J. *Polym. Mater.* **1999**, 16, 135–153.
8. Ding, Y. S.; Register, R. A.; Yang, C.-z.; Cooper, S. L. *Polymer* **1989**, 30, 1204–1212.
9. Visser, S. A.; Cooper, S. L. *Macromolecules* **1991**, 24, 2576–2583.
10. Williams, S. R.; Wang, W.; Winey, K. I.; Long, T. E. *Macromolecules* **2008**, 41, 9072–9079.
11. Yang, C.-Z.; Grasel, T. G.; Bell, J. L.; Register, R. A.; Cooper, S. L. *J. Polym. Sci., Part B: Polym. Phys.* **1991**, 29, 581–588.
12. Chen, S.-A.; Hsu, J.-S. *Polymer* **1993**, 34, 2769–2775.
13. Lee, D.-c.; Register, R. A.; Yang, C.-z.; Cooper, S. L. *Macromolecules* **1988**, 21, 1005–1008.
14. Xu, H.-S.; Yang, C.-Z. *J. Polym. Sci., Part B: Polym. Phys.* **1995**, 33, 745–751.
15. Jayakumar, R.; Nanjundan, S.; Prabakaran, M. *J. Macromol. Sci., Part C: Polym. Rev.* **2005**, 45, 231–261.
16. Kremer, F.; Schonhals, A. *Broadband Dielectric Spectroscopy*; Springer: New York, **2003**.
17. Pissis, P.; Polizos, G. In *Handbook of Condensation Thermoplastic Elastomers*; Fakirov, S., Ed.; Wiley-VCH: Weinheim, Germany, **2005**, pp 381–434.

18. Polizos, G.; Georgoussis, G.; Kyritsis, A.; Shilov, V. V.; Shevchenko, V. V.; Gomza, Y. P.; Nesin, S. D.; Klimenko, N. S.; Wartewig, S.; Pissis, P. *Polym. Int.* **2000**, 49, 987–992.
19. Fragiadakis, D.; Dou, S.; Colby, R. H.; Runt, J. *Macromolecules* **2008**, 41, 5723–5728.
20. Wei, X.; Yu, X. *J. Polym. Sci., Part B: Polym. Phys.* **1997**, 35, 225–232.
21. Sheth, J. P.; Klinedinst, D. B.; Wilkes, G. L.; Yilgor, I.; Yilgor, E. *Polymer* **2005**, 46, 7317–7322.
22. Ishida, M.; Yoshinaga, K.; Horii, F. *Macromolecules* **1996**, 29, 8824–8829.
23. Becke, A. D. *J. Chem. Phys.* **1993**, 98, 5648–5652.
24. Lee, C. T.; Yang, W. T.; Parr, R. G. *Phys. Rev. B* **1988**, 37, 785–789.
25. Vosko, S. H.; Wilk, L.; Nusair, M. *Can. J. Phys.* **1980**, 58, 1200–1211.
26. Stephens, P. J.; Devlin, F. J.; Chabalowski, C. F.; Frisch, M. J. *J. Phys. Chem.* **1994**, 98, 11623–11627.
27. Liu, W. Doctoral Dissertation, The Pennsylvania State University, State College, PA, **2011**.
28. Al-Salah, H. A.; Frisch, K. C.; Xiao, H. X.; McLean, J. A., Jr. *J. Polym. Sci., Part A: Polym. Chem.* **1987**, 25, 2127–2137.
29. Chen, H.; Chen, D.; Fan, Q.; Yu, X. *J. Appl. Polym. Sci.* **2000**, 76, 2049–2056.
30. Klein, R. J.; Zhang, S.; Dou, S.; Jones, B. H.; Colby, R. H.; Runt, J. *J. Chem. Phys.* **2006**, 124, 144903.
31. Eisenberg, A. *Macromolecules* **1971**, 4, 125–128.
32. Weiss, R. A.; Agarwal, P. K.; Lundberg, R. D. *J. Appl. Polym. Sci.* **1984**, 29, 2719–2734.
33. Eisenberg, A.; Kim, J.-S. *Introduction to Ionomers*; Wiley-Interscience: New York, **1998**.
34. Pauling, L. *The Nature of the Chemical Bond and the Structure of Molecules and Crystals: An Introduction to Modern Structural Chemistry*, 3rd ed.; Cornell University Press: Ithaca, NY, **1960**.
35. Weiss, R. A.; Agarwal, P. K. *J. Appl. Polym. Sci.* **1981**, 26, 449–462.
36. Weiss, R. A.; Stamato, H. *Polym. Eng. Sci.* **1989**, 29, 134–139.
37. Velankar, S.; Cooper, S. L. *Macromolecules* **1998**, 31, 9181–9192.
38. Velankar, S.; Cooper, S. L. *Macromolecules* **2000**, 33, 395–403.
39. Han, C. D. In *Rheology and Processing of Polymeric Materials*; Oxford University Press: New York, **2007**; Vol. 1, pp 484–486.
40. Lu, X.; Weiss, R. A. *Macromolecules* **1995**, 28, 3022–3029.
41. Smith, G. D.; Borodin, O.; Li, L. Y.; Kim, H.; Liu, Q.; Bara, J. E.; Gin, D. L.; Nobel, R. *Phys. Chem. Chem. Phys.* **2008**, 10, 6301–6312.
42. Huang, K.; Han, X.; Zhang, X.; Armstrong, D. W. *Anal. Bioanal. Chem.* **2007**, 389, 2265–2275.
43. Fragiadakis, D.; Dou, S.; Colby, R. H.; Runt, J. *J. Chem. Phys.* **2009**, 130, 064907.
44. Wubbenhorst, M.; van Turnhout, J. *J. Non-Cryst. Solids* **2002**, 305, 40–49.
45. Zhang, S.; Dou, S.; Colby, R. H.; Runt, J. *J. Non-Cryst. Solids* **2005**, 351, 2825–2830.

46. Angell, C. A. *Proc. Natl. Acad. Sci. U.S.A.* **1995**, 92, 6675–6682.
47. Borodin, O.; Smith, G. D. *Macromolecules* **2006**, 39, 1620–1629.
48. Macdonald, J. R. *Phys. Rev.* **1953**, 92, 4–17.
49. Coelho, R. *J. Non-Cryst. Solids* **1991**, 131-133, 1136–1139.
50. Macdonald, J. R. *J. Chem. Phys.* **1974**, 61, 3977–3996.
51. Cole, K. S.; Cole, R. H. *J. Chem. Phys.* **1941**, 9, 341–351.
52. Ratner, M. A.; Shriver, D. F. *Chem. Rev.* **1988**, 88, 109–124.
53. Bruce, G.; Gray, F. M. in *Solid State Electrochemistry*, Cambridge University Press: Cambridge, **1995**.
54. Ratner, M. A.; Nitzan, A. *Faraday Discuss. Chem. Soc.* **1989**, 88, 19–42.
55. Sangoro, J. R.; Serghei, A.; Naumov, S.; Galvosas, P.; Karger, J.; Wespe, C.; Bordusa, F.; Kremer, F. *Phys. Rev. E* **2008**, 77, 051202.
56. Dyre, J. C.; Maass, P.; Roling, B.; Sidebottom, D. L. *Rep. Prog. Phys.* **2009**, 72, 046501.

## Chapter 3

### X-ray Scattering and Infrared Studies for Polyurethane Ionomers with Ions in the Hard Segment

#### 3.1 Introduction

In the previous chapter, anionic polyurethane ionomers with different ionic liquid type counterions were synthesized and characterized by DSC, DRS and rheology. All characterization methods suggest the same morphology: no discrete microphase separation but there is most likely a local environment involving both pPDI and ions. To further understand the morphology and the local environment, X-ray scattering and Fourier transform infrared spectroscopy (FTIR) techniques can be very good options. X-ray scattering is a very useful tool for probing microphase separation in polyurethane materials.<sup>1-5</sup> The size of the hard domain is usually around 10 nm ( $q \sim 0.6 \text{ nm}^{-1}$ ) which can be seen in the small angle spectra<sup>6</sup> and there are well established models to interpret the morphology from SAXS<sup>1, 2, 7, 8</sup>. FTIR is also commonly used to study polyurethane materials: from in-situ diisocyanate reaction kinetics study in polyurethane/urea synthesis<sup>9, 10</sup>, understanding the hydrogen bonding condition between urethane linkages, soft segment ether or ionic groups,<sup>11-15</sup> to degradation studies<sup>16, 17</sup>. At the same time, temperature and time dependence of the formation of hydrogen bonding and microphase separation can be characterized with both techniques and provides a better understanding of the kinetics and mechanism of microphase separation of polyurethane<sup>14, 18-20</sup>.

In this chapter, room temperature X-ray scattering and FTIR spectra are reported. Both techniques show the same conclusion of no discrete microphase separation as was concluded in Chapter 2 on the same samples. However, there are still differences in hydrogen bonding amount in urethane N-H, C=O as well as ether oxygen region between neutral, acid form and ionomer samples. Temperature dependence of these hydrogen bonding interactions will also be discussed.

## 3.2 Materials and Experimental Methods

### 3.2.1 Materials

PU ionomer samples with ionic group in the hard segment and ionic liquid type counterions studied in this chapter were the same sample set as in Chapter 2 except the neutral sample. Please refer to Section 2.2.1 for chemical structures and synthesis details.

Neutral sample was synthesized with the same method as described in Chapter 2 except 2,2-diethyl-1,3-propanediol (purchased from Sigma-Aldrich) was used instead of 2,2-bis(hydromethyl)butyric acid. Polymer structure is shown in Figure 3-1. The neutral sample has only one DSC  $T_g$  at 11°C.

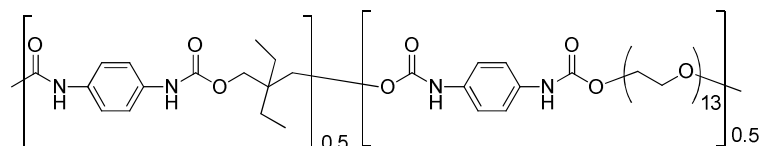


Figure 3-1: Chemical structure of the neutral sample.

---

### 3.2.2 Experimental methods

**X-ray scattering** All samples were dried and annealed at 80°C for 2 days as in Chapter 2 before measurement. A CuK $\alpha$  source from a Nonius FR591 rotating-anode generator operated at 40kV and 85mA was used for the X-ray scattering system at University of Pennsylvania. The bright, highly collimated beam was obtained via Osmic Max-Flux optics and triple pinhole collimation under vacuum. The scattering data were collected at room temperature using a Bruker Hi-Star multiwire detector with sample to detector distances of 7, 11, 54, and 150cm. The 2-D data reduction and analysis were performed using the Datasqueeze software<sup>21, 22</sup>. Background scattering was subtracted from the data. Thanks go to Wenqin (Sunny) Wang for acquiring and analyzing the X-ray data.

**Fourier transform infrared spectroscopy (FTIR)** Selected samples were first dissolved in DMF with a concentration of 2 wt% and the solution was dropped (~ 3 drops) onto a KBr window, dried at room temperature in hood for a day and then dried in a vacuum oven at 80°C to remove solvent. Samples are further dried in the equipment and confirmed to have no water absorbance peak before measurement. The absorbance spectra were collected using a Nicolet 450 FTIR spectrometer with a resolution of 2 cm<sup>-1</sup>. 20 min annealing was allowed for each isothermal measurement. Thanks go to Kyle Hart and Meredith Muskovich for acquiring FTIR data.

### 3.3 Results and Discussions

#### 3.3.1 X-ray scattering

The neutral sample was also studied as a control experiment, to investigate the effect of the presence of both carboxylic acid group and counterions. Figure 3-2 shows the comparison between neutral, acid form, and Na<sup>+</sup> salt. A very clear PEO amorphous halo can be seen at  $q \sim 15 \text{ nm}^{-1}$  as in PEO-based polyesters<sup>21</sup>. No crystalline PEO was observed in all samples, since the PEO used here only has  $\sim 13$  repeat units ( $M_w = 600$ ). There is also another unclear shoulder at  $q \sim 7 \text{ nm}^{-1}$  (green dashed arrow) that appears in all three samples, which may correspond to the distance between two aromatic rings (Figure 3-3). The neutral sample has another broad weak peak at  $q \sim 3 \text{ nm}^{-1}$  (black arrow) which is not seen in the other two samples. This peak was attributed to the intramolecular scattering from pPDI<sup>23</sup>. One may expect microphase separation from this peak, but it is very difficult to determine the microphase separation in this neutral sample. Generally, a microphase separation peak of polyurethanes appears at  $\sim 0.16 - 3 \text{ nm}^{-1}$  ( $\sim 40 - 2 \text{ nm}$  size)<sup>6, 24-26</sup>. Low  $q$  upturns in Figure 3-2 can be observed. However, it is difficult to say it is from microphase separation or concentration fluctuation or other causes<sup>26</sup>, as all ionomers have qualitatively similar low  $q$  upturns. The acid form sample does not present any other peaks, suggesting it is even more uniform, which is likely due to carboxylic acid groups that can also act as hydrogen bond donors and acceptors thus interrupting the hydrogen bonds between urethane linkage or bind to the ether groups in the soft segment. This stronger interaction as well explains the higher  $T_g$  of the acid form ( $23^\circ\text{C}$ ) compared to the neutral form. After neutralizing with NaOH, a broad weak peak appears at  $\sim 1 \text{ nm}^{-1}$

(purple dashed arrow). This peak can be attributed to ion aggregates<sup>21</sup>, microphase separation of hard and soft phase<sup>6</sup> or both. The breadth of this  $\sim 1 \text{ nm}^{-1}$  peak suggests a wide range of spacings (3-15nm).

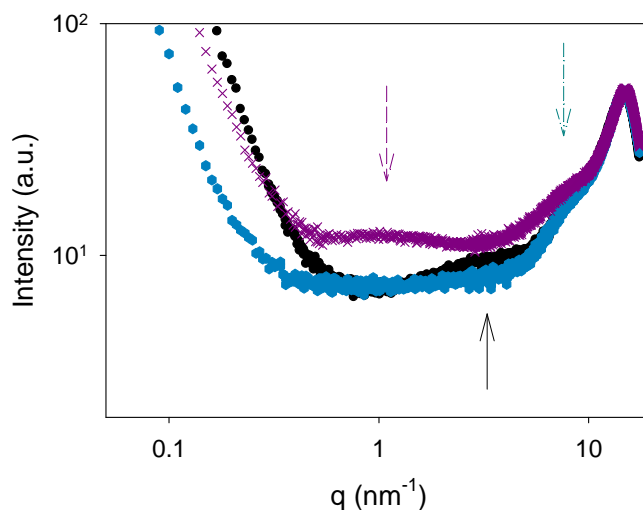


Figure 3-2: Comparison of X-ray scattering spectra for neutral (black circle), acid form (light blue hexagon) and  $\text{Na}^+$  (purple x) samples. Data are vertically shifted to have the same the amorphous halo intensity.

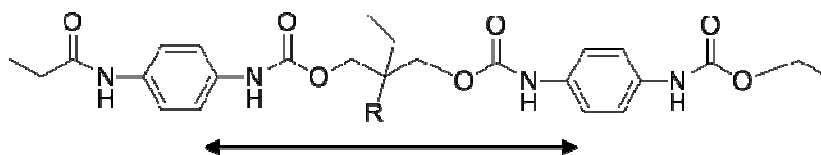


Figure 3-3: Spacing corresponding to the peak at  $q \sim 7 \text{ nm}^{-1}$ .  $R = -\text{COO}^-$  or  $-\text{C}_2\text{H}_4$ .

Figure 3-4 compares samples with  $\text{Na}^+$ ,  $\text{Me}_4\text{N}^+$ ,  $\text{BuMeIm}^+$ ,  $\text{Bu}_4\text{N}^+$  and  $\text{Bu}_4\text{P}^+$  counterions. The weak broad peak at  $1 \text{ nm}^{-1}$  in  $\text{Na}^+$  was not observed in samples with larger counterions, suggesting it may more be related to ion aggregates since it has much stronger Coulombic interaction from its smaller ion size. At the same time, the peak at  $7 \text{ nm}^{-1}$  ( $0.9 \text{ nm}$ , the average spacing of ions is  $\sim 1.2 \text{ nm}$  from the theoretical ion content

calculated from chemical structure) increases with alkyl chain length due to the increase of contrast between the carbon rich alkyl chain and the PEO-based matrix. This can be verified by comparing the difference between samples having counterions with and without ether oxygen on the alkyl chain in Figure 3-5. The increase of peak intensity at  $\sim 7 \text{ nm}^{-1}$  only happens with increase of alkyl chain length or amount instead of size, since  $(\text{MOEOE})_3\text{MeN}^+$  has the largest cation size but does not have a clear peak. It can be seen even more clearly on the linear scale in Figure 3-6. We can also see  $\text{Bu}_4\text{P}^+$  shows a slightly higher intensity than  $\text{Bu}_4\text{N}^+$ , due to larger atomic number of phosphorous than nitrogen. The PEO amorphous peak position is basically independent of counterions, while the pPDI-carboxylate-pPDI peak slightly moves to lower  $q$  with increasing counterion size, possibly due to steric hindrance of large ions.

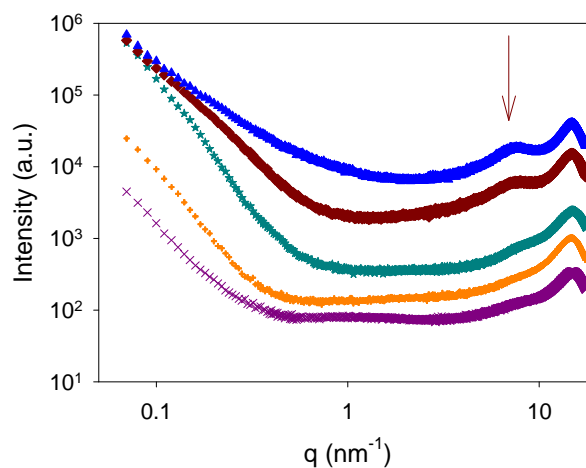


Figure 3-4: X-ray scattering spectra of  $\text{Na}^+$  (purple x),  $\text{Me}_4\text{N}^+$  (orange plus),  $\text{MeBuIm}^+$  (cyan star),  $\text{Bu}_4\text{N}^+$  (dark red diamond) and  $\text{Bu}_4\text{P}^+$  (blue triangle) samples. Data are vertically shifted for clarity.

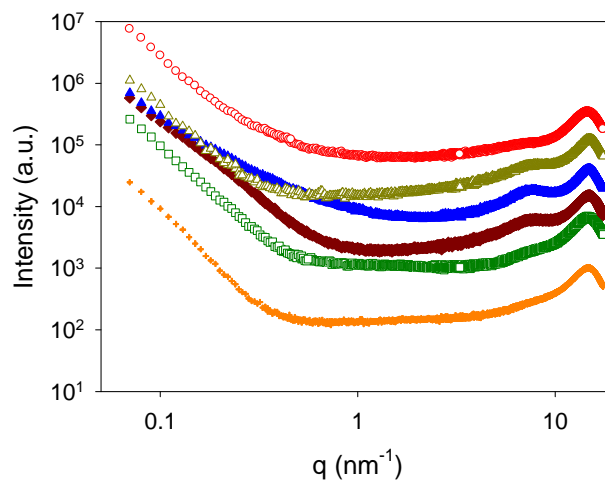


Figure 3-5: X-ray scattering spectra of  $\text{Me}_4\text{N}^+$  (orange plus),  $(\text{EOc})_2\text{Me}(\text{MOE})\text{N}^+$  (open green square),  $\text{Bu}_4\text{N}^+$  (dark red diamond),  $\text{Bu}_4\text{P}^+$  (blue triangle),  $\text{Bu}_3(\text{MOE})\text{P}^+$  (olive green open triangle), and  $(\text{MOEOE})_3\text{MeN}^+$  (red open circle) samples. Samples with ether-oxygen containing cations are shown with open symbols, otherwise with solid symbols. Data are vertically shifted for clarity.

---

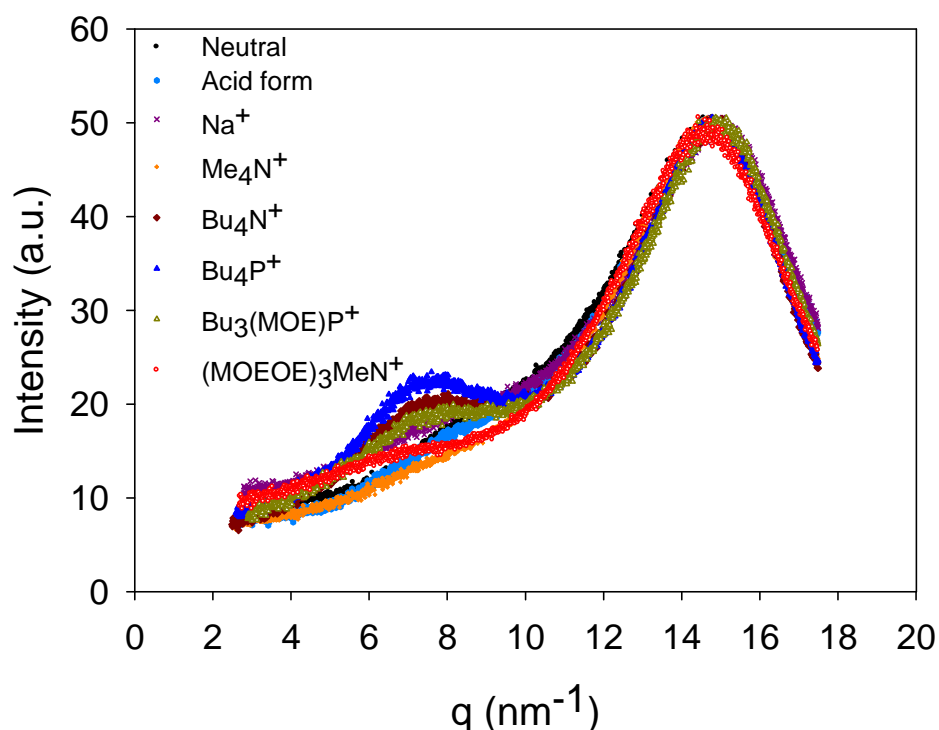


Figure 3-6: Linear scale wide angle X-ray scattering spectra. Neutral: black circle; acid form: light blue hexagon;  $\text{Na}^+$ : purple x;  $\text{Me}_4\text{N}^+$ : orange plus;  $\text{Bu}_4\text{N}^+$ : dark red diamond;  $\text{Bu}_4\text{P}^+$ : blue triangle;  $\text{Bu}_3(\text{MOE})\text{P}^+$ : olive green open triangle;  $(\text{MOEOE})_3\text{MeN}^+$ : red open circle. Samples with ether-oxygen containing cations are shown with open symbols, otherwise with solid symbols. Data are normalized to show the same amorphous peak intensity.

### 3.3.2 Fourier transform infrared study (FTIR)

Since the driving force of polyurethane to microphase separate is the strong hydrogen bond between urethane linkages, it is very useful to study the hydrogen bond condition through FTIR studies<sup>27</sup>. Figure 3-7 shows the full FTIR spectra from 800 to 4000  $\text{cm}^{-1}$  of selected samples studied at 30°C. All samples have similar spectra owing to their similar molecular structures (the different salts are the same ionomer with different

counterions). For easier discussion, Figure 3-8 shows only the stretching peak of the urethane carbonyl group. Both neutral and acid form sample have a free C=O peak at  $1730\text{ cm}^{-1}$  and a disordered, hydrogen bonded peak at  $1708\text{ cm}^{-1}$  which agrees with Yilgor et al published results in 2006 on pPDI based polyurethanes<sup>28</sup>. No ordered, hydrogen bonded peak at  $1695\text{ cm}^{-1}$  was observed in all studied samples since ether oxygens in the soft segment strongly interact with the urethane linkage<sup>28, 29</sup>. This also suggests no clear microphase separation, as in previously discussed DSC, SAXS, rheology and DRS studies. The free carbonyl peak shifts to  $1720\text{ cm}^{-1}$  after neutralization and is independent of the type of counterion. The shift to lower wavenumber can possibly due to stronger interaction of the free carbonyl groups with cationic counterions<sup>15, 30</sup>.

---

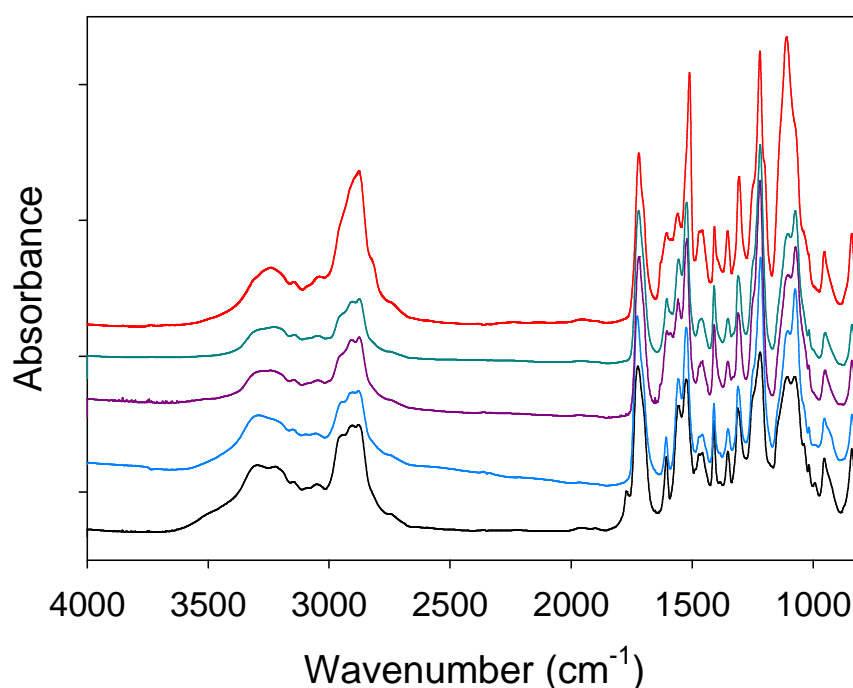


Figure 3-7: FTIR spectra of (from bottom to top) neutral (black), acid form (blue), Na<sup>+</sup> (purple), BuMeIm<sup>+</sup> (cyan) and (MOE)OEt<sub>3</sub>MeN<sup>+</sup> (red) samples at 30°C.

---

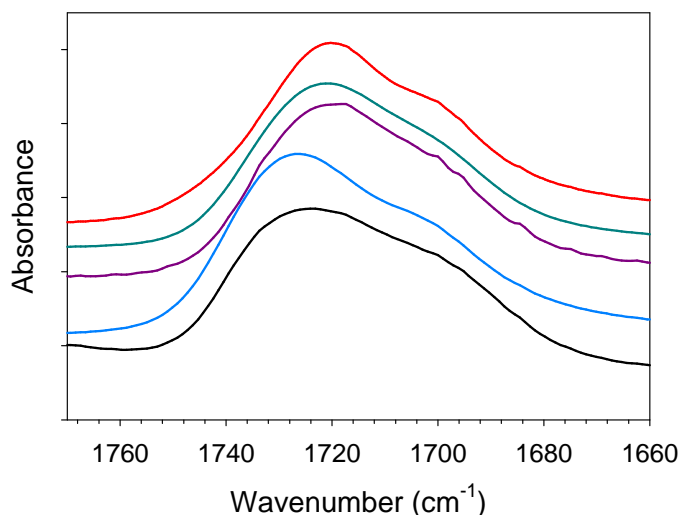


Figure 3-8: Carbonyl stretching region of neutral (black), acid form (blue), Na<sup>+</sup> (purple), BuMeIm<sup>+</sup> (cyan) and (MOE)₃MeN<sup>+</sup> (red) samples at 30°C.

Another region worth considering is the N-H stretching at 3300 – 3600 cm<sup>-1</sup>, displayed in Figure 3-9. Generally, N-H can be free, hydrogen bonded to carbonyl or ether groups<sup>11, 31, 32</sup> or anions. Two clear absorbance peaks can be observed and assigned to free and bonded N-H (~ 3300 and 3220 cm<sup>-1</sup>, respectively). In the neutral sample, there are similar amounts of free and bonded N-H. Free N-H increases with the presence of carboxylic acid (blue) and this agrees with the increase of free urethane C=O group and better phase mixing from SAXS. After neutralization with counterions, the bonded N-H peak increases due to bonded to negatively charged carboxylate group<sup>33</sup>. It is interesting that (MOE)₃MeN<sup>+</sup> has a much larger bonded peak, which is possibly from N-H bonded to ether oxygen on (MOE)₃MeN<sup>+</sup>. It would be very useful to further investigate the individual contributions from each peak with curve resolving. Unfortunately, the data shown here do not have a flat baseline, which is critical for reliable curve resolving.

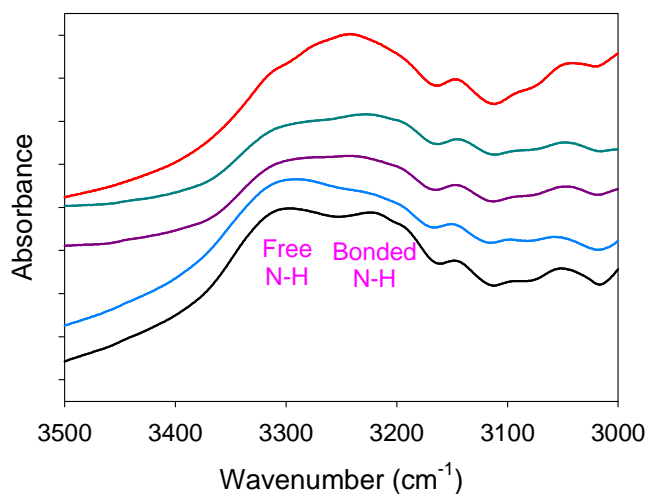


Figure 3-9: N-H stretching region of neutral (black), acid form (blue), Na<sup>+</sup> (purple), BuMeIm<sup>+</sup> (cyan) and (MOE)₃MeN<sup>+</sup> (red) samples at 30°C.

Besides the C=O and N-H regions, ether group absorbance from C-O-C stretching is shown in Figure 3-10. The two ether peaks at  $\sim 1105$  and  $\sim 1074$  cm<sup>-1</sup> are assigned to free and bonded ether groups<sup>28, 34</sup>. One thing that needs to be noticed is that the O=C-O of urethane also has an absorbance peak at around 1070-1120 cm<sup>-1</sup> although it is not as strong as the ether group<sup>17</sup> and there are  $\sim 13$  ethers/4 urethane linkages. Luckily, urethane O=C-O also has an out-of-plane peak at 750-830 cm<sup>-1</sup>, which is very similar for all samples so we can assume that the absorbance from O=C-O is the same in this region and the difference is caused by the different conditions of the ether groups. From neutral to acid form, the bonded ether peak increases, due to both bonding to the urethane N-H and the carboxylic acid, indicating phase mixing. After neutralization with counterions, this peak decreases slightly, possibly from both a decrease of bonding to the urethane and to the carboxylic acid but also an increase of bonding to cations<sup>34</sup>. (MOE)₃MeN<sup>+</sup>

shows significantly larger non-bonded peak because of many more ether groups compared to other samples.

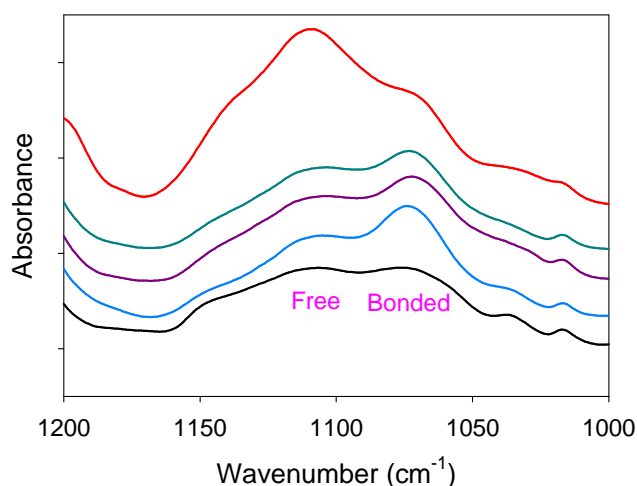


Figure 3-10: Ether group (C-O-C) region of neutral (black), acid form (blue), Na<sup>+</sup> (purple), BuMeIm<sup>+</sup> (cyan) and (MOE)<sub>3</sub>MeN<sup>+</sup> (red) samples at 30°C.

Temperature studies were also done for the neutral and BuMeIm<sup>+</sup> samples. Figure 3-11 shows temperature effect on both urethane C=O and N-H region for the neutral sample. As expected, the bonded peak decreases and free peak increases at temperature increases<sup>28, 31</sup>. The BuMeIm<sup>+</sup> sample shows similar behavior in Figure 3-12. The spectra during cooling down to 30°C were also recorded and are shown as dash-dot lines. It is interesting that hysteresis in the bonded peak growth during cooling can be observed and the full spectra were not recovered after cooling. This can be due to (1) polymer chemically changed, (2) residual solvent evaporated, (3) the hydrogen bond process did not reach equilibrium when spectra were collected, or some combination of the three. Through TGA, it was found that the onset of significant degradation is at about 150°C and DRS also showed evidence of stable spectra under 80°C so it is less likely to

be reason (1). At the same time, hydrogen bonding in polyurethane usually happens gradually and this process can require days<sup>28</sup> so this may be the origin of the observed hysteresis. To further confirm the causes of this hysteresis, annealing study over hours at different temperatures should be tried.

---

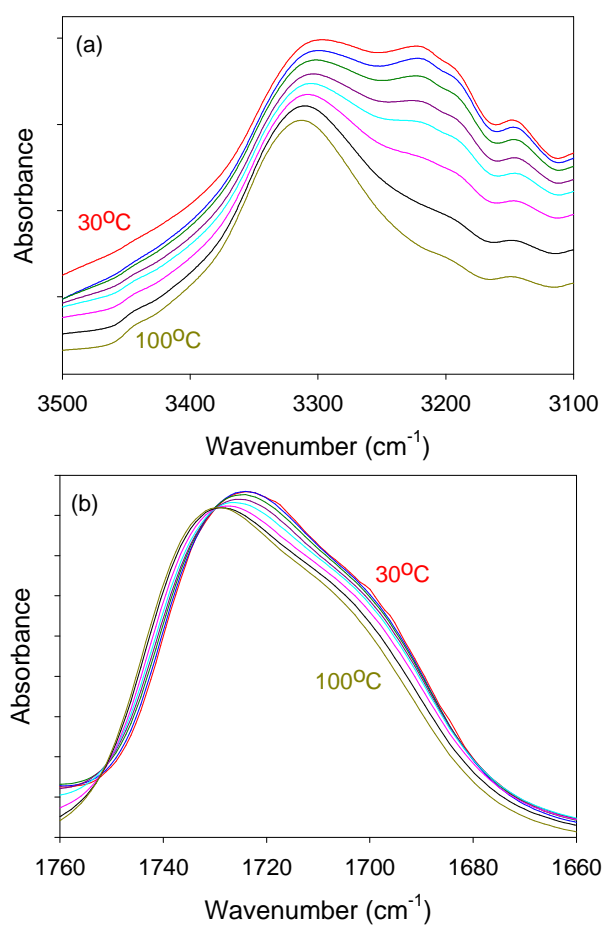


Figure 3-11: FTIR spectra of neutral sample from 30 to 100°C at (a) N-H region and (b) C=O region.

---

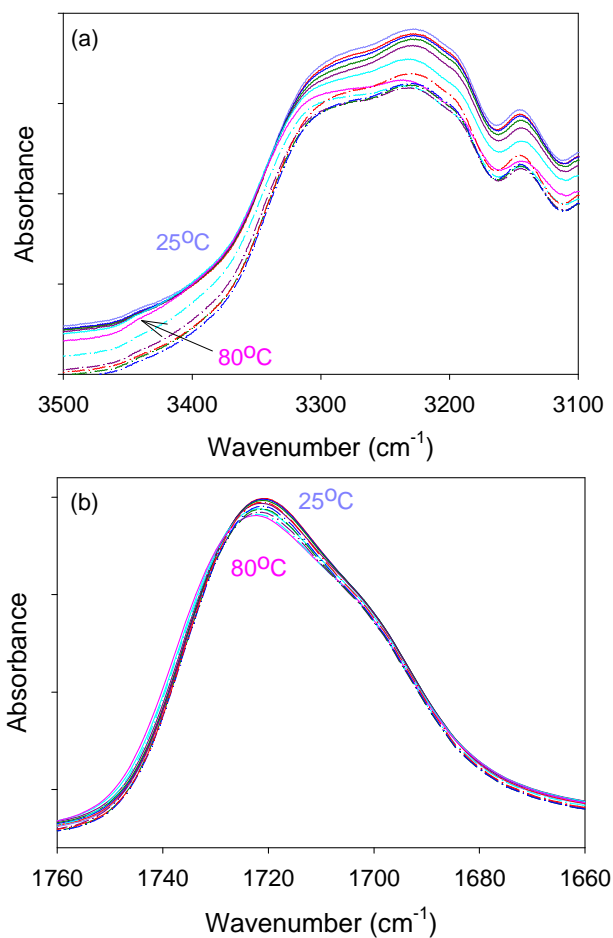


Figure 3-12: FTIR spectra of BuMeIm<sup>+</sup> sample from 25 to 100°C at (a) N-H region and (b) C=O region. Solid line: during heating process; dash-dot line: during cooling process.

### 3.4 Summary and Future Work

Throughout this chapter, the morphology and hydrogen bonding of urethane and ether groups were investigated by X-ray scattering and FTIR. X-ray scattering showed no evidence of microphase separation which agrees with our previous DRS and rheology study. FTIR spectra also suggested similar morphology. First, no ordered hydrogen

bonded C=O was observed. Second, there are many N-H groups hydrogen bonded to ether groups, indicating good phase mixing. Third, many urethane C=O are shown to be free, again suggesting a small extent of microphase separation. It can also be seen that free C=O decreases with the presence of counterions, as expected. For more quantitative comparison of the amount of hydrogen bonding, especially for the complicated N-H region including possibly more than 3 peaks corresponding to hydrogen bonds to different functional groups and counterions, curve resolving is very critical. Unfortunately, the data collected here do not have a good flat baseline that is vital for good curve resolving. A more smooth surface of the sample film on KBr is required for the flat baseline, which may be achieved by better sample preparation method or a better solvent for these ionomers. (Some experimental methods and discussions about hydrogen bonding in polyurethanes can also be found in Meredith Muskovich's senior thesis<sup>35</sup>.)

Temperature studies were also done by FTIR. As expected, hydrogen bonded N-H and C=O decrease with increasing temperature. When these samples are cooled down, hysteresis of the hydrogen bonded N-H and C=O peaks growth was observed, which is very likely because of the slow formation of hydrogen bonding in polyurethanes. It will be very interesting for future work to study the hysteresis through several heating-cooling cycles and the changes over a long period of time, i.e. in days or weeks.

### 3.5 Reference

1. Bonart, R.; Muller, E. H. *Journal of Macromolecular Science - Physics* **1974**, B10, (1), 177-189.
2. Bonart, R.; Muller, E. H. *Journal of Macromolecular Science - Physics* **1974**, B10, (2), 345-357.

3. Lee, D.-c.; Register, R. A.; Yang, C.-z.; Cooper, S. L. *Macromolecules* **1988**, 21, 1005-1008.
4. Polizos, G.; Georgoussis, G.; Kyritsis, A.; Shilov, V. V.; Shevchenko, V. V.; Gomza, Y. P.; Nesin, S. D.; Klimenko, N. S.; Wartewig, S.; Pissis, P. *Polymer International* **2000**, 49, 987-992.
5. Shilov, V. V.; Shevchenko, V. V.; Pissis, P.; Kyritsis, A.; Georgoussis, G.; Gomza, Y. P.; Nesin, S. D.; Klimenko, N. S. *Molecular Crystals and Liquid Crystals Science and Technology. A: Molecular Crystals and Liquid Crystals* **2001**, 361, 269-274.
6. Leung, L. M.; Koberstein, J. T. *Journal of Polymer Science: Polymer Physics Edition* **1985**, 23, 1883-1913.
7. Neumuller, W.; Bonart, R. *Journal of Macromolecular Science - Physics* **1982**, B21, (2), 203-217.
8. Choi, T.; Weksler, J.; Padsalgikar, A.; Runt, J. *Polymer* **2009**, 50, 2320-2327.
9. Elwell, M. J.; Ryan, A. J.; Brunbauer, H. J. M.; Lieshout, H. C. V. *Macromolecules* **1996**, 29, 2960-2968.
10. Yilgor, I.; Mather, B. D.; Unal, S.; Yilgor, E.; Long, T. E. *Polymer* **2004**, 45, (5829-5836).
11. Coleman, M. M.; Skrovanek, D. J.; Hu, J.; Painter, P. C. *Macromolecules* **1988**, 21, 59-65.
12. Wang, F. C.; Fève, M.; Lam, T. M.; Pascault, J.-P. *Journal of Polymer Science: Part B: Polymer Physics* **1994**, 32, 1305-1313.
13. Grasel, T. G.; Cooper, S. L. *Journal of Biomedical Materials Research* **1989**, 23, 311-338.
14. Goddard, R. J.; Cooper, S. L. *Macromolecules* **1995**, 28, 1401-1406.
15. Yang, J. E.; Kong, J. S.; Park, S. W.; Lee, D. J.; Kim, H. D. *Journal of Applied Polymer Science* **2002**, 86, (9), 2375-2383.
16. McGarthy, S. J.; Meijs, G. F.; Mitchell, N.; Gunatillake, P. A.; Heath, G.; Brandwood, A.; Schindhelm, K. *Biomaterials* **1997**, 18, 1387-1409.
17. Marchant, R. E.; Zhao, Q.; Anderson, J. M.; Hiltner, A. *Polymer* **1987**, 28, (12), 2032-2039.
18. Koberstein, J. T.; Gancarz, I. *Journal of Polymer Science: Part B: Polymer Physics* **1986**, 24, (11), 2487-2498.
19. Li, Y.; Gao, T.; Chu, B. *Macromolecules* **1992**, 25, 1737-1742.
20. Elwell, M. J.; Mortimer, S.; Ryan, A. J. *Macromolecules* **1994**, 27, 5428-5439.
21. Wang, W.; Liu, W.; Tudryn, G. J.; Colby, R. H.; Winey, K. I. *Macromolecules* **2010**, 43, 4223-4229.
22. Heiney, P. A. *Commission on Powder Diffraction Newsletter* **2005**, 32, 9-11.
23. Williams, S. R.; Wang, W.; Winey, K. I.; Long, T. E. *Macromolecules* **2008**, 41, 9072-9079.
24. Garrett, J. T.; Runt, J.; Lin, J. S. *Macromolecules* **2000**, 33, 6353-6359.
25. Chu, B.; Gao, T.; Li, Y.; Wang, J.; Desper, C. R.; Byrne, C. A. *Macromolecules* **1992**, 25, 5724-5729.
26. Velankar, S.; Cooper, S. L. *Macromolecules* **1998**, 31, 9181-9192.
27. Hummel, D. O.; Ellinghorst, G.; Khatchatryan, A.; Stenzenberger, H. D. *Angewandte Makromolekulare Chemie* **1979**, 82, (Nov), 129-148.

28. Yilgor, I.; Yilgor, E.; Guler, I. G.; Ward, T. C.; Wilkes, G. L. *Polymer* **2006**, 47, (11), 4105-4114.
29. Mondal, S.; Hu, J. L. *Journal of Membrane Science* **2006**, 274, 219-226.
30. Chen, L.; Yu, X.; Yang, C.-Z. *Chinese Journal of Polymer Science* **1996**, 14, (4), 295-303.
31. Teo, L.-S.; Chen, C.-Y.; Kuo, J.-F. *Macromolecules* **1997**, 30, 1793-1799.
32. Queiroz, D. P.; Pinho, M. N. d.; Dias, C. *Macromolecules* **2003**, 36, 4195-4200.
33. Wen, T. C.; Wang, Y.-J.; Cheng, T.-T.; Yang, C. H. *Polymer* **1999**, 40, 3979-3988.
34. Lu, M.; Runt, J.; Painter, P. *Macromolecules* **2009**, 42, 6581-6587.
35. Muskovich, M. Senior thesis, The Pennsylvania State University, State College, PA, 2010

## Chapter 4

### Structure-Property Relationship of Polyurethane Ionomers with Ions in the Soft Segment

#### 4.1 Introduction

Since first discovered to have outstanding cation solvation ability<sup>1</sup>, PEO-based ion conducting materials have been widely synthesized and tested and the mechanism of ion transport in PEO-based materials was also investigated<sup>2-4</sup>. The majority of these PEO-based ion conductors are PEO with dissolved salt which have potential issues like: (1) ionic conductivity contributed more by anions because anions move faster than small cations in the PEO matrix and (2) anions can undergo electrochemical reaction through charge-recharge cycles which cause hazardous problems and short lifetime<sup>5</sup>. For better applications  $\text{Li}^+$  or  $\text{Na}^+$  are often the ions of operation, but the faster anions polarize at one electrode first. These polarized anions store charge like a capacitor but (3) lower the field the cations see and (4) build up at the electrode/electrolyte interface, causing debonding that shortens cycle lifetime. To avoid these problems, single-ion conductors with anionic groups attached to the polymer chain present very good potential.<sup>5</sup> On the other hand, PEO has low  $T_g$ , which is an advantage for ion conduction, since ion transport in a PEO matrix is strongly coupled to PEO relaxation<sup>6, 7</sup>, but at the same time low  $T_g$  means low mechanical strength<sup>8</sup>. This issue may be overcome either by crosslinking polymers (chemically<sup>9</sup> or physically by semicrystalline PEO) or using block copolymers which contain both high  $T_g$  (mechanically strong) and low  $T_g$  (good

conductivity) phases<sup>10, 11</sup>. Here, we choose polyurethane based single-ion conductor as our candidate for its relatively simple and inexpensive chemistry compared to block copolymers. Polyurethanes physically crosslink by hydrogen bonding between urethane linkages and naturally microphase separated into hard (high  $T_g$ ) and soft (low  $T_g$ ) phases, whose size can be controlled by the monomers used.

Strategies to prepare polyurethane ionomers can be categorized by where and how the ionic groups are attached. A. Modifying the urethane linkage with an ionic group. This can be done by replacing urethane protons with propanesultone or propiolactone after a neutral polyurethane was synthesized. Note that this method removes partial or all urethane protons and impact the ability of microphase separation of hard and soft segment significantly.<sup>12-17</sup> B. Attaching ionic group in the hard segment by using a ion containing chain extender (short ionic diol) such as 2,2-dimethylolpropionic acid (DMPA).<sup>18-29</sup> This may be the easiest method to cooperate ions into polyurethanes since there are some commercial available ones that require no pre- or post- synthesis. C. Attaching ionic group in the soft segment by preparing ion containing polyols (long ionic diol).<sup>15, 30-37</sup> and (3) replacing urethane proton<sup>38</sup>. Since the urethane proton is critical for microphase separation and we already proved that placing ions in the hard segment also prevents microphase separation in Chapter 1, ion in soft segment polyurethane ionomers have been synthesized and are discussed in this chapter.

## 4.2 Materials and Experiment methods

### 4.2.1 Materials

Para-phenylene diisocyanate (pPDI), dimethyl fumarate, sodium bisulfite, tetraethylene glycol (PEG200,  $M_n = 194$ ), and dibutyltin oxide were purchased from Sigma-Aldrich. Polyethylene glycol (PEG,  $M_n = 400$  and  $600$  with  $M_w/M_n < 1.2$ ) was purchased from TCI America, Inc. Anhydrous, N,N-dimethylformamide (DMF), tetrahydrofuran (THF), toluene, and diethyl ether were purchased from EMD. All reagents were used as received without further purification, except pPDI which was purified by sublimation at  $80^\circ\text{C}$  overnight as described in the literature<sup>39</sup> and PEG600 which was dried under vacuum at  $80^\circ\text{C}$  for at least 24 hours to remove water (with less than 100ppm by Karl-Fischer titration).

### 4.2.2 Polyurethane (PU) ionomer synthesis

**Synthesis of sulfonated dimethyl fumarate.** Dimethyl fumarate (10 molar % excess) and sodium bisulfite were dissolved in methanol and distilled water respectively and then mixed in a round bottom flask and stirred at  $80^\circ\text{C}$  overnight<sup>34</sup>. The solution was concentrated by rotary evaporation and the product was crystallized in an excess of acetone at  $4^\circ\text{C}$ . Crystallized product was washed with acetone and dried at  $80^\circ\text{C}$  under vacuum. The chemical structure was confirmed by  $^1\text{H-NMR}$  in DMSO- $d_6$ .  $^1\text{H-NMR}$  (Figure A-1) and  $^{13}\text{C-NMR}$  (Figure A-2) are shown in the Appendix.

**Synthesis of sulfonate-centered diol (SC-diol).** Sulfonated dimethyl fumarate and PEG ( $M_w = 194, 400$  or  $600$ ) with a molar ratio of 1:4 and 0.5wt% dibutyltin oxide were charged into a three-neck round bottom flask and oxygen was removed by 30 minutes of vacuum before the reaction. The reaction was carried out at  $160^\circ\text{C}$  for at least 18 hours with argon purge to remove methanol. Completion of the reaction was monitored by disappearance of  $^{13}\text{C}$ -NMR peak of the methyl group in dimethyl fumarate at 53ppm. The product was dissolved in acetone and precipitated in toluene five times and the chemical structure was confirmed by  $^1\text{H}$ - and  $^{13}\text{C}$ -NMR (shown in Appendix, Figure A-3 and A-4). The chemical structure is shown in Figure 4-1.

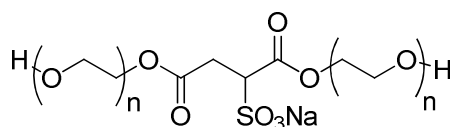


Figure 4-1: Chemical structure of SC-diols. In this chapter,  $n$  is 4, 9 or 13 with  $M_n = 248, 984$  or  $1384$ .

---

**Synthesis of PU ionomers with SC-diol.** The prepared SC-diol was dried at  $80^\circ\text{C}$  under vacuum overnight before use. Dried SC-diol, pPDI and PEG (with  $-\text{NCO} : -\text{OH} = 1:1$ ) were dissolved in anhydrous DMF, and then reacted at  $60^\circ\text{C}$  for 5-6 hours until the  $-\text{NCO}$  absorption peak at  $\sim 2270\text{ cm}^{-1}$  disappeared. Products were precipitated with excess diethyl ether and dialyzed using a dialysis cassette with 3500 molar mass cutoff in de-ionized water for a week to remove extra ions and low molecular weight polymer. The chemical structure is shown in Figure 4-2.

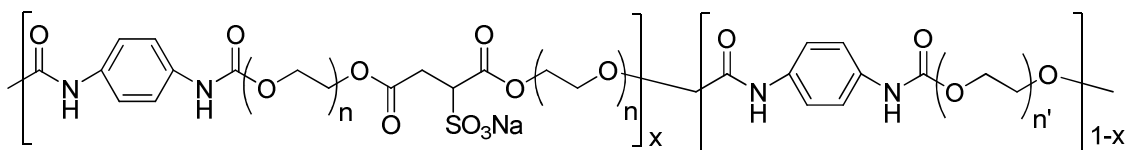


Figure 4-2: Chemical structure of SC-diol based polyurethane ionomers.

### 4.2.3 Experiment methods

**Differential scanning calorimetry (DSC).** The calorimetric glass transition temperature  $T_g$  was measured using a Seiko Instruments SSC/5200. All samples were dried under vacuum at 120°C for 2 days before measurement. All samples were first heated to 120°C and annealed for 3 minutes and then cooled down to -80°C at 10 K/min.  $T_g$  was determined from the change in heat capacity during the second heating at a heating rate of 10 K/min under an ultrahigh purity nitrogen purge.

**Thermogravimetric analysis (TGA).** The thermal degradation was probed by a TA Instruments Q50. All samples were dried under vacuum at 120°C for 2 days before measurement. All samples were heated to 800°C at a heating rate of 10 K/min with 20 ml/min nitrogen purge and the degradation temperature  $T_d$  was determined by the onset of degradation (intercept of stable and degradation curves).

**Dielectric relaxation spectroscopy (DRS).** All samples were dried at 120°C under vacuum for 1 day to remove moisture and then sandwiched between two freshly polished brass electrodes with 100  $\mu\text{m}$  Teflon spacers. The prepared cells were annealed in the vacuum oven for an additional 24 hours at 120°C before measurement. Dielectric (impedance) spectra were measured using a Novocontrol GmbH Concept 40 broadband

dielectric spectrometer in the frequency range of  $1 \times 10^{-2}$  to  $1 \times 10^7$  Hz with 0.1V amplitude. Samples were annealed at 150°C (all PU samples) or 120°C (SC-diols) for 30 min in the equipment and allowed to reach equilibrium with temperature for 5 min before each isothermal measurement.

**Linear viscoelasticity (LVE).** All samples were annealed at 120°C under vacuum for 2 days before measurement. Note that since all samples discussed here do not microphase separate and have  $T_g$  lower than 120 °C, they are annealed at their melt state. Linear viscoelastic response was probed in oscillatory shear using a Rheometrics RDS-II. All samples were annealed at the highest temperature studied (180°C for solid samples and 80°C for liquid samples), between two parallel plates (8 mm plates were used for solid samples and 25mm plates were used for liquid samples) for 30min in the equipment before measurement. All samples were allowed to equilibrate for 25min before each isothermal measurement. The temperature step data were collected every 1°C from room temperature at 1 rad/s with a 60 s equilibration time. The film thickness was double confirmed before and after DRS measurement.

**Small angle X-ray scattering (SAXS).** Samples were prepared by the same methods as described in the rheology section. Sample thickness (~0.1 mm) and Kapton or empty backgrounds were also recorded for data reduction. The data were collected on a Molecular Metrology SAXS instrument using a  $\text{CuK}\alpha$  radiation ( $\lambda = 1.542\text{\AA}$ ) and a two-dimensional multi-wire detector. The sample to detector distance is 150cm. At least 1,000,000 counts were collected for good quality of data (with transmission above 70%), which takes about 4 to 6 hours.

## 4.3 Results and Discussion

### 4.3.1 Chemical structure and thermal properties

Table 4-1 summarizes basic physical and thermal properties of PU ionomers studied in this chapter. SC-diolXXX indicates SC-diol made from PEG with molecular weight of XXX. PU indicates all the polyurethane samples, “s” indicates the use of SC-diol as soft segment and the number before “s” indicates  $M_n$  of PEG used in SC-diols. “d” and the number after are  $M_n$  of PEG diol used as a second soft segment component to dilute total ion content.

Table 4-1: Basic physical properties of sulfonate-center diols and PU ionomers studied in this chapter.

Sample	$n^1$	$n'^1$	$x^1$	Ion content $\rho_{\text{tot}} (1/\text{cm}^3)^2$	$\text{Na}^+/\text{EO}$	Hard segment (wt%)	$T_g (\text{°C})^3$	$T_d (\text{°C})^4$
SC-diol200	4	--	--	$1.3 \times 10^{21}$	0.13	--	21	228
SC-diol400	9	--	--	$7.7 \times 10^{20}$	0.056	--	-16	225
SC-diol600	13	--	--	$5.5 \times 10^{20}$	0.037	--	-30 <sup>6</sup>	237
PUd400	--	9	0	0	0	29	-1	
PU200s	4	--	1	$1.0 \times 10^{21}$	0.13	39	82	259
PU200sd400 <sup>5</sup>	4	9	0.58	$6.6 \times 10^{20}$	0.067	34	53	253
PU400s <sup>5</sup>	9	--	1	$6.6 \times 10^{20}$	0.056	14	22	263
PU600s	13	--	1	$4.9 \times 10^{20}$	0.037	10	-5	247
PU600sd600	13	13	0.17	$1.3 \times 10^{20}$	0.011	22	-16	

<sup>1</sup> $n$ ,  $n'$  and  $x$  are number of repeating units in Figure 4-1 and Figure 4-2.

<sup>2</sup>Assuming all samples have the same density of  $1 \text{ g/cm}^3$ .

<sup>3</sup>DSC  $T_g$ ; only one  $T_g$  is seen in DSC for all samples.

<sup>4</sup>Onset of thermal degradation from TGA.

<sup>5</sup>PU200sd400 and PU400s are designed to have the same total ion content.

<sup>6</sup>SC-diol600 also shows a small melting peak at  $15^\circ\text{C}$ .

Only one  $T_g$  was observed from DSC for all samples, regardless of ion content and hard segment content. No evidence of microphase separation from other characterization methods (discussed later) suggests single-phase morphology, even with more than 30wt% of hard segment. This is possibly caused by the PEO spacer between sulfonate groups and urethane linkage being too short, restricting formation of hard phase and raising  $T_g$ . It is worth to note that PU200sd400 and PU400s are designed to have the same ion content but result in very different  $T_g$ , implying  $T_g$  is not only controlled by ion content in these soft segment polyurethane. Figure 4-3 displays the relationship between  $T_g$  and  $\text{Na}^+/\text{EO}$  ratio which shows much better correlation than with ion content. PU samples show a stronger dependence on  $\text{Na}^+/\text{EO}$  ratio than SC-diols because hard segment content increases with increasing ion content in our design. This also explains why PUD400 has higher  $T_g$  than PU600s and PU600sd600, even with no ions. All ionomers have stronger  $T_g$  dependence on ion/EO ratio than salt dissolved in PEO systems<sup>40-42</sup> since anions attached on polymer chain in these ionomers.  $T_g$  of polyester ionomers with sulfonated isophthalate group attached between PEO spacers from the literature<sup>43</sup> are also compared in Figure 4-3. It is interesting that  $T_g$  in these polyester ionomers have similar dependence on  $\text{Na}^+/\text{EO}$  ratio with polyurethane samples, and a stronger dependence than SC-diols. Also, with small  $\text{Na}^+/\text{EO}$  ratio, the polyester ionomers from Dou et al<sup>43</sup> have lower  $T_g$  than the SC-diols. It may related to that there are more hydroxyl end groups in the SC-diols compared to polyester ionomers in Dou et al.

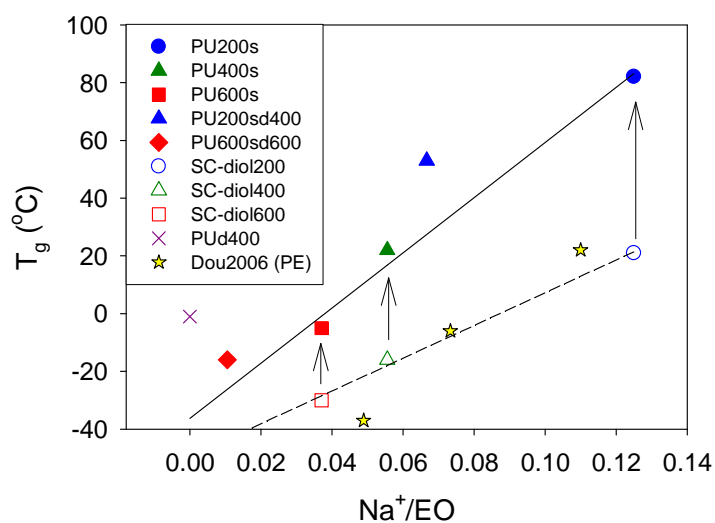


Figure 4-3: Relationship between DSC  $T_g$  and  $\text{Na}^+/\text{EO}$  ratio. Filled symbols: PU ionomers; open symbols: SC-diols. Blue symbols: made with SC-diol200; Green symbols: made with SC-diol400; red symbols: made with SC-diol600; yellow star: PEO-based polyesters with Na sulfonated isophthalates from Dou2006<sup>43</sup>. Dashed line is for the diols, solid line is for three polyurethanes with only SC-diols and the arrows connect the polyurethanes with the diol they are made from.

#### 4.3.2 Small angle X-ray scattering (SAXS) and morphology

As mentioned above, DSC suggests single-phase morphology. SAXS at room temperature was also done to further confirm the morphology. Figure 4-4 gives SAXS spectra of PU ionomer samples showing very little scattering and homogeneous morphology (or very low contrast between phases). Neither microphase separation nor ion aggregates were observed from SAXS.

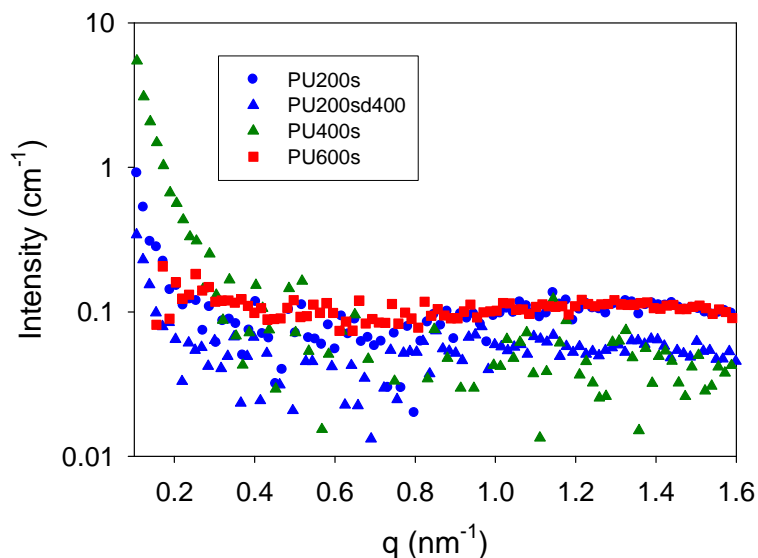


Figure 4-4: SAXS spectra of PU ionomers. Intensity was corrected for background and thickness.

### 4.3.3 Linear viscoelastic response

Linear viscoelastic response was probed by small amplitude oscillatory shear, which is also very useful for investigating local structure and relaxation.<sup>20, 44, 45</sup> The master curves of PU200s, PU400s and PU600s are presented in Figure 4-5, Figure 4-6 and Figure 4-7 respectively. These ionomers are weakly entangled. Time-temperature superposition (tTS) applies for both high and low frequency region but fails in transition region (90-110°C) for PU200s (Figure 4-5). tTS fails at 90-110°C is more likely because of local environment of ion-ion interaction or ion-urethane interaction and these interactions can change with temperature. In PU400s, tTS works better but still has a clear failure between 20 and 30°C due to the glass transition (DSC  $T_g = 22^\circ\text{C}$ ). The failure at 30-50°C is reminiscent of PU200s. The local minimum in  $\tan\delta$  in the rubbery

plateau is often where polymer blends exhibit tTS failure. tTS applies perfectly for PU600s, because the temperatures studied are much higher than  $T_g$ .  $G'$  is plotted against  $G''$  (Cole-Cole plot) in Figure 4-8. Although tTS fails in some parts, all of them show similar behavior in Cole-Cole plot suggesting very similar morphology in these ionomers. The slope in their terminal zone is much smaller than 2, consistent with the polydispersity expected for polycondensation polymers.<sup>46</sup>

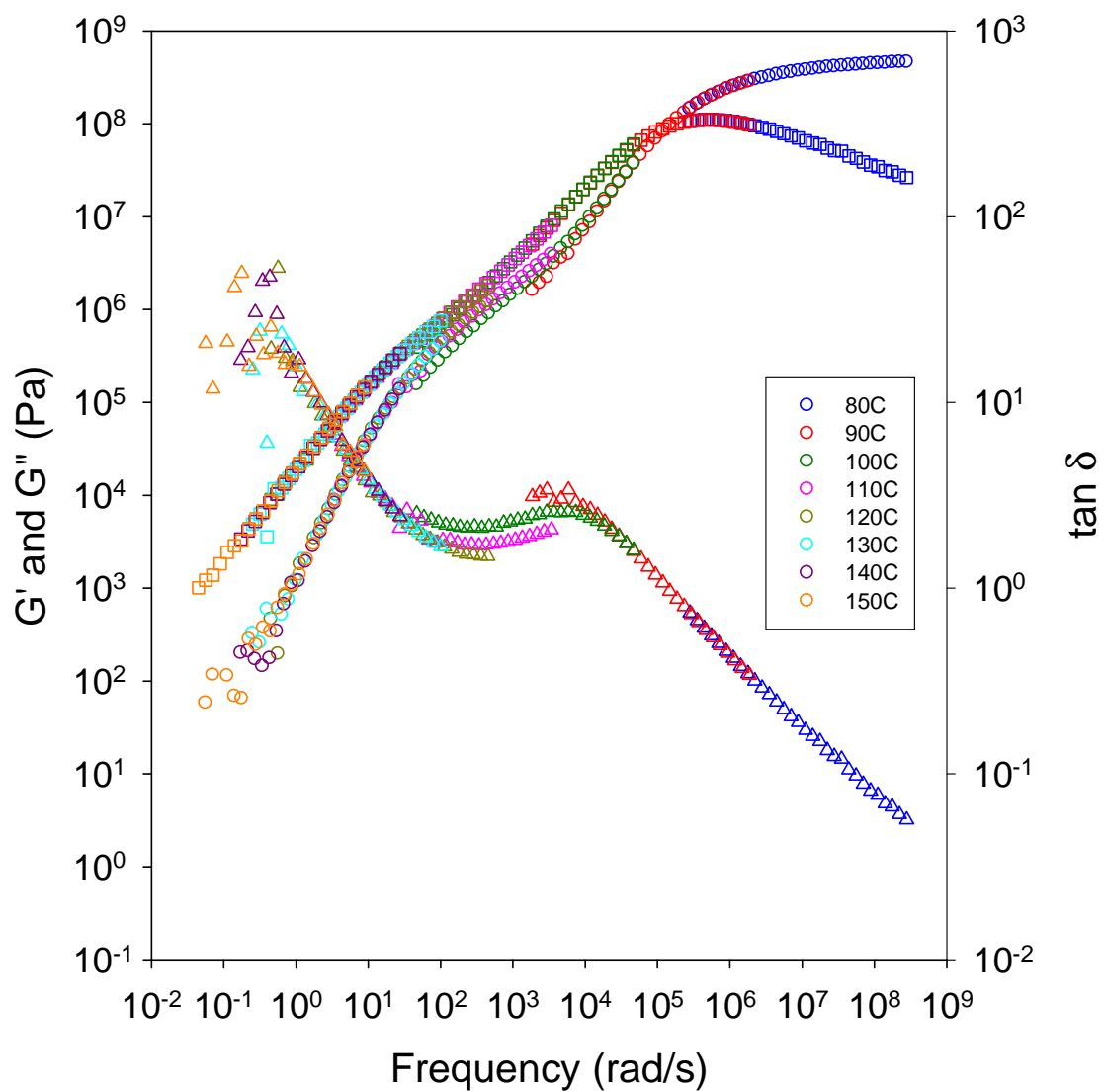


Figure 4-5: Master curve of PU200s with  $T_{\text{ref}} = 130^\circ\text{C}$  ( $T_g + 50^\circ\text{C}$ ). Circles:  $G'$ ; squares:  $G''$ ; triangles:  $\tan \delta$ .

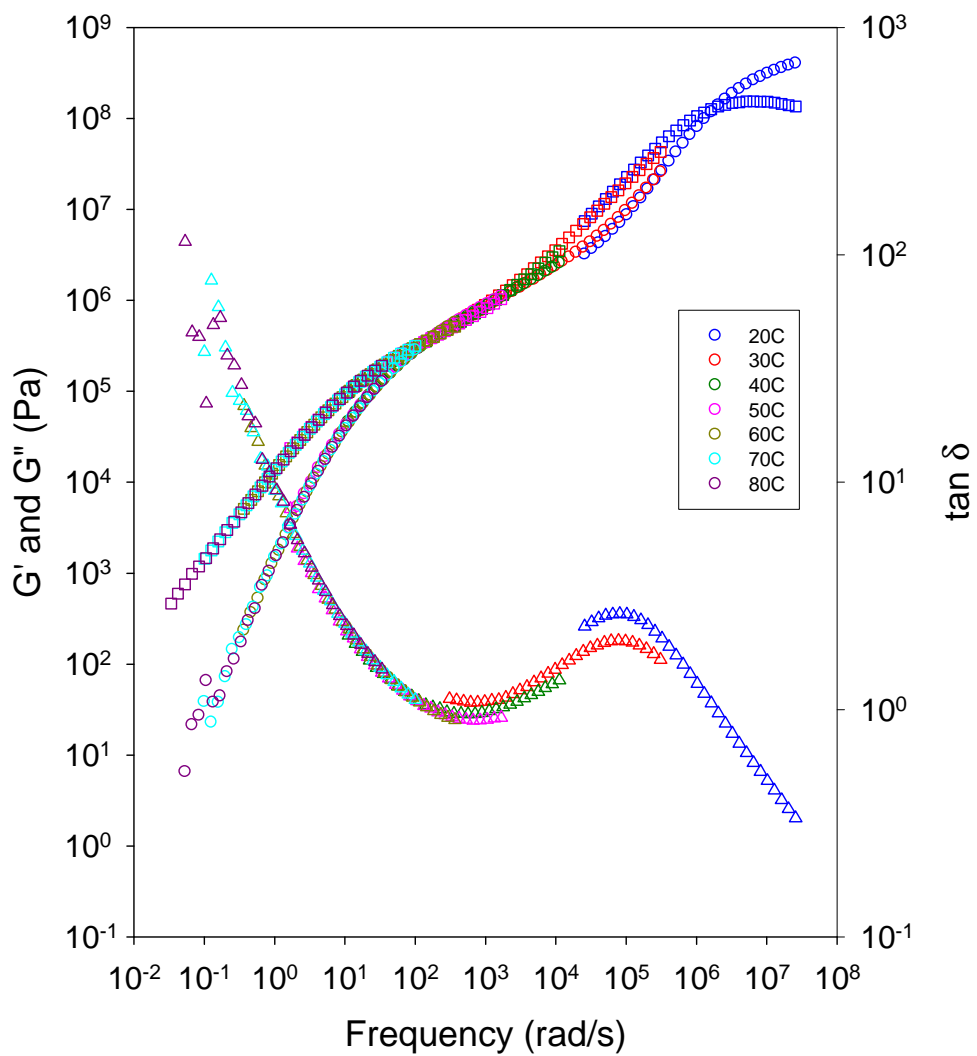


Figure 4-6: Master curve of PU400s with  $T_{ref} = 70^\circ\text{C}$  ( $T_g + 50^\circ\text{C}$ ). Circles:  $G'$ ; squares:  $G''$ ; triangles:  $\tan \delta$ .

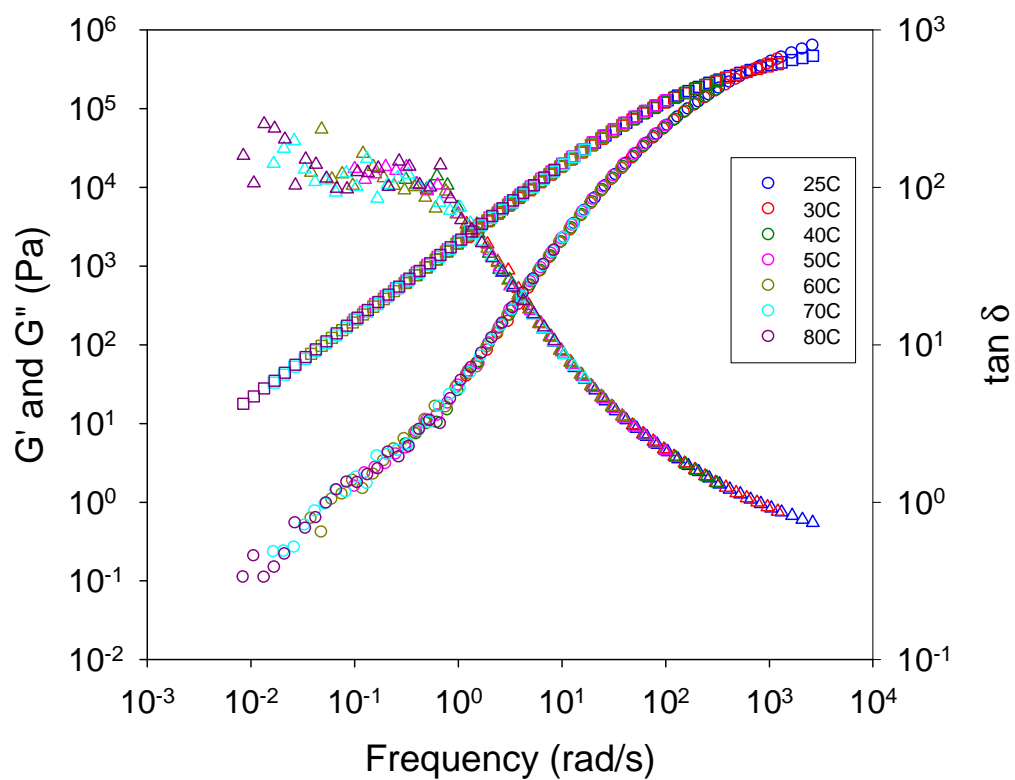


Figure 4-7: Master curve of PU600s with  $T_{\text{ref}} = 50\text{ }^{\circ}\text{C}$  ( $T_g + 50^{\circ}\text{C}$ ). Circles:  $G'$ ; squares:  $G''$ ; triangles:  $\tan \delta$ .

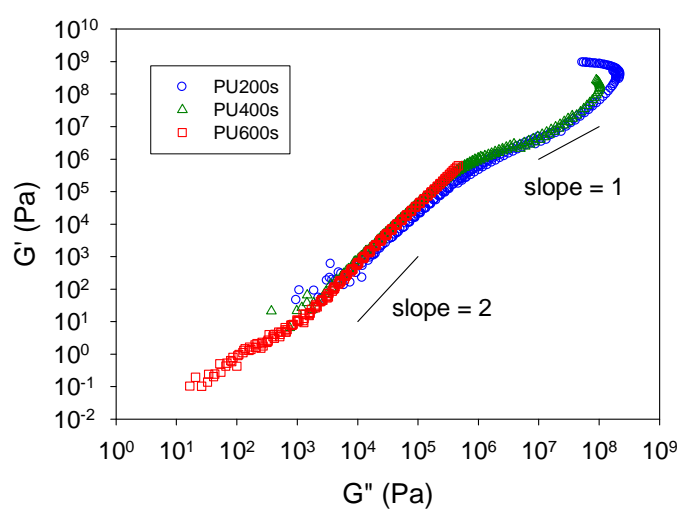


Figure 4-8: Cole-Cole plot of  $G'$  vs  $G''$  of PU ionomers.

Figure 4-9 displays the temperature step study of PU200s, PU400s and PU600s. A delayed relaxation can be seen in this temperature step study. PU200s has a  $\tan \delta$  peak at  $T_g + 10K$  with a small shoulder (black arrow in Figure 4-9), which is usually considered as the evidence of microphase separation in PUs<sup>47, 48</sup> or trapped ions as in Chapter 1<sup>20</sup>. tTS failure was also observed in a similar temperature range in Figure 4-5. Since no trapped ions were found through DRS analysis (discussed in next section) and SAXS suggests single-phase morphology, this is more likely due to a strong interaction between ions and the hard segment.

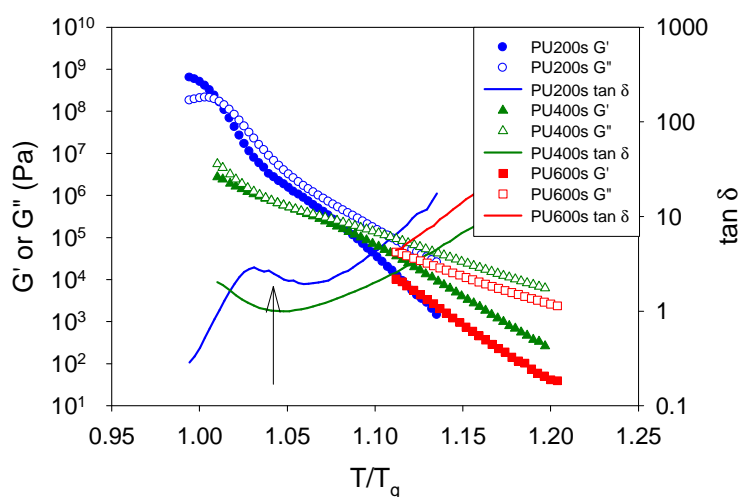


Figure 4-9: Temperature step study for PU200s, PU400s, and PU600s at 1 rad/s. Blue: PU200s; green: PU400s; red: PU600s; filled symbols:  $G'$ ; open symbols:  $G''$ ; solid lines:  $\tan \delta$ .

#### 4.3.4 Dielectric relaxation spectroscopy (DRS)

Besides investigating polymer dynamics by linear viscoelastic response, DRS also provides dynamics information by probing the dipole relaxations in polymers.<sup>49, 50</sup> Here,

DRS was used for probing both chain and ion relaxation. For ion conducting polymers, the  $\alpha$  relaxation peak in the loss spectra ( $\epsilon''$ ) associated with the segmental motion connected to the glass transition can be easily masked by dominating ion conduction. To reveal relaxations underneath ion conduction, a derivative spectrum (Eq. **4-1**) derived from the Kramers-Kronig relation was used<sup>50</sup>:

$$\epsilon_{der}(\omega) = -\frac{\pi}{2} \frac{\partial \epsilon'(\omega)}{\partial \ln \omega} \quad (\mathbf{4-1})$$

The derivative spectra of both PU ionomers and SC-diols are compared in Figure **4-10**.

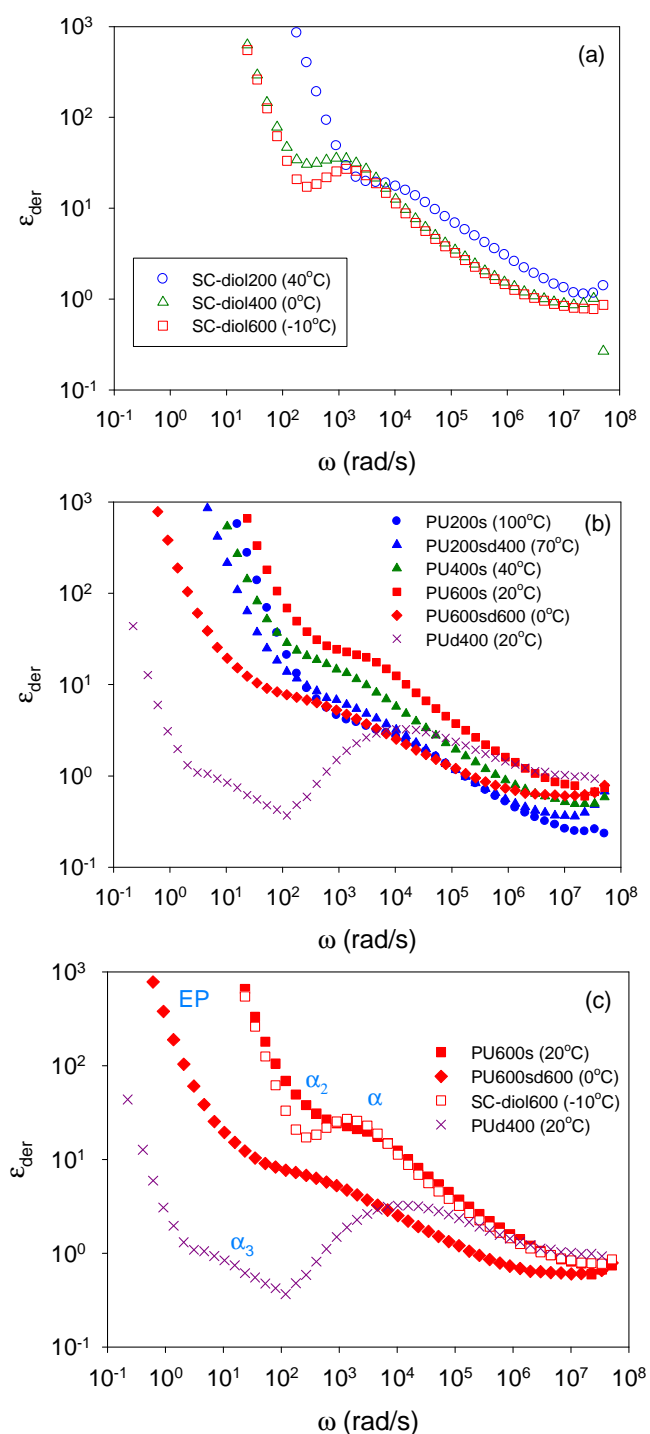


Figure 4-10: Derivative spectra of (a) SC-diols; (b) PUs; (c) SC-diol600 based ionomers and PUD400 at  $T_g + 20K$ . Fill symbols: PU ionomers; open symbols: SC-diols. Blue symbols: made with SC-diol200; Green symbols: made with SC-diol400; red symbols: made with SC-diol600.

Figure 4-10(a) shows the comparison of SC-diols with different PEO length. Only one relaxation (the  $\alpha$  relaxation) was observed in all three SC-diols. In Figure 4-10 (b), PUs with and without (PUd400) ions are compared. Unlike SC-diols, a second relaxation can be observed in all ion-containing PUs, right before electrode polarization (EP) starts. The same relaxation was not observed for the neutral PUd400, instead another much smaller relaxation appeared. Figure 4-10(c) further compares SC-diol600 based samples with neutral PUd400, with relaxations assigned. First, all samples show an  $\alpha$  relaxation of similar strength (Eq. 4-2 and Figure 4-11) that is larger than our previous study on polyester based ionomers<sup>42</sup> because of the presence of the very polar urethane group. It is interesting that SC-diols also have a larger  $\alpha$  relaxation even without urethane group. However, considering their much shorter chain, the  $\alpha$  relaxation of SC-diols may be related to relaxation of the whole chain, including the ions, instead of just PEO and that increases the dielectric strength since this now involves the much larger dipoles. This may as well explain why no  $\alpha_2$  relaxation was observed in our previous study<sup>42</sup>. Second, the  $\alpha_2$  relaxation only shows in ion containing PUs and in most samples, the  $\alpha_2$  relaxation is much larger than the  $\alpha$  relaxation.  $\alpha_2$  may be related to ions exchanging states.<sup>42</sup> Third, neutral PUd400 has another very small  $\alpha_3$  relaxation which cannot be observed in other ionomers. A similar relaxation was also seen in our polyester system but the origin of this relaxation is still not clear.<sup>42</sup> Fourth, EP (originating from ion accumulation) at low frequency can be observed in all samples including neutral PUd400. PUd400 has EP about 2 orders of magnitude smaller in amplitude than other ion-containing samples, for unknown reasons.

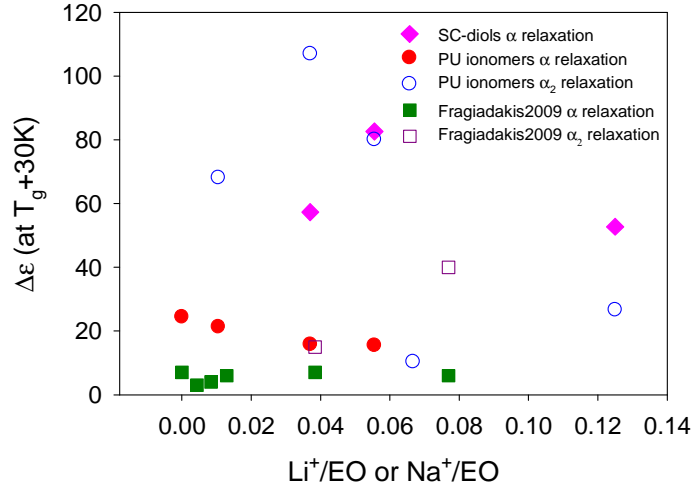


Figure 4-11: Relaxation strength  $\Delta\epsilon$  (Eq. 4-2) of  $\alpha$  and  $\alpha_2$  relaxation of polyurethane ionomers in this chapter and polyester sulfonate ionomers from ref <sup>42</sup> as a function cation/EO ratio.

The individual relaxations can be separated by fitting the spectra with the combination of power law (EP) and Havriliak-Nagami functions (Eq. 4-2) <sup>50</sup>:

$$\epsilon_{HN}^*(\omega) = \frac{\Delta\epsilon}{[1 + (i\omega\tau_{HN})^a]^b} \quad (4-2)$$

where  $\Delta\epsilon$  is the relaxation strength,  $a$  and  $b$  are shape parameters and  $\tau_{HN}$  is a characteristic relaxation time. The peak relaxation frequency of both  $\alpha$  and  $\alpha_2$  relaxations as functions of  $T_g/T$  are shown in Figure 4-12. The fact that Figure 4-12 does not collapse all curves suggests  $T_g$  is not directly related to chain relaxation. Both relaxations follow the Vogel-Fulcher-Tammann (VFT) equation:

$$\omega(T) = \omega_0 \exp\left(\frac{-DT_0}{T - T_0}\right) \quad (4-3)$$

where  $\omega_0$  is the unconstrained (high T) frequency,  $T_0$  is the Vogel temperature and D is a parameter inversely related to fragility. The fitting parameters are summarized in Table 4-2.

The  $\alpha$  relaxation has Vogel temperature  $T_0$  40-70K lower than the DSC  $T_g$ .  $T_g$  obtained by extrapolating the relaxation frequency to 0.01 rad/s can be as much as 28K lower than the DSC  $T_g$ , especially in samples with high ion and/or hard segment content. For the  $\alpha_2$  relaxation, the Vogel temperature  $T_0$  is 40-60K lower than the DSC  $T_g$  and  $T_g$  predicted from the VFT equation agrees with DSC  $T_g$  within 10K. Both relaxations can also be fitted with a common  $T_0 = 202\text{K}$ , which is the same as in our previous study on other PEO based ionomers<sup>20, 42</sup>. This collectively suggests that both relaxations are basically controlled by PEO relaxation. Similar mismatches were also observed in temperature step rheological study (Figure 4-9 and Chapter 2) where the  $\tan \delta$  peak, which always is above the DSC  $T_g$ , is further above  $T_g$  in samples with stronger or more Coulombic interaction and/or hydrogen bonds. In summary, the  $\alpha$  relaxation is more controlled by pure PEO relaxation while the DSC  $T_g$ ,  $\alpha_2$  and mechanical relaxation are controlled by slower (Coulombic interaction and hydrogen bonds) relaxations.

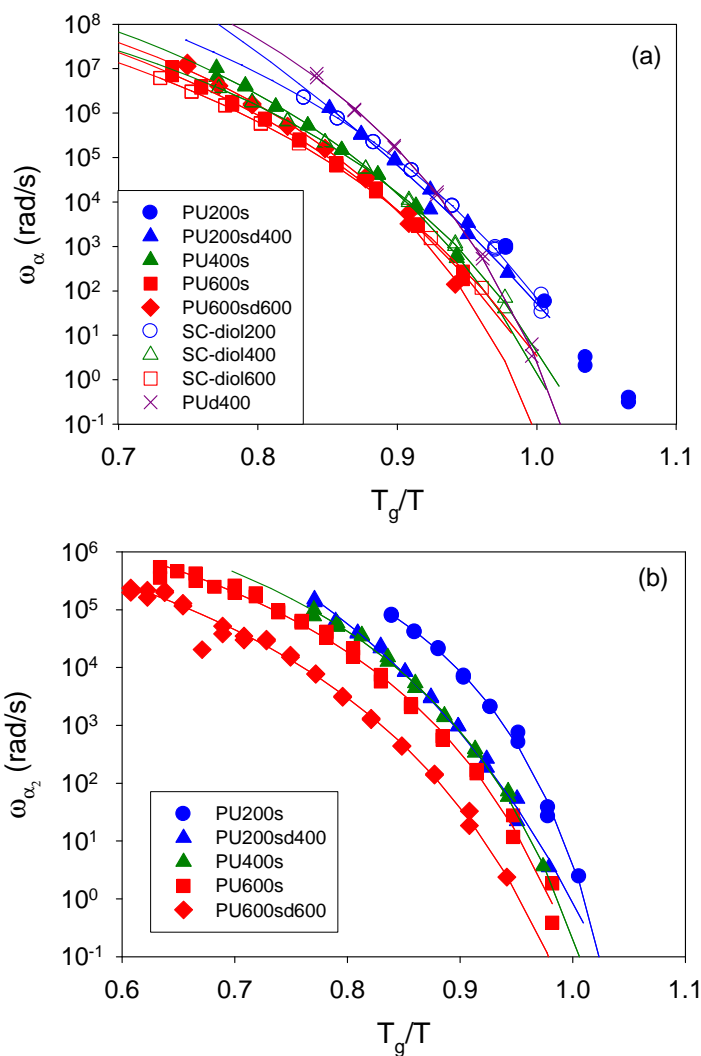


Figure 4-12: (a)  $\alpha$  and (b)  $\alpha_2$  relaxation frequency as function of  $T_g/T$ . Filled symbols: PU ionomers; open symbols: SC-diols. Blue symbols: made with SC-diol200; Green symbols: made with SC-diol400; red symbols: made with SC-diol600. Solid lines are best fits to the VFT equation (Eq. 4-3) with fitting parameters in Table 4-2.

Table 4-2: Fitting parameters for the temperature dependence of  $\alpha$ ,  $\alpha_2$ , and  $\alpha_3$  relaxation frequency.

Sample	$\omega_\alpha$			$\omega_{\alpha_2}$			$\omega_{\alpha_3}$		
	log $\omega_0$	$T_0$ (K)	D	log $\omega_0$	$T_0$ (K)	D	log $\omega_0$	$T_0$ (K)	D
SC-diol200	12	220	7.8						
SC-diol400	10.5	206	5.57						
SC-diol600	10.7	186	7.15						
PU200s*				7.89	308	2.56			
PU200sd400	10.5	240	5.57	8.65	263	4.94			
PU400s	11.4	237	6.38	7.98	248	3.74			
PU600s	11.1	209	7.16	7.69	224	3.88			
PU600sd600	10.8	217	5.1	7.51	210	4.94			
PUd400	12.8	224	6.13				9.45	191	10.6

\* $\alpha_2$  relaxation in PU200s is dominate and it is difficult to resolve  $\alpha$  relaxation and too few  $\alpha$  relaxation data points for good fitting.

Ionic conductivity (normalized by theoretical ion content) of PU ionomers as well as SC-diols is shown in Figure 4-13. As expected, samples with lower  $T_g$  show higher conductivity. Figure 4-13(b) is plotted against  $T_g/T$  to remove this effect and pretty well reduce the data within an order of magnitude band. Molar conductivity is also plotted against  $\alpha$  and  $\alpha_2$  relaxation in Figure 4-14. For a system with ion transport strongly coupled with polymer chain relaxation, which is common in PEO-based ion conductors<sup>7, 51</sup>, ionic conductivity can be described by fractal Debye-Stokes-Einstein (DSE) equation<sup>42, 52, 53</sup>:

$$\mu_{avg} = \frac{\sigma_{DC}}{ep_{tot}} = \frac{1}{e} \Lambda \sim \left( \frac{\omega_\alpha}{T} \right)^s \quad (4-4)$$

where  $\mu_{avg}$  is average cation mobility of all ions,  $e$  is the elementary charge,  $p_{tot}$  is theoretical ion content calculated from chemical structure and  $\Lambda$  is molar conductivity. Here, the change in  $T$  is ignored since it is much smaller compared to the change in  $\omega_\alpha$ .

Figure 4-14(a) is plotted against  $\omega_\alpha$  and the data naturally separate into two groups: PU200s and PU200sd400 group and all others. PU200s and PU200sd400 have a slope of 1 indicating ion transport is perfectly coupled with  $\alpha$  relaxation in these two ionomers while decoupling can be seen in the other samples, whose slope of 0.85 agrees with our previous PEO-based polyester ionomers study<sup>42</sup>.

Figure 4-14(b) shows the correlation between molar conductivity and  $\alpha_2$  relaxation. Unlike in Figure 4-14(a), all samples show a slope of 1 in this plot. This proves the idea that  $\alpha_2$  relaxation is related to ion association/relaxation. It is interesting that short SC-diols do not have this relaxation. Here I propose the origin of the difference as follows. In all samples ion interaction is the strongest and as a result it relaxes slowest like a temporary crosslink point. Consider the chemical structure of SC-diols, the ions (crosslink point) are located at the middle of the chain, which can slow down the chain relaxation but the whole chain is still short enough to relax with only one physical crosslink point in the middle of the chain within the same time distribution, so only one delayed  $\alpha$  relaxation is seen. When SC-diols are chemically bonded into PU ionomers, crosslink points on every single chain increase. So besides slowed down  $\alpha$  relaxation, another slower  $\alpha_2$  relaxation appears. This  $\alpha_2$  relaxation represents the time scale for a polymer chain to escape from these crosslink points and ions to exchange status. And depending on the strength of the interaction between the ions and polymer chains, different degree of decoupling can occur. It is interesting that molar conductivity at a given relaxation time decreases with increasing ion content (or  $\text{Na}^+/\text{EO}$  ratio) which is opposite to our previous study<sup>42</sup>. However, in this PU ionomer system, the urethane

linkage has strong interactions with ions<sup>20</sup>, PEO<sup>37</sup> and other urethane linkages. Since the amount of urethane linkage also changes with ion content, it is difficult to provide a simple explanation here.

Molar conductance and conductivity were also plotted against  $\Delta\varepsilon_{\alpha}\omega_{\alpha}$  and  $\Delta\varepsilon_{\alpha_2}\omega_{\alpha_2}$  in the inset in Figure 4-14 which show better correlation and collapse the data better than fractal DSE equation. Barton-Nakajima-Namikawa (BNN) relation<sup>54, 55</sup> predicts:  $\sigma_{DC} \sim \Delta\varepsilon\omega$  as shown in Figure 4-14 inset. It is very interesting that  $\Delta\varepsilon_{\alpha}\omega_{\alpha}$  shows good correlation with *molar conductivity* while  $\Delta\varepsilon_{\alpha_2}\omega_{\alpha_2}$  shows better correlation with *conductivity*. This may be related to that  $\alpha_2$  relaxation involves with ions so it has correlation with *total amount* of ions in the polymer while  $\alpha$  relaxation is purely polymer chain relaxation so it correlates better with how much ions transport *per chain*.

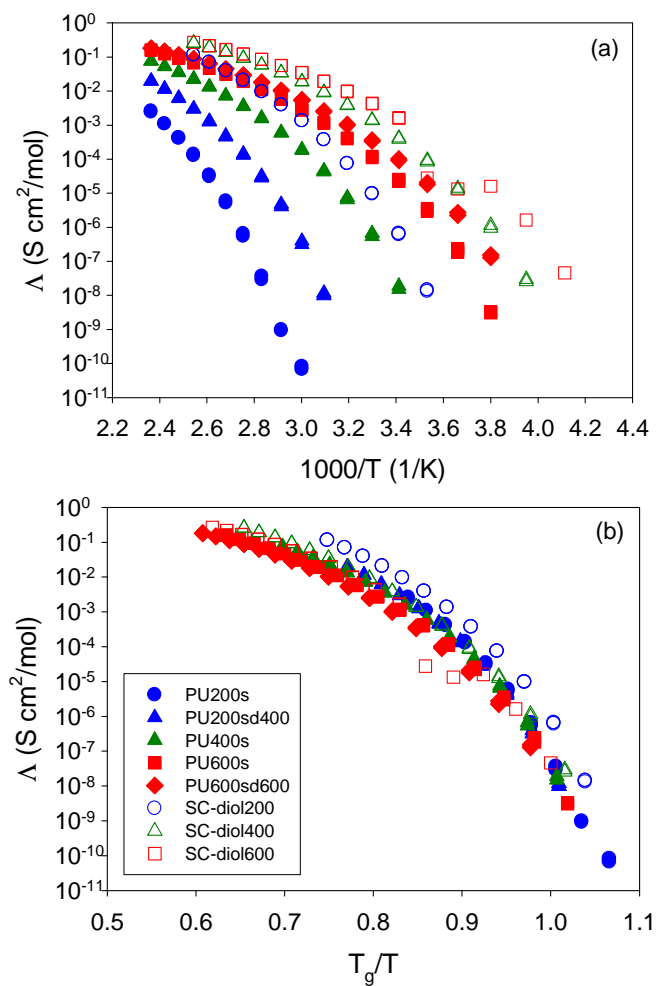


Figure 4-13: Molar ionic conductivity as function of (a)  $1000/T$  and (b)  $T_g/T$ . Fill symbols: PU ionomers; open symbols: SC-diols. Blue symbols: made with SC-diol200; Green symbols: made with SC-diol400; red symbols: made with SC-diol600.

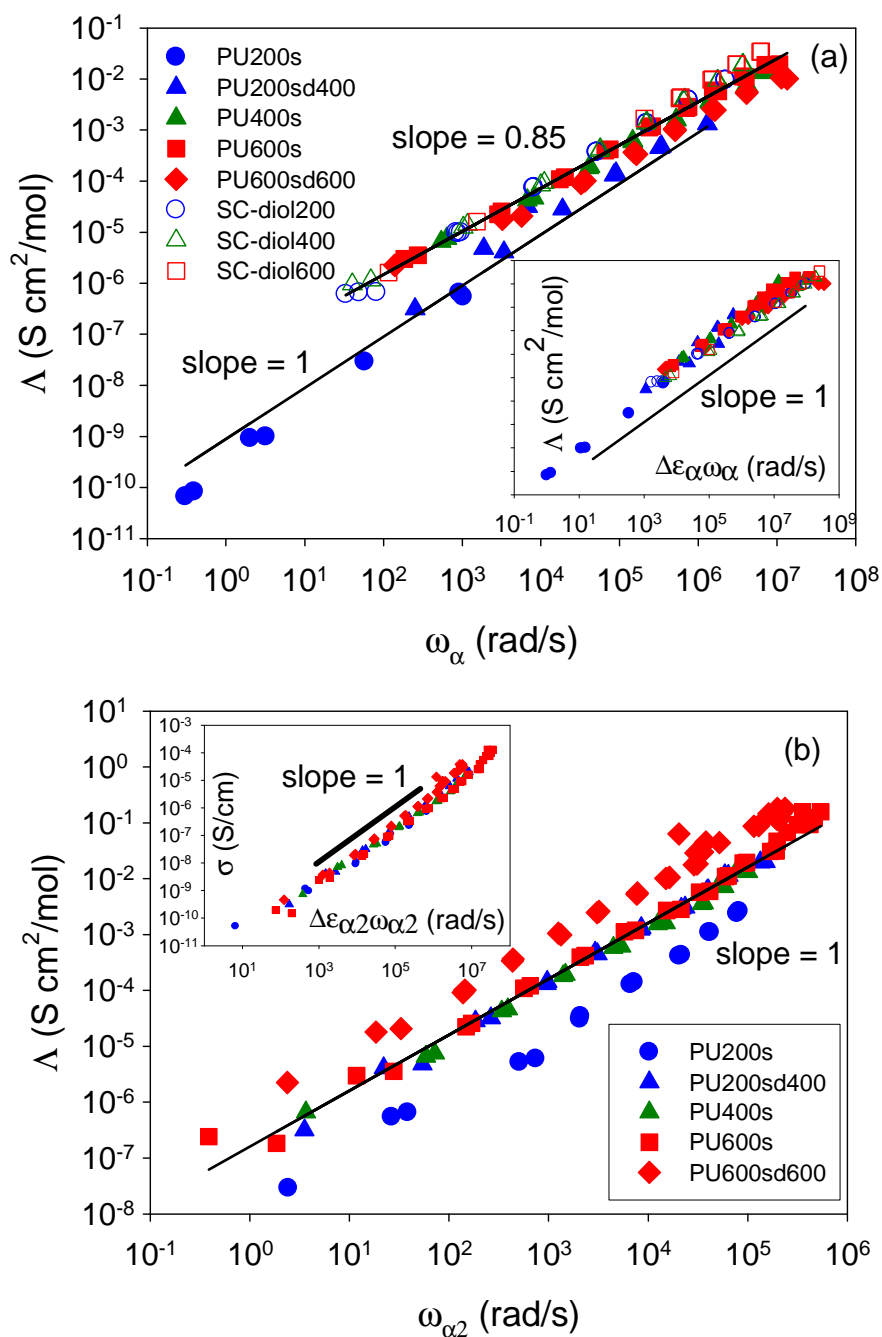


Figure 4-14: Molar ionic conductivity as function of (a)  $\alpha$  relaxation frequency and (b)  $\alpha_2$  relaxation frequency. Fill symbols: PU ionomers; open symbols: SC-diols. Blue symbols: made with SC-diol200; Green symbols: made with SC-diol400; red symbols: made with SC-siol600; solid lines: fit to fractal DSE equation (Eq. 4-4). Inset: BNN plot of *molar conductance* as a function of  $\Delta\epsilon_{\alpha}\omega_{\alpha}$  and *conductivity* as a function of  $\Delta\epsilon_{\alpha_2}\omega_{\alpha_2}$ .

To further investigate ion transport, an electrode polarization model (EP model, Macdonald/Coelho model)<sup>56-58</sup> was applied to separate conducting ion content and their mobility at any given instant in time. For a single-ion conductor with blocking electrodes under electric field, the conductivity and the polarization can be described as (Eq. 4-5, Eq. 4-6)

$$\sigma_{DC} = e\mu p \quad (4-5)$$

$$\tan \delta = \frac{\varepsilon''}{\varepsilon'} = \frac{\omega\tau_{EP}}{1 + \omega^2\tau_{\sigma}\tau_{EP}} \quad (4-6)$$

with  $\tau_{\sigma}$  and  $\tau_{EP}$  representing time scale of ion conduction and full electrode polarization (Eq. 4-7, Eq. 4-8)

$$\tau_{\sigma} \equiv \frac{\varepsilon_s \varepsilon_0}{\sigma_{DC}} \quad (4-7)$$

$$\tau_{EP} \equiv \frac{\varepsilon_{EP} \varepsilon_0}{\sigma_{DC}} \quad (4-8)$$

where  $\varepsilon_s$  is the static dielectric constant of polymer,  $\varepsilon_{EP}$  is the dielectric constant when EP is completed and  $\varepsilon_0$  is vacuum permittivity. At any given instant, conducting ion concentration and their mobility can be obtained, with L the sample film thickness (Eq. 4-9, Eq. 4-10)

$$p = \frac{4\sigma_{DC}\tau_{EP}^2 kT}{e^2 L^2 \tau_{\sigma}} \quad (4-9)$$

$$\mu = \frac{eL^2 \tau_{\sigma}}{4\tau_{EP}^2 kT} \quad (4-10)$$

Figure 4-15 gives the temperature dependence of conducting ion concentration. Since all samples have different ion content, Figure 4-15 is normalized by theoretical total ion content,  $p_{\text{tot}}$ . As expected, ionomers with smaller  $p_{\text{tot}}$  (or  $\text{Na}^+/\text{EO}$ ) have a larger portion of conducting ions.<sup>42</sup> The conducting ion concentration follows Arrhenius behavior:

$$p = p_0 \exp\left(\frac{-E_a}{kT}\right) \quad (4-11)$$

where  $E_a$  is the activation energy and  $p_0$  is the conducting ion content at infinite temperature.  $p_0$  also gives a hint as to how many ions are available to conduct under an electric field. The fitting parameters are summarized in Table 4-3. We can find that  $p_0$  in this ion-in-soft-segment system agrees with the theoretical ion content  $p_{\text{tot}}$  within an order of magnitude except PU600sd600. This implies that the problem of ions trapped in the hard segment in our previous ion-in-hard-segment system has been solved by placing ions in the soft segment. The usual high conducting ion content and low cation mobility (Figure 4-17) of PU600sd600 may be related to some other relaxation underneath EP (the  $\alpha_2$  relaxation of PU600sd600 in Figure 4-10(c) is more like neutral PUd400 than other ionomers). As expected, PU ionomers have a larger  $E_a$  owing to stronger interactions with ions. It may also be expected that samples with larger  $p_{\text{tot}}$  or  $\text{Na}^+/\text{EO}$  have larger activation energy like yellow stars in Figure 4-16. However, a minimum activation energy was found at  $\text{Na}^+/\text{EO} = 0.06$  corresponding to 9 EO unit per  $\text{Na}^+$  (shown in Figure 4-16) for both SC-diols and PU ionomers. Further study is suggested for understanding this phenomena.

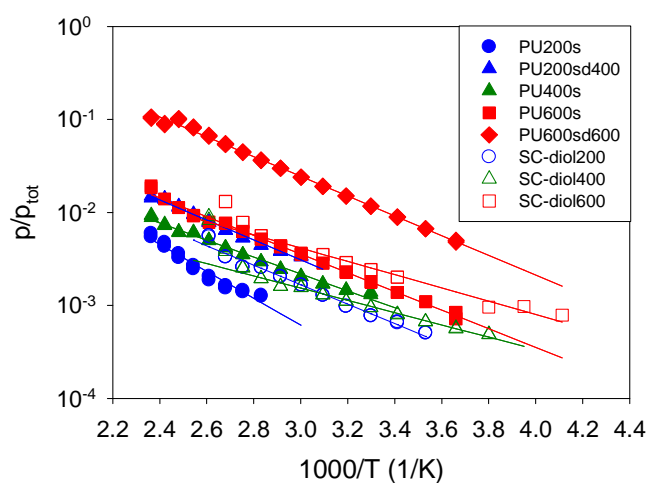


Figure 4-15: Temperature dependence of conducting ion concentration. Fill symbols: PU ionomers; open symbols: SC-diols. Blue symbols: made with SC-diol200; Green symbols: made with SC-diol400; red symbols: made with SC-diol600; solid line: fit to Eq. 4-11.

Table 4-3: Fitting parameters for temperature dependence of conducting ion concentration (Eq. 4-11) and their mobility (Eq. 4-12).

Sample	$\log p_{\text{tot}}$	Conducting ion concentration $p$		Cation mobility $\mu$		
		$\log p_0$	$E_a$ (kJ/mol)	$\log \mu_0$	$T_0$ (K)	$D$
SC-diol200	21.1	21.5	20.0	-1.41	242	3.15
SC-diol400	20.9	20.1	12.6	-1.12	211	3.71
SC-diol600	20.7	20.5	13.7	-1.92	206	3.08
PU200s	21.0	22.1	27.7	-2.58	308	2.36
PU200sd400	20.8	21.5	20.5	-2.63	283	2.60
PU400s	20.8	20.9	17.4	-2.30	255	2.60
PU600s	20.7	21.3	19.2	-2.54	229	2.70
PU600sd600	20.1	21.7	20.3	-3.59	226	2.24

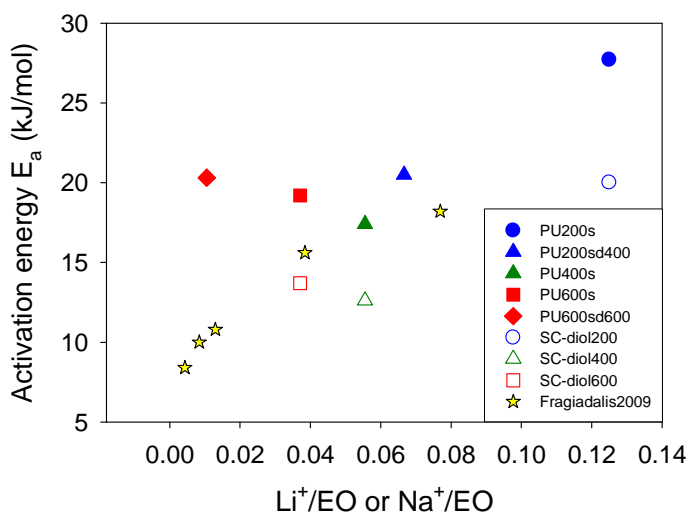


Figure 4-16: Relationship between activation energy and Na<sup>+</sup>/EO ratio. Fill symbols: PU ionomers; open symbols: SC-diols. Blue symbols: made with SC-diol200; Green symbols: made with SC-diol400; red symbols: made with SC-diol600; yellow star: data from ref<sup>42</sup> with Li<sup>+</sup>.

The temperature dependence of cation mobility is displayed in Figure 4-17(a). As expected, cation mobility follows the VFT equation:

$$\mu = \mu_0 \exp\left(\frac{-DT_0}{T - T_0}\right) \quad (4-12)$$

where  $\mu_0$  is the unconstrained (high T) cation mobility. Note that cation mobility cannot be fitted to a common  $T_0$ , like  $\omega_\alpha$  and  $\omega_{\alpha_2}$  were and has higher  $T_0$  than either  $\alpha$  or  $\alpha_2$  relaxations suggesting that it is controlled by a slower relaxation such as ion diassociation. On the other hand, plotting  $\mu$  against  $T_g/T$  does not reduce the data as well as for molar conductivity (i.e. average cation mobility, Figure 4-13), as we previously observed.<sup>20</sup> A simple interpretation is that all ions equally contribute to conductivity beyond  $\tau_\sigma$  and  $\omega_\alpha^{-1}$ , with the average mobility  $\mu_{\text{avg}}$  strongly correlated to  $T_g$  and polymer relaxations. The deviation we see here just reflects the fact that only a portion of cations

are conducting at any given instant in time and the cation mobility  $\mu$  of these conducting cations is faster with a stronger temperature dependence. The deviation and smaller slope in Figure 4-17(b) and (c) are also from the same reason, coupled to the fact that the number of conducting cations at any given instant increases with temperature.

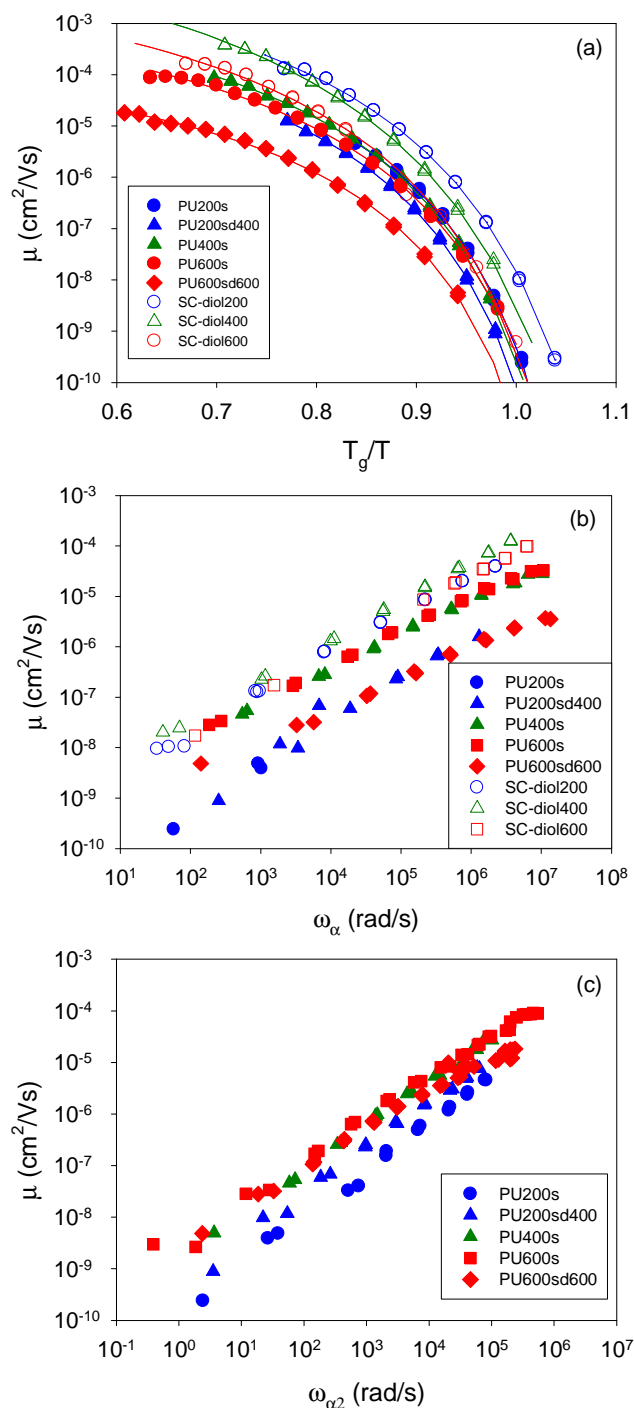


Figure 4-17: (a) Temperature, (b)  $\alpha$  relaxation and (c)  $\alpha_2$  relaxation frequency dependence of cation mobility. Filled symbols: PU ionomers; open symbols: SC-diols. Blue symbols: made with SC-diol200; Green symbols: made with SC-diol400; red symbols: made with SC-diol600; solid line: fit to Eq. 4-12.

#### 4.4 Conclusion

Sulfonate-centered PEO-based diols (SC-diols) with different PEO spacer lengths as well as PU ionomers based on these SC-diols were synthesized. As expected,  $T_g$  increases with shorter PEO spacer, increased ion density and increased hard segment content. SAXS suggests single-phase morphology although rheology suggests the existence of local ion-ion or ion-hard segment interaction. Polymer segmental relaxation plays a vital role. SC-diols have only one  $\alpha$  relaxation while PU ionomers have an extra, slower  $\alpha_2$  relaxation related to ion dissociation. It was again found that ionic conductivity is strongly related to polymer relaxation as a fractal DSE equation. Besides, BNN relation shows better ability to collapse data and may be the better way to explain the ion transport in ionomers. An EP model was applied to investigate conducting ion content and their mobility, which have Arrhenius and VFT temperature dependence, respectively.

Throughout this chapter, The data support that placing ionic groups in the middle of the soft segment diol effectively solved the ion trapping by the hard segment problem in the ion-in-hard-segment system discussed in Chapters 2 and 3. No discrete microphase separation was observed in this system even with high ion content in PU200s, possibly due to the very short PEO spacer. To further improve microphase separation and achieve our goal of coexistence of continuous hard phase with good mechanical strength and continuous soft phase with good flexibility and ionic conductivity, butane diol chain extenders will next be used to increase hard segment content without reducing PEO spacer length. Chain extended PU ionomers with SC-diol600 as the soft segment will be discussed in the next chapter.

#### 4.5 References

1. Fenton, D. E.; Parker, J. M.; Wright, P. V. *Polymer* **1973**, 14, 589.
2. Chandrasekhar, V. *Advances in Polymer Science* **1998**, 135, 139-205.
3. Ratner, M. A.; Johansson, P.; Shriver, D. F. *MRS Bulletin* **2000**, 25, (3), 31-37.
4. Quartarone, E.; Mustarelli, P.; Magistris, A. *Solid State Ionics* **1998**, 110, 1-14.
5. Wright, P. V. *MRS Bulletin* **2002**, 27, 597-602.
6. Ratner, M. A.; Shriver, D. F. *Chemical Reviews* **1988**, 88, 109-124.
7. Meyer, W. H. *Advanced Materials* **1998**, 10, (6), 439-448.
8. Snyder, J. F.; Carter, R. H.; Wetzel, E. D. *Chemistry of Materials* **2007**, 19, 3793-3801.
9. Song, J. Y.; Wang, Y. Y.; Wan, C. C. *Journal of Power Sources* **1999**, 77, 183-197.
10. Soo, P. P.; Huang, B.; Jang, Y.-I.; Chiang, Y.-M.; Sadoway, D. R.; Mayes, A. M. *Journal of The Electrochemical Society* **1999**, 146, (1), 32-37.
11. Gomez, E. D.; Panday, A.; Feng, E. H.; Chen, V.; Stone, G. M.; Minor, A. M.; Kisielowski, C.; Downing, K. H.; Borodin, O.; Smith, G. D.; Balsara, N. P. *Nano Letters* **2009**, 9, (3), 1212-1216.
12. Ding, Y. S.; Register, R. A.; Yang, C. Z.; Cooper, S. L. *Polymer* **1989**, 30, (7), 1213-1220.
13. Visser, S. A.; Cooper, S. L. *Macromolecules* **1991**, 24, 2576-2583.
14. Lee, D.-C.; Register, R. A.; Yang, C.-Z.; Cooper, S. L. *Macromolecules* **1988**, 21, 1005-1008.
15. Xu, H.-S.; Yang, C.-Z. *Journal of Polymer Science: Part B: Polymer Physics* **1995**, 33, 745-751.
16. Grasel, T. G.; Cooper, S. L. *Journal of Biomedical Materials Research* **1989**, 23, (3), 311-338.
17. Silver, J. H.; Marchant, J. W.; Cooper, S. L. *Journal of Biomedical Materials Research* **1993**, 27, (11), 1443-1457.
18. Yang, C.-Z.; Grasel, T. G.; Bell, J. L.; Register, R. A.; Cooper, S. L. *Journal of Polymer Science: part B: Polymer Physics* **1991**, 29, 581-588.
19. Wen, T.-C.; Wang, Y.-J.; Cheng, T.-T.; Yang, C.-H. *Polymer* **1999**, 40, 3979-3988.
20. Wang, S.-W.; Liu, W.; Colby, R. H. *Chemistry of Materials* **2011**, 23, 1862-1873.
21. Hwang, K. K. S.; Speckhard, T. A.; Cooper, S. L. *Journal of Macromolecular Science - Physics* **1984**, B23, 153-174.
22. Al-Salah, H. A.; Frisch, K. C.; Xiao, H. X.; Jr., J. A. M. *Journal of Polymer Science: part A: Polymer Chemistry* **1987**, 25, 2127-2137.
23. Lam, P. K. H.; George, M. H.; Barrie, J. A. *Polymer* **1989**, 30, (12), 2320-2323.
24. Kakati, D. K.; George, M. H. *Polymer* **1993**, 34, (20), 4319-4324.
25. Dieterich, D.; Keberle, W.; Witt, H. *Angewandte Chemie International Edition* **1970**, 9, (1), 40-50.
26. Chen, S.-A.; Chan, W.-C. *Journal of Polymer Science: Part B: Polymer Physics* **1990**, 28, (9), 1499-1514.
27. Goddard, R. J.; Cooper, S. L. *Macromolecules* **1995**, 28, 1401-1406.
28. Kim, B. K.; Lee, S. Y.; Lee, J. S.; Baek, S. H.; Choi, Y. J.; Lee, J. O.; Xu, M. *Polymer* **1998**, 39, (13), 2803-2808.

29. Ding, J.; Xue, G.; Yang, C.; Chen, R. *Journal of Applied Polymer Science* **1992**, *45*, 1087-1092.
30. Polizos, G.; Kyritsis, A.; Pissis, P.; Shilov, V. V.; Shevchenko, V. V. *Solid State Ionics* **2000**, *136*, 1139-1146.
31. Fragiadakis, D.; Dou, S.; Colby, R. H.; Runt, J. *Macromolecules* **2008**, *41*, 5723-5728.
32. Wei, X.; Yu, X. *Journal of Polymer Science: part B: Polymer Physics* **1997**, *35*, 225-232.
33. Shilov, V. V.; Shevchenko, V. V.; Pissis, P.; Kyritsis, A.; Georgoussis, G.; Gomza, Y. P.; Nesin, S. D.; Klimenko, N. S. *Journal of Non-Crystalline Solids* **2000**, *275*, 116-136.
34. Wang, X.; Li, H.; Tang, X.; Chang, F.-C. *Journal of Polymer Science Part B-Polymer Physics* **1999**, *37*, 837-845.
35. Bao, L.-H.; Lan, Y.-J.; Zhang, S.-F. *Journal of Polymer Research* **2006**, *13*, 507-514.
36. Wang, X. L.; Wang, L.; Li, H.; Tang, X. Z.; Chang, F. C. *Journal of Applied Polymer Science* **2000**, *77*, (1), 184-188.
37. Polizos, G.; Georgoussis, G.; Kyritsis, A.; Shilov, V. V.; Shevchenko, V. V.; Gomza, Y. P.; Nesin, S. D.; Klimenko, N. S.; Wartewig, S.; Pissis, P. *Polymer International* **2000**, *49*, 987-992.
38. Lee, D.-c.; Register, R. A.; Yang, C.-z.; Cooper, S. L. *Macromolecules* **1988**, *21*, 998-1004.
39. Sheth, J. P.; Klinedinst, D. B.; Wilkes, G. L.; Yilgor, I.; Yilgor, E. *Polymer* **2005**, *46*, 7317-7322.
40. Vachon, C.; Vasco, M.; Perrier, M.; Prud'homme, J. *Macromolecules* **1993**, *26*, 4023-4031.
41. Robitaille, C.; Marques, S.; Boils, D.; Prud'homme, J. *Macromolecules* **1987**, *20*, 3023-3034.
42. Fragiadakis, D.; Dou, S.; Colby, R. H.; Runt, J. *The Journal of Chemical Physics* **2009**, *130*, 064907.
43. Dou, S.; Zhang, S.; Klein, R. J.; Runt, J.; Colby, R. H. *Chemistry of Materials* **2006**, *18*, 4288-4295.
44. Colby, R. H.; Zheng, X.; Rafailovich, M. H.; Sokolov, J.; Peiffer, D. G.; Schwarz, S. A.; Strzhemechny, Y.; Nguyen, D. *Physical Review Letters* **1998**, *81*, (18), 3876-3879.
45. Tierney, N. K.; Register, R. A. *Macromolecules* **2003**, *36*, 1170-1177.
46. Han, C. D., Rheology of flexible homopolymers. In *Rheology and Processing of Polymeric Materials: Polymer Rheology*, Oxford University Press: New York, 2007; Vol. 1.
47. Velankar, S.; Cooper, S. L. *Macromolecules* **1998**, *31*, 9181-9192.
48. Velankar, S.; Cooper, S. L. *Macromolecules* **2000**, *33*, 395-403.
49. Kremer, F.; Schonhals, A., *Broadband Dielectric Spectroscopy*. Springer: 2003.
50. Wubbenhorst, M.; van Turnhout, J. *Journal of Non-Crystalline Solids* **2002**, *305*, (1-3), 40-49.
51. Borodin, O.; Smith, G. D. *Macromolecules* **2006**, *39*, 1620-1629.
52. Corezzi, S.; Campani, E.; Rolla, P. A.; Capaccioli, S. *Journal of Chemical Physics* **1999**, *11*, (20), 9343-9351.

53. Becker, S. R.; Poole, P. H.; Starr, F. W. *Physical Review Letters* **2006**, 97, (5), -.
54. Sangoro, J. R.; Serghei, A.; Naumov, S.; Galvosas, P.; Karger, J.; Wespe, C.; Bordusa, F.; Kremer, F. *Physical Review E* **2008**, 77, 051202.
55. Sidebottom, D. L. *Reviews of Modern Physics* **2009**, 81, (3), 999-1014.
56. Macdonald, J. R. *Physical Review* **1953**, 92, (1), 4-17.
57. Coelho, R. *Journal of Non-Crystalline Solids* **1991**, 131-133, 1136-1139.
58. Klein, R. J.; Zhang, S.; Dou, S.; Jones, B. H.; Colby, R. H.; Runt, J. *The Journal of Chemical Physics* **2006**, 124, 144903.

## Chapter 5

### Microphase Separation in Polyurethane Ionomers

#### 5.1 Introduction

Polyethylene glycol (PEG or PEO)-based polymer electrolytes, polyelectrolytes and single-ion conductors have drawn attention to many scientists and researchers since PEO was found to have excellent ability to solvate cations<sup>1-3</sup>. The flexible ether linkage and low  $T_g$  of PEO-based homopolymers facilitate ion transport and boost ionic conductivity, but at the same time sacrifice the mechanical strength<sup>4</sup>, which is very important for ion-conducting polymer applications including lithium ion battery membranes and ionic actuators.

In order to meet both requirements of ionic conductivity and mechanical strength, cross-linked PEO-based gel is a popular option, however, use of solvents to boost conductivity is inevitable.<sup>3, 5</sup> Besides polymer gels, materials with both hard phase (with good mechanical strength) and soft phase (fast relaxation and good conductivity) are also potential candidates. Instead of block copolymers<sup>6-8</sup>, we turn to PEO-based polyurethanes which also microphase separate into desired hard and soft phases. There are several ways to prepare polyurethane ionomers: (1) replacing the urethane proton by ion containing groups<sup>9, 10</sup>; (2) introducing the ionic group into the hard segment by ionic chain extender such as dimethylolpropionic acid (DMPA)<sup>11-14</sup>; and (3) attaching ionic groups in the soft segment by using oligomeric ion-containing diols<sup>15-17</sup>. Replacing the urethane proton

precludes microphase separation due to loss of the hydrogen bond donating –NH groups. And our previous study suggests that placing ionic groups in the hard segment increases ionic conductivity but reduces mechanical strength because ions in the hard segment compete for hydrogen bonds<sup>18</sup>. In this study, PEO-based sulfonate-containing diol was synthesized and used as soft segment. Butane diol was added as a chain extender to para-phenylene diisocyanate to investigate the required hard segment content for microphase separation and its effects on morphology, ionic conductivity, mechanical and dielectric properties.

## 5.2 Materials and Experimental Methods

### 5.2.1 Materials

Para-phenylene diisocyanate (pPDI), dimethyl fumarate, sodium bisulfite, 1,4-butanediol, terephthaloyl chloride, fumaryl chloride, potassium carbonate and dibutyltin oxide were purchased from Sigma-Aldrich. Polyethylene glycol (PEG,  $M_w = 600$  and  $M_w/M_n < 1.2$  from the manufacturer and confirmed by aqueous SEC and  $^1\text{H}$  NMR in DMSO- $d_6$ ) was purchased from TCI America, Inc. Anhydrous, N, N-dimethylformamide (DMF), dimethylsulfoxide (DMSO), tetrahydrofuran (THF), N-methyl-2pyrrolidone (NMP), toluene, methanol and diethyl ether were purchased from EMD. All reagents were used as received without further purification, except pPDI which was purified by sublimation at 80°C overnight as described in the literature<sup>19</sup> and PEG600 which was dried under vacuum at 80°C for at least 24 hours to remove water.

### 5.2.2 Synthesis of polyurethane and polyester ionomers

**Synthesis of sulfonated dimethyl fumarate.** Dimethyl fumarate (10 molar % excess) and sodium bisulfite were dissolved in methanol and distilled water respectively and then mixed in a round bottom flask at 80°C overnight<sup>20</sup>. The solution was concentrated by rotary evaporation and the product was crystallized with excess of acetone. Crystallized product was washed with acetone and dried at 80°C under vacuum. The chemical structure was confirmed by <sup>1</sup>H-NMR and <sup>13</sup>C-NMR in DMSO-d<sub>6</sub> (Appendix, Figure A-1 and A-2).

**Synthesis of sulfonate-centered diol (SC-diol).** Sulfonated dimethyl fumarate and PEG600 with a molar ratio of 1:4 and 0.5wt% dibutyltin oxide were charged into a three-neck round bottom flask and oxygen was removed by 30 minutes of vacuum before the reaction. The reaction was carried out at 160°C for at least 18 hours with argon purge to remove methanol. The product was precipitated from toluene five times and the chemical structure was confirmed by <sup>1</sup>H- and <sup>13</sup>C-NMR (Appendix Figure A-3 ~ 8).

**Synthesis of PU ionomers with SC-diol.** The prepared SC-diol was dried at 80°C under vacuum overnight before use. 1,4-Butanediol was dried with molecular sieves for a week (moisture content was below 100ppm by Karl Fischer titration). Dried SC-diol, 1,4-butanediol and pPDI (with -NCO : -OH = 1:1) were dissolved in anhydrous DMF, and then reacted at 60°C for 5-6 hours until the -NCO absorption peak at ~2270 cm<sup>-1</sup> disappeared. Products were precipitated with excess diethyl ether and dialyzed in de-ionized water for a week to remove extra ions and low molecular weight polymer. The chemical structure is shown in Figure 5-1 and confirmed by <sup>1</sup>H-NMR.

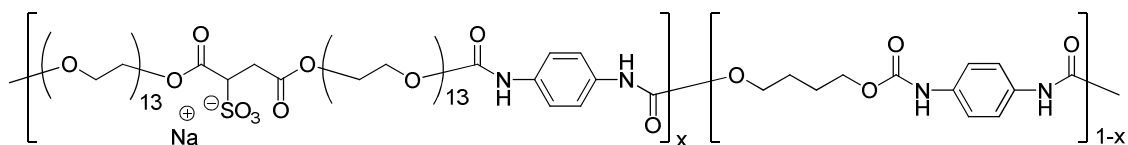


Figure 5-1: Chemical structure of SC-diol based PU ionomers. EO/Na<sup>+</sup> ratio is fixed at 26. SC-diol fraction  $x = 1, 0.5, 0.33, 0.25$ .

**Synthesis of polyester ionomer based on SC-diol.** Vacuum dried PEG600 dissolved in THF and potassium carbonate was charged into a three-neck flask and further dried by stirring with molecular sieves for 2 days. The solution was put into an ice bath before reaction. Fumaryl chloride THF solution was dropped into the dried solution above for 1 hour and the solution was stirred for another hour. Terephthaloyl chloride THF solution was then added dropwise for 1 hour. The solution (20wt% in THF) was allowed to warm up to room temperature and react overnight. THF was then removed by rotary evaporation to obtain crude product. The crude product was dissolved in methanol and mixed with sodium bisulfite (10% excess) aqueous solution and the solution was allowed to react at 80°C overnight. The final product was concentrated and dialyzed in de-ionized water for 2 weeks to remove extra sodium bisulfite, ions and low molecular weight polymer. The chemical structure is shown in Figure 5-2.

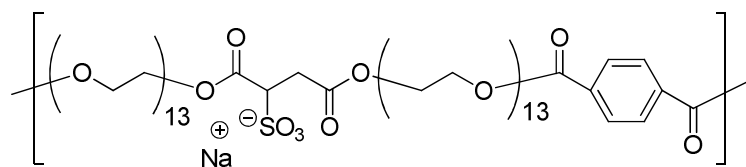


Figure 5-2: Chemical structure of SC-diol based polyester ionomer. EO/Na<sup>+</sup> ratio is 26.

### 5.2.3 Sample preparation and characterization

**Differential scanning calorimetry (DSC).** The calorimetric glass transition temperature  $T_g$  was measured using a Seiko Instruments SSC/5200. All samples were dried under vacuum at 120°C for 2 days before measurement. All samples were first heated to 120°C and annealed for 3 minutes and then cooled down to -80°C at 10 K/min.  $T_g$  was determined from the change in heat capacity during the second heating at a heating rate of 10 K/min under ultrahigh purity nitrogen purge.

**Thermogravimetric analysis (TGA).** The thermal degradation was probed by a TA Instruments Q50. All samples were dried under vacuum at 120°C for 2 days before measurement. All samples were heated to 800°C at a heating rate of 10 K/min with 20 ml/min nitrogen purge and the degradation temperature  $T_d$  was determined by the onset of degradation (intersect of stable and degradation curve).

**Dielectric relaxation spectroscopy (DRS).** Liquid samples were dried at 120°C under vacuum for 1 day to remove moisture and then sandwiched between two freshly polished brass electrodes with 100  $\mu\text{m}$  thick Teflon spacers. The prepared cells were annealed in the vacuum oven for an additional 24 hours at 120°C before measurement. For solid samples, sample films were prepared by either solution casting or hot pressing. Solution cast samples were prepared from 10wt% DMSO polymer solution (~100  $\mu\text{m}$  thick, NMP was used for PU40 since it doesn't dissolve in DMSO) and hot pressed samples were prepared at 160°C under a pressure of 34 MPa (~200-300  $\mu\text{m}$ ). All prepared sample films were sandwiched between two freshly polished brass electrodes without spacers and then dried and annealed in a vacuum oven at 120°C for 2 days.

Dielectric (impedance) spectra were measured using a Novocontrol GmbH Concept 40 broadband dielectric spectrometer in the frequency range of  $1 \times 10^{-2}$  to  $1 \times 10^7$  Hz with 0.1 V amplitude. Samples were annealed at 150°C for 30 min in the equipment and allowed to equilibrate for 5 min before each isothermal measurement.

**Linear viscoelasticity.** Solid samples were vacuum molded at 160°C for 20 min to prepare ~1mm thick, 7.9mm diameter pellets. All samples were annealed at 120°C under vacuum for 2 days before measurement. Linear viscoelastic response was measured in oscillatory shear using a Rheometrics Dynamic Spectrometer RDS-II with Bendix spring transducer. Solid samples were annealed at 180°C between two parallel plates for 30min with ~ 100g normal force to ensure good contact. All samples were allowed to equilibrate for 25min before each isothermal measurement. The temperature step data were collected every 1°C in heating from room temperature (after the isothermal frequency sweep study) at 1 rad/s with a 60 s equilibration time.

**Small angle X-ray scattering (SAXS).** Samples were prepared by the same methods as described in the DRS section. Sample thickness (~ 0.1-0.6mm) and Kapton® (2 sheets with 0.15mm total thickness) or empty background were also recorded for data reduction. The data were collected on a Molecular Metrology SAXS instrument using a CuK $\alpha$  radiation ( $\lambda = 1.542\text{\AA}$ ) and a two-dimensional multi-wire detector. The sample to detector distance is 150cm. At least 1,000,000 counts were collected for good quality of data, which takes about 4 to 6 hours.

## 5.3 Results and Discussions

### 5.3.1 Thermal analysis and basic physical properties

Table 5-1 summarizes the chemical composition of ionomers studied in this chapter as well as their basic physical properties.

Table 5-1: Chemical composition of SC-diol based PU and polyester ionomers and their physical properties.

Sample	$x^2$	HS content <sup>3</sup>	Physical state at room temperature	Ion content $p_{\text{tot}}$ ( $10^{20} \text{ cm}^{-3}$ )	$T_g^4$ ( $^{\circ}\text{C}$ )	$T_d^5$ ( $^{\circ}\text{C}$ )
SC-diol	-	-	Viscous liquid	5.5	-30	237
PE <sup>1</sup>	-	0wt%	Viscous liquid	5.0	-33	238
PU10 <sup>6</sup>	1	10wt%	Viscous liquid	4.9	-5	247
PU23	0.5	23wt%	Solid, $G' = 1 \text{ MPa}$	4.2	-1, 2	243
PU32	0.33	32wt%	Solid, $G' = 10 \text{ MPa}$	3.7	-2, 2	259
PU40	0.25	40wt%	Solid	3.3	1, 2	257

<sup>1</sup>Polyester version, see Figure 5-2.

<sup>2</sup> $x$  is the fraction of diols that are in SC-diol in Figure 5-1.

<sup>3</sup>Hard segment content = (diisocyanate + butanediol)/(diisocyanate + butanediol + SC-diol)

<sup>4</sup>Soft phase  $T_g$  measured by DSC. For solid samples, first shows the  $T_g$  of hot pressed films and then the solution cast (DMSO for PU23 and PU32, NMP for PU40) films.

<sup>5</sup>Onset of thermal degradation in TGA measurement, thought to be an upper bound as DSC and LVE indicate degradation starts at  $200^{\circ}\text{C}$ .

<sup>6</sup>PU10 is the same sample as PU600s in Chapter 4.

PE is the polyester form of corresponding PU ionomers (without  $-\text{NH}-$  group).

The two digit number XX in PUXX represents hard segment (HS) content in wt% of PU ionomer samples calculated from the feed. Both PE and SC-diol were used as reference samples with no hard segment and only have a single phase<sup>21</sup> but perhaps have ion aggregates<sup>22</sup>. Both of these two samples have  $T_g$  around  $-30^{\circ}\text{C}$  and are viscous liquids at room temperature, indicating the extra ester linkage in PE does not have strong

interaction to raise  $T_g$ . The slightly higher  $T_g$  of the SC-diol is perhaps because of higher ion content and more  $-OH$  end groups. In contrast, PU10 has  $25^\circ C$  higher  $T_g$  owing to the presence of  $-NH-$  groups acting as strong hydrogen bond donors. Note that PU10 is also a viscous liquid at room temperature and shows no evidence of microphase separation in SAXS (Figure 5-4). However, the Fox equation does not work in PU10 by using SC-diol  $T_g - 30^\circ C$  as the soft segment  $T_g$ , as that suggests a hard phase  $T_g$  over 3000K. The deviation from the Fox equation has been interpreted to imply microphase separation<sup>23, 24</sup> and/or different heat capacity contribution of hard and soft segment even in a single phase<sup>25</sup>. Samples with higher HS content start to microphase separate and are soft and rubbery pale yellow powders at room temperature, with a soft phase  $T_g$  at around  $0^\circ C$  regardless of HS content. This has been observed in the neutral polyurethane literature<sup>26</sup> and implies the amount of HS mixed in the soft phase is a constant once it reaches the critical concentration to microphase separate and/or more ions are trapped with increased hard phase. It is interesting that there is no significant difference ( $\pm 5K$ ) in soft phase  $T_g$  with samples from different preparation methods. No hard phase  $T_g$  or  $T_m$  was observed in DSC (Figure 5-3) before thermal degradation above  $200^\circ C$ . Although the TGA measurement indicates the onset of thermal degradation is above  $230^\circ C$  and increases with HS content, sample degradation (charred) was observed below  $230^\circ C$  during heating, suggesting the degradation occurs slowly at lower temperature.

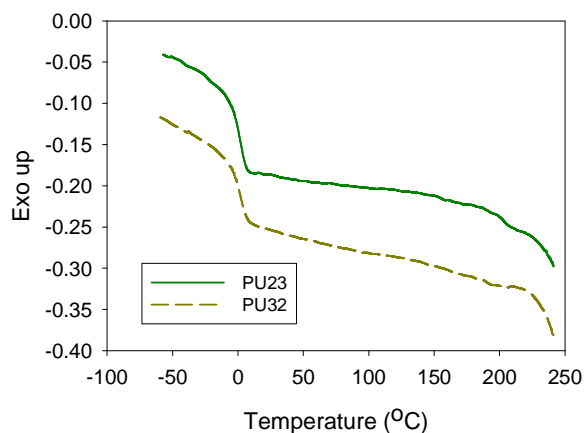


Figure 5-3: DSC study for PU23 and PU32.

The solubility is also affected by HS content. For HS content less than 10wt%, ionomers are soluble in polar solvents including water, DMSO, and DMF. PU23 and PU32 are soluble in DMSO but have poor solubility in water and DMF. PU40 can only swell in DMSO and is insoluble in water and DMF.

### 5.3.2 Small angle X-ray scattering (SAXS) and morphology

In order to further investigate microphase separation, SAXS spectra were collected and are shown in Figure 5-4. PU10, which is a viscous liquid at room temperature, shows no scattering, indicating single-phase morphology, as expected. In contrast, PU23 and PU32 prepared by either DMSO solution casting or hot pressing show clear microphase separation peaks. The peak position represents the spacing between two hard domains.<sup>27, 28</sup> The spacing of ~ 14 nm can be calculated by  $d = 2\pi/q_{\max}$  and is reported in Table 5-2. Hot pressed PU32 shows similar spacing as hot pressed PU23 but significant larger intensity, indicating better microphase separation and/or better contrast

between hard and soft phases. Both DMSO cast PU23 and PU32 films show significantly larger spacing than hot pressed samples, while PU23 shows lower intensity but PU32 higher intensity when solution cast. Solution casting from DMSO solution helps polymer chains relax and reach a state closer to equilibrium, with microphase separation better developed, hence the slightly larger spacing. The presence of DMSO allows urethane linkages to rearrange, interact more with the soft segment and possibly release the soft segment trapped in the hard domain in hot pressed samples, resulting in larger spacing and lower intensity (less amount of hard domain) for PU23. On the other hand, DMSO also allows the urethane linkage in PU32 to rearrange and interact with ion-containing soft segment but the larger amount of hard segment and urethane linkage also get a chance to trap the ion-containing soft segment since it is believed that  $\text{-NH}$  groups can interact with  $\text{-SO}_3^-$  anions in the soft segment strongly<sup>29</sup> imparting better contrast and higher intensity. Ions trapped in the hard domain will be revisited in section 5.3.4.

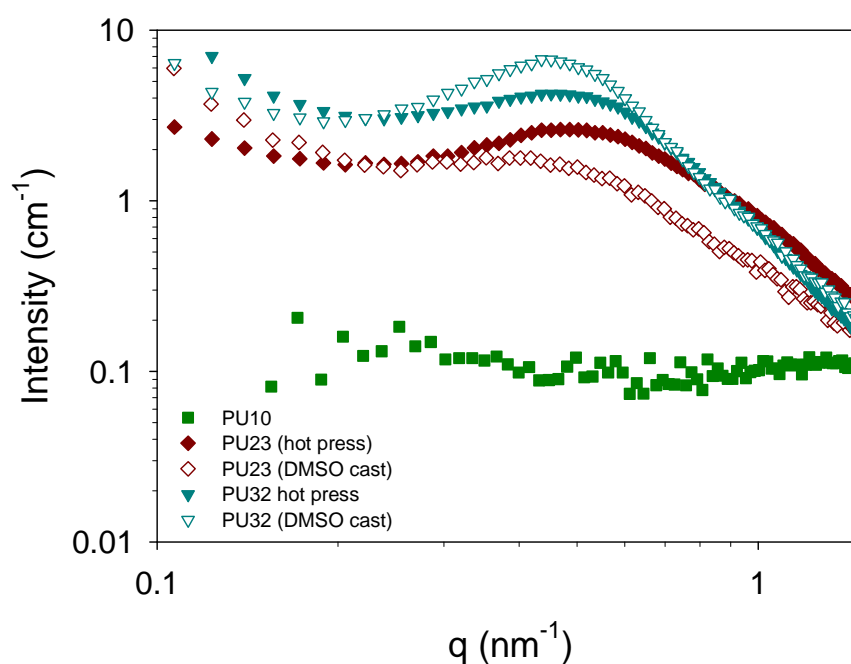


Figure 5-4: SAXS spectra of PU ionomer samples. Intensity was corrected by background and thickness. Open symbols: samples prepared by DMSO solution casting; filled symbols: samples prepared by hot pressing (except PU10).

Table 5-2: Spacing between hard domains from SAXS.

Sample	PU23		PU32	
	Hot press	DMSO cast	Hot press	DMSO cast
Spacing (nm)	13.2	15.6	13.7	14.7

### 5.3.3 Linear viscoelasticity

Microphase separation of PU can also be probed by linear viscoelastic response.<sup>30</sup>

<sup>31</sup> Figure Error! Reference source not found. shows the master curves of PU10 and vacuum molded PU23 and PU32. Note that PU10 is a viscous liquid at room temperature while PU23 and PU32 are solid. Time-temperature superposition (tTS) applies for PU10

suggesting single-phase morphology (no morphology changes), which agrees with our SAXS results. For PU23 and PU32, tTS only applies at low temperature and starts to fail at about 140°C. The failure of tTS implies breaking of hydrogen bonding and possibly a morphology change as well. In Figure Error! Reference source not found.(b), PU23 has a small relaxation in  $G''$  in the temperature range 100-140°C but this relaxation was not observed at higher temperature (160 and 180°C). It was found that this relaxation does not show up every time and disappears with longer annealing time. This may be due to unequilibrated hydrogen bonding or microphase separation.

Cole-Cole plots of these three samples are shown in Figure Error! Reference source not found.. PU10 collapses into a single curve perfectly again confirm the single phase morphology. A slope of 2 in Figure Error! Reference source not found.(a) is expected for homopolymer in terminal region.<sup>32</sup> The slope of 1 in the transition region of PU23 and PU32 suggests polydispersity as in most polycondensation polymers.<sup>32</sup> However, a slope of 2 in the terminal region was not observed for either PU23 or PU32. The leveling of  $G'$  at low frequencies suggest PU23 and PU32 are viscoelastic solids; the hard phase is immobile at these temperatures and acts as permanent crosslinks for the PEO-based soft phase. The failure of tTS suggests a morphology change<sup>33</sup>.

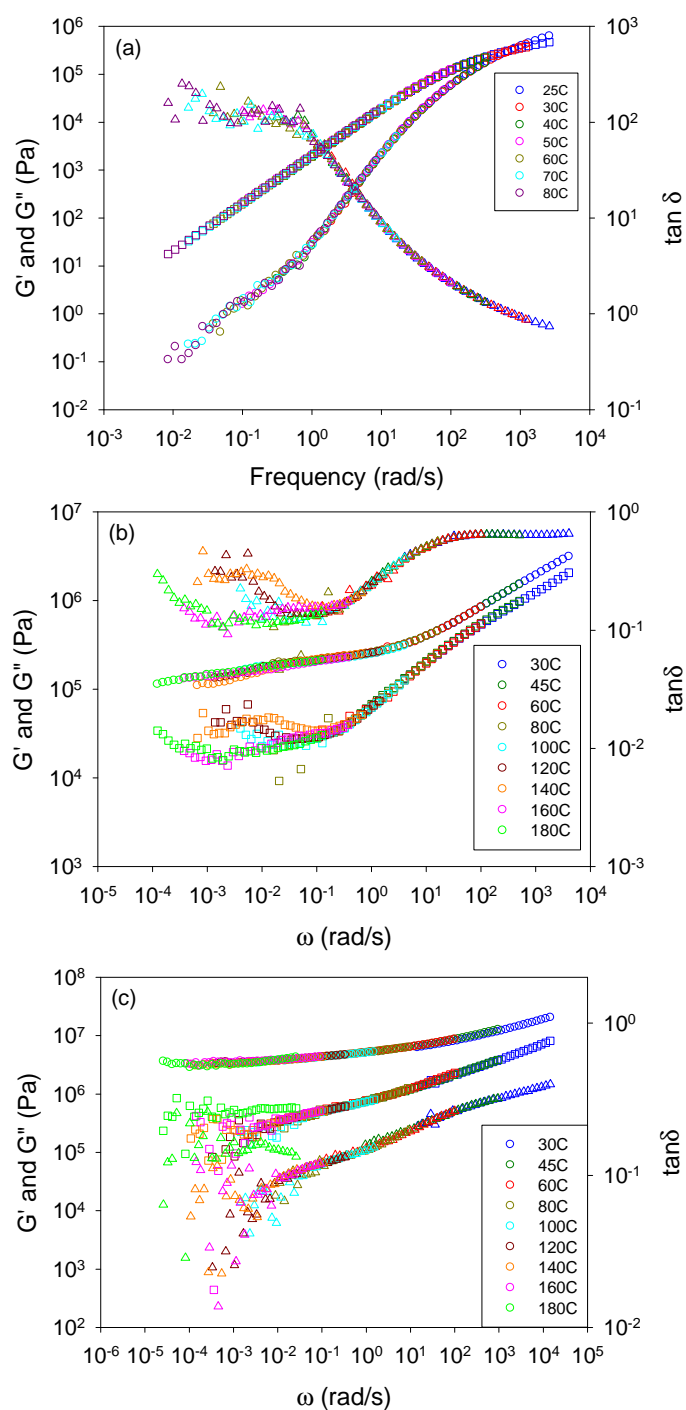


Figure 5-5: Master curves of (a) PU10 ( $T_{ref} = 50^\circ\text{C}$ ), (b) PU23 and (c) PU32 with  $T_{ref} = 60^\circ\text{C}$ . Sphere:  $G'$ ; square:  $G''$ ; triangle:  $\tan \delta$ . Please note that (a), (b) and (c) have different scales.

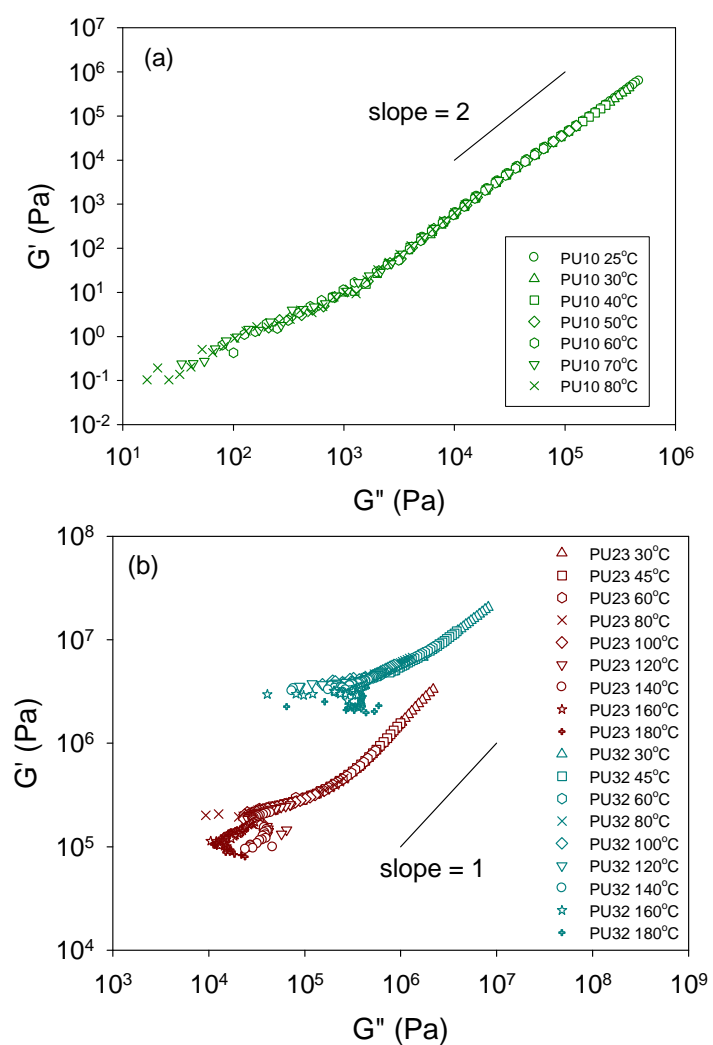


Figure 5-6: Cole-Cole plot of (a) PU10 and (b) PU23 and PU32.

Dynamic temperature step study was also used to investigate temperature effect and is shown in Figure 5-7. As expected, the storage modulus  $G'$  of PU10 decreases with temperature rapidly like most polymer melts<sup>34</sup>. The microphase separated samples PU23 and PU32 show that,  $G'$  remains roughly constant from 50 °C up to about 200°C. One

may consider the rapid drop of  $G'$  above  $200^{\circ}\text{C}$  to represent the hard phase  $T_g$  since TGA suggests the thermal degradation starts around  $230^{\circ}\text{C}$ . However, samples in the rheometer became charred below  $230^{\circ}\text{C}$ . Possible explanations are that the rheometer chamber was not entirely free of oxygen, although a nitrogen purge was applied throughout the experiment, or thermal degradation does happen below  $230^{\circ}\text{C}$  but the weight loss is not significant. Thus the rapid drop of  $G'$  can be the result of either hard phase melting or thermal degradation. PU32 shows about 10x larger  $G'$  than PU23 because PU32 has more hard segment and better microphase separation. However, PU23 and PU32 have relatively low  $G'$  compared to other pPDI-based PUs<sup>19, 35</sup> because there is no hard phase crystallinity. PU40 was not studied because of the difficulty of vacuum molding even at  $180^{\circ}\text{C}$ .

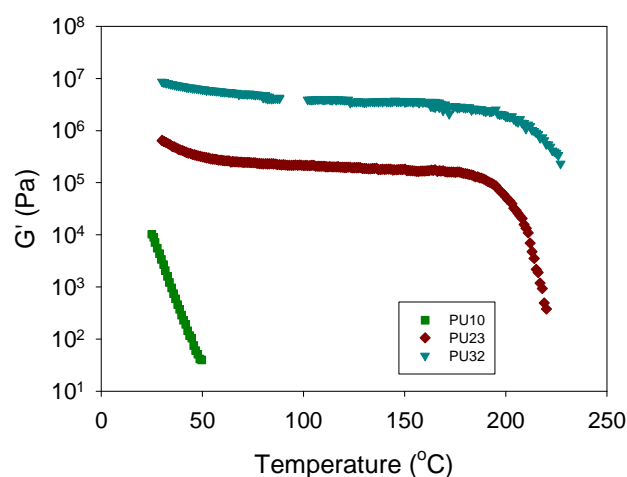


Figure 5-7: Dynamic temperature step study of PU ionomers at 1 rad/s.

---

### 5.3.4 Dielectric properties and ionic conductivity

Besides mechanical studies, DRS also gives very useful information about polymer relaxation as well as dielectric properties such as ionic conductivity.<sup>36, 37</sup> Polymer relaxation can be probed from dielectric loss spectra. However, for ion-conducting polymers, ion conduction usually dominates the loss spectra and often masks polymer relaxations. A common method to reveal polymer relaxation underneath ion conduction is to use Eq. 5-1, derived from the Kramers-Kronig relation, to obtain “conduction-free” derivative spectra.<sup>36, 38</sup>

$$\varepsilon_{der}(\omega) = -\frac{\pi}{2} \frac{\partial \varepsilon'(\omega)}{\partial \ln \omega} \quad (5-1)$$

Figure 5-8(a) shows the derivative spectra of ionomers with different amounts of HS. The polyester (PE) and the polyurethane without chain extender (PU10) ionomers show a segmental relaxation just before electrode polarization (EP) starts. In contrast, the microphase separated ionomers PU23 and PU32 show better defined segmental relaxations significantly before EP starts. More than one relaxation can be seen in these derivative spectra besides electrode polarization (EP).  $\varepsilon_{der}$  can be fitted with a power-law based EP and two Havriliak-Nagami functions (Eq. 5-2)<sup>21, 38</sup> to reveal both relaxations and the best fit is shown in Figure 5-8(b).

$$\varepsilon_{HN}^*(\omega) = \frac{\Delta\varepsilon}{[1 + (i\omega\tau_{HN})^a]^b} \quad (5-2)$$

where  $\Delta\varepsilon$  is relaxation strength,  $a$  and  $b$  are shape parameters and  $\tau_{HN}$  is a characteristic relaxation time.

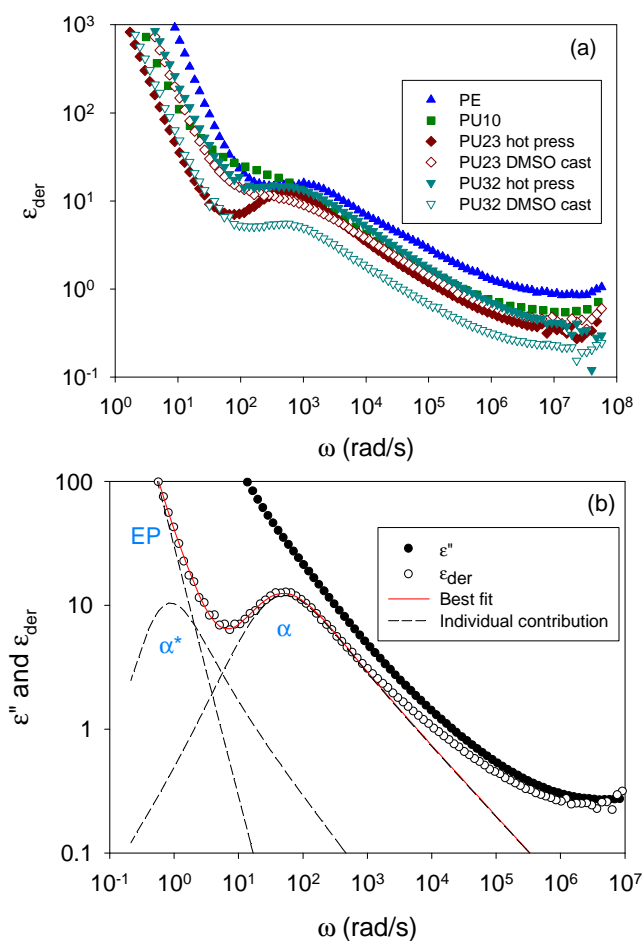


Figure 5-8: (a)“Conduction-free” derivative spectra of ionomers with various hard segment content and sample preparation methods at  $T = T_g + 20\text{K} (\pm 5\text{K})$ . (b) Comparison of  $\epsilon''$  and  $\epsilon_{\text{der}}$  spectra and the best fit with power-law EP and two Havriliak-Nagami functions for hot pressed PU23 at  $10^\circ\text{C}$ .

These two relaxations are assigned to  $\alpha$  and  $\alpha^*$  relaxation corresponding to polymer chain and ion (ion pairs and/or ion aggregates) associated chain relaxation, respectively<sup>17, 18, 21</sup>. Temperature dependence of frequency  $\omega_\alpha$  of the  $\alpha$  relaxation and  $\omega_{\alpha^*}$  of the  $\alpha^*$  relaxation are shown in Figure 5-9. Both  $\alpha$  and  $\alpha^*$  relaxations follow the Vogel-Fulcher-Tammann (VFT) equation:

$$\omega(T) = \omega_0 \exp\left(\frac{-DT_0}{T - T_0}\right) \quad (5-3)$$

where  $\omega_0$  is the unconstrained (high T) frequency,  $T_0$  is the Vogel temperature and D is a parameter that is inversely related to fragility. Fitting parameters of  $\omega_\alpha$  or  $\omega_{\alpha^*}$  are summarized in Table 5-3. Note that  $T_g$  obtained by extrapolating Eq. 5-3 to  $\omega_\alpha$  or  $\omega_{\alpha^*}$  equals to 0.01 rad/s agrees with DSC soft phase  $T_g$  suggesting both relaxations are related to chain relaxation. Meanwhile, both  $\omega_\alpha$  and  $\omega_{\alpha^*}$  can be fitted with a common  $T_0 = 202\text{K}$  with  $R^2 \geq 0.98$  (parameters shown in Table 5-4). This common  $T_0 = 202\text{K}$  is similar to other PEO-based polyester and PU ionomers<sup>18, 21</sup>, which again suggests that both  $\alpha$  and  $\alpha^*$  are related to PEO chain relaxation. The  $\alpha^*$  relaxation was particularly well resolved in the derivative spectra of a series of PEO-based polyester ionomers<sup>21</sup>, for which independent fits yielded  $197\text{K} < T_0 < 203\text{K}$  for  $\alpha$  and  $199\text{K} < T_0 < 201\text{K}$  for  $\alpha^*$ . (Actually, all the PU ionomers can be fitted to a common  $T_0$  at  $\sim 202 - 210\text{K}$  while PE shows a much better fit with lower  $T_0$  as in Table 5-3. The possible reason is that in PU ionomers, the urethane linkages in the PEO phase still slightly raise  $T_0$ . PE has a significantly lower  $T_0$ , possibly due to the weaker sulfonate fumarate-PEO interaction than sulfonate phthalate-PEO interaction seen in Chapter 4.) We can see that D increases (fragility decreases) significantly from PE to PU10 because of strong interaction from hydrogen bonds.<sup>39, 40</sup> Differences in D for microphase separated samples may be due to different amount of HS mixed in the soft phase.

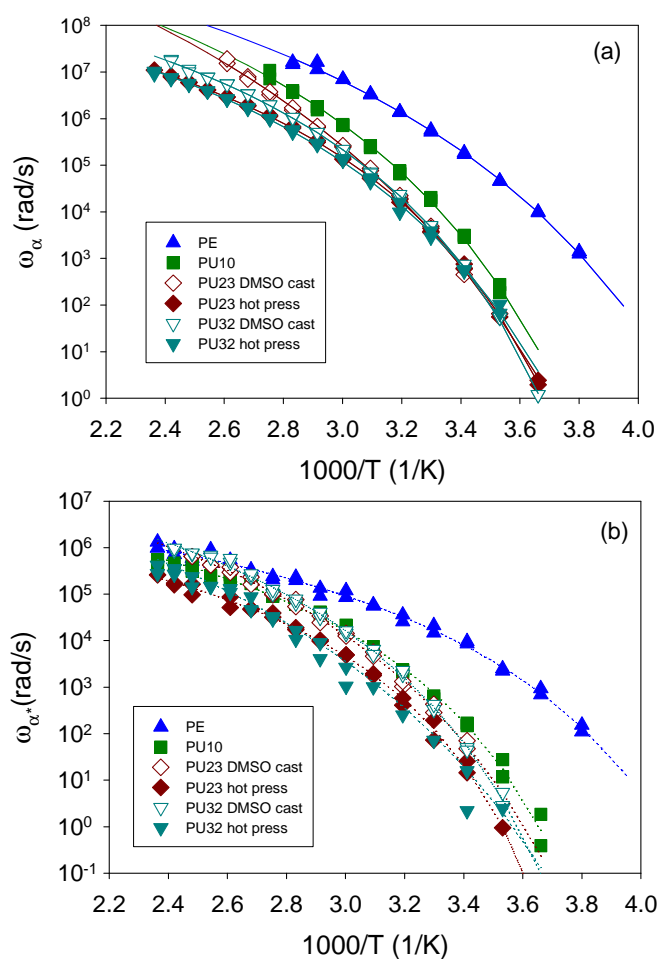


Figure 5-9: (a)  $\alpha$  and (b)  $\alpha^*$  relaxation frequency as a function of temperature. Solid and dotted lines are fitting results to VFT equation with parameters summarized in Table 5-3 and 5-4.

Table 5-3: VFT fitting parameters of  $\omega_\alpha$  and  $\omega_{\alpha^*}$  relaxations.

Sample	preparation method	$T_g$ (K)	$\omega_\alpha$			$\omega_{\alpha^*}$		
			$\log \omega_0$	$T_0$ (K)	D	$\log \omega_0$	$T_0$ (K)	D
PE		240	11.0	183	7.90	7.46	201	3.78
PU10		268	11.1	209	7.16	7.69	224	3.88
PU23	DMSO cast	277	12.2	191	11.5	8.75	214	5.95
	hot press	277	9.38	221	4.96	7.19	235	3.39
PU32	DMSO cast	276	9.84	221	5.26	8.6	223	5.02
	hot press	276	9.66	212	6.07	9.02	199	8.50

Table 5-4: VFT fitting parameters of  $\omega_\alpha$  and  $\omega_{\alpha^*}$  relaxations with  $T_0 = 202\text{K}$ .

Sample	preparation method	$T_g$ (K)	$\omega_\alpha$				$\omega_{\alpha^*}$			
			$\log \omega_0$	$T_0$ (K)	D	$R^2$	$\log \omega_0$	$T_0$ (K)	D	$R^2$
PE		240	10.1	202	4.90	0.996	7.44	202	3.70	0.994
PU10		268	11.5	202	8.36	0.998	8.67	202	6.84	0.988
PU23	DMSO cast	272	11.6	202	9.25	0.998	9.23	202	7.72	0.996
	hot press	275	10.3	202	7.87	0.996	8.50	202	8.10	0.985
PU32	DMSO cast	271	10.9	202	8.51	0.996	9.53	202	8.10	0.995
	hot press	275	10.0	202	7.51	0.998	8.89	202	7.97	0.994

It is surprising that microphase separated samples (PU23 and PU32) do not have an extra Maxwell-Wagner-Sillars (MWS) interfacial polarization peak compared to homogeneous PE and PU10. MWS originates from different charge mobility between two phases and is very common in PUs with microphase separation above their soft phase  $T_g$ .<sup>41, 42</sup> A possible explanation can be that MWS happens at similar frequency with other events in Figure 5-8<sup>43, 44</sup>. This also would explain some the unusually large relaxation strengths of  $\alpha$  and  $\alpha^*$  relaxation ( $\Delta\epsilon \approx 10-40$ ) as well as broader EP, compared to the literature<sup>21, 40, 45</sup> and single-phase PE and PU10. However, further resolving of MWS from  $\alpha$  and  $\alpha^*$  relaxation and EP would introduce more parameters (2 parameters from EP and total 12 parameters for 3 HN functions) and seems impossible to resolve.

Figure 5-10(a) shows the temperature dependence of ionic conductivity. The SC-diol has the highest ionic conductivity because of its low  $T_g$  and low MW. It gives the upper limit of possible conductivity if microphase separation were complete. PE and PU10 also have higher conductivity compared to other samples due to their lower  $T_g$ . Note that conductivity of PE and PU10 merge at high temperature, suggesting similar ion conduction in PE and PU10. PU23 and PU32 have the same soft phase  $T_g$  but very

different ionic conductivity. At the same time, sample preparation also affects conductivity; however, the effect is very different in PU23 and PU32. For PU23, the DMSO cast sample shows higher conductivity while the hot pressed sample has higher conductivity for PU32. This phenomenon shows good correlation with our SAXS results: samples with stronger SAXS peaks (hot pressed PU23 and DMSO cast PU32) have lower conductivity.

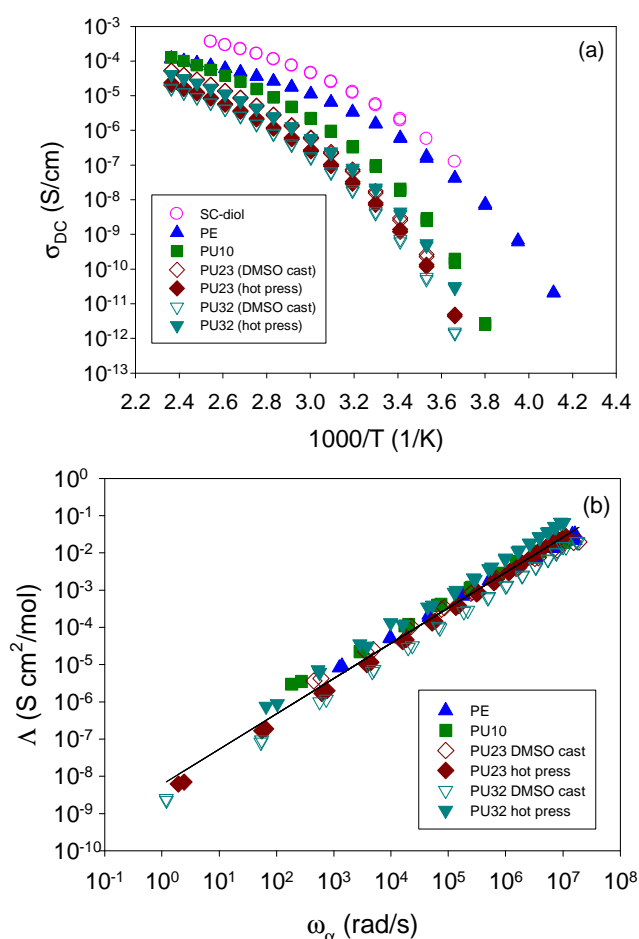


Figure 5-10: (a) Ionic conductivity as a function of reciprocal temperature; (b) Molar conductivity as function of  $\alpha$ -relaxation frequency. Solid line is the best fit with fractal DSE equation:  $\Lambda = 6 \times 10^{-9} \omega_\alpha^{0.95 \pm 0.01}$ .

The conductivity data can be reduced to a single power law by plotting against  $\alpha$ -relaxation frequency as in Figure 5-10(b). It is believed that ion transport depends on polymer relaxation for PEO-based ionomers<sup>2, 18, 21, 46</sup> and the dependence empirically follows the fractal Debye-Stokes-Einstein (DSE) equation (Eq. 5-4)<sup>47, 48</sup>:

$$\mu_{avg} = \frac{\sigma_{DC}}{ep_{tot}} = \frac{1}{e} \Lambda \sim \left( \frac{\omega_{\alpha}}{T} \right)^s \quad (5-4)$$

where  $\mu_{avg}$  is average ion mobility of all ions,  $e$  is the elementary charge,  $p_{tot}$  is theoretical ion content calculated from chemical structure and  $\Lambda$  is molar conductivity. Since the relative temperature change is small compared to  $\omega_{\alpha}$ , molar conductivity is plotted against  $\omega_{\alpha}$  in Figure 5-10(b) for simplicity. The slope slightly smaller than unity (0.95) suggests ion transport is strongly coupled with polymer relaxation as reported in our other study on PU ionomers<sup>18</sup>.

To further investigate ion transport, an electrode polarization model (EP model, Macdonald/Coelho model)<sup>49-51</sup> was applied to separate conducting ion content and their mobility at any given instant in time. For a single-ion conductor with blocking electrodes under electric field, the conductivity and the polarization can be described as (Eq. 5-5, Eq. 5-6):

$$\sigma_{DC} = e\mu p \quad (5-5)$$

$$\tan \delta = \frac{\varepsilon''}{\varepsilon'} = \frac{\omega \tau_{EP}}{1 + \omega^2 \tau_{\sigma} \tau_{EP}} \quad (5-6)$$

where  $\tau_\sigma$  and  $\tau_{EP}$  are time scales of ion conduction and full electrode polarization (Eq. 5-7 Eq. 5-8):

$$\tau_\sigma \equiv \frac{\epsilon_s \epsilon_0}{\sigma_{DC}} \quad (5-7)$$

$$\tau_{EP} \equiv \frac{\epsilon_{EP} \epsilon_0}{\sigma_{DC}} \quad (5-8)$$

where  $\epsilon_s$  is the static dielectric constant of polymer,  $\epsilon_{EP}$  is the dielectric constant when EP is completed and  $\epsilon_0$  is the vacuum permittivity. Please note that the peak of  $\tan\delta$  become wider with smaller magnitude in microphase separated samples (especially for PU40, data not shown) compared to the homogeneous samples (such as PU10 and ionomers discussed in Chapter 4). This is very likely because MWS relaxation occurs at the same time scale and the  $\tan\delta$  peak is the combination of both MWS relaxation and EP. This also implies that the prediction  $\tau_\sigma$  and  $\tau_{EP}$  (as well as  $p$  and  $\mu$  discussed below) become less reliable with high degree of microphase separation. At any given instant, conducting ion concentration and their mobility can be obtained with  $L$  as the sample film thickness (Eq. 5-9 Eq. 5-10):

$$p = \frac{4\sigma_{DC}\tau_{EP}^2 kT}{e^2 L^2 \tau_\sigma} \quad (5-9)$$

$$\mu = \frac{eL^2 \tau_\sigma}{4\tau_{EP}^2 kT} \quad (5-10)$$

Figure 5-11 shows conducting ion concentration divided by theoretical ion content,  $p_{\text{tot}}$ , as a function of temperature. It is clear that the conducting ion concentration follows the Arrhenius equation:

$$p = p_0 \exp\left(\frac{-E_a}{kT}\right) \quad (5-11)$$

where  $E_a$  is activation energy and  $p_0$  is the conducting ion content at infinite high temperature. Note that  $p_0$  here represents the total amount of ion that is *available to contribute to conductivity* under electric field and is not necessary equal to the theoretical total ion content  $p_{\text{tot}}$ .

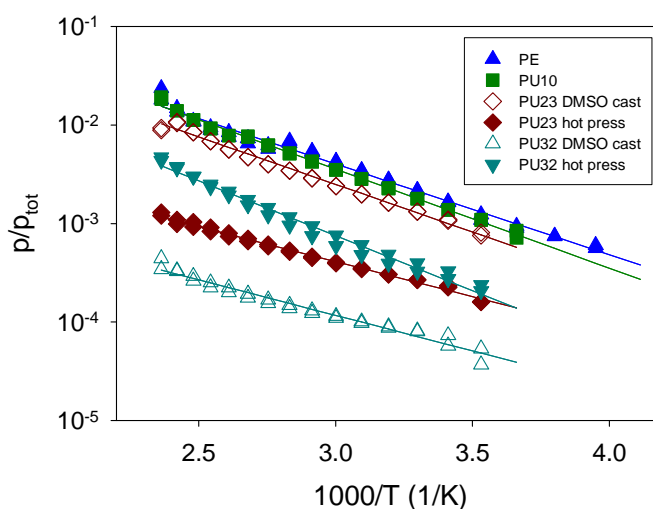


Figure 5-11: Normalized conducting ion concentration as a function of temperature. Solid lines are best fits to the Arrhenius equation (Eq. 5-11) with fitting parameters in Table 5-5.

Table 5-5 gives the fitting parameters of the Arrhenius equation for conducting ion content. At any given instant, less than 10% of the  $\text{Na}^+$  are participating in conduction and the majority of  $\text{Na}^+$  are in pair or aggregate states. PE, PU10, DMSO cast PU23 and hot pressed PU32 have similar  $p_0$  which is very close to  $p_{\text{tot}}$  (Table 5-1) suggesting all

Na<sup>+</sup> contributes to conductivity. Hot pressed PU23 and DMSO cast PU32 have lower  $p_0$  indicating that a certain amount of Na<sup>+</sup> are trapped in the hard domain and cannot contribute to conductivity<sup>18</sup>. This observation agrees with our previous analysis of SAXS spectra and also explains the lower conductivity of hot pressed PU23 and DMSO cast PU32 in Figure 5-10. PE has slightly lower activation energy compared to our previous studies<sup>21,51</sup> on PEO-based polyester single-ion conductors, possibly due to different anion species. PU10, DMSO cast PU23 and hot pressed PU32 have similar  $p_0$  but lower  $p$  at all studied temperatures and larger activation energy with increasing HS content implying worse solvation ability in the presence of the urethane linkage. The activation energy decreases with less available conducting ions due to higher EO/Na<sup>+</sup> ratio, as reported by<sup>21</sup> when they varied ion content in PEO-polyester ionomers.

Table 5-5: Fitting parameters for conducting ion content (Eq. 5-11) and their mobility (Eq. 5-12).

Sample	Preparation method	$T_g$ (K)	Conducting ion content $p$ (1/cm <sup>3</sup> )		Cation mobility $\mu$ (cm <sup>2</sup> /Vs)		
			$\log p_0$	$E_a$ (kJ/mol)	$\log \mu_0$	$T_0$ (K)	$D$
PE		240	21.1	17.6	-2.85	214	2.13
PU10		268	21.3	19.2	-2.54	229	2.70
PU23	DMSO cast	272	20.9	18.5	-2.58	234	2.77
	hot press	275	19.4	13.6	-1.75	227	3.52
PU32	DMSO cast	271	18.8	13.8	-1.26	230	3.47
	hot press	275	20.8	21.3	-2.53	238	2.15

The mobility of these “free” Na<sup>+</sup> follows VFT behavior and is shown in Figure 5-12 with fitting parameters summarized in Table 5-5.

$$\mu = \mu_0 \exp\left(\frac{-DT_0}{T - T_0}\right) \quad (5-12)$$

where  $\mu_0$  is unconstrained (high T) cation mobility. Unlike  $\omega_\alpha$  and  $\omega_{\alpha^*}$ , cation mobility cannot be fit with a common  $T_0$ . Instead, PE has  $T_0$  of 214K as reported previously<sup>21</sup> and all PUs have higher  $T_0$  of 230-240K, reflecting the higher  $T_g$  of the soft phase. For this reason, Figure 5-12 is plotted against  $T_g/T$ . It is interesting that PE, PU10 and DMSO cast PU23 have the same mobility, while other microphase separated samples have *higher* mobility. A possible explanation is that the presence of the hard phase provides well-ordered –NH– groups at the interface that can interact with sulfonate groups and allow cations to move along the interface, resulting in higher mobility. On the other hand, this can also simply be the error of EP fitting because of the presence of MWS relaxation at the same frequency range.

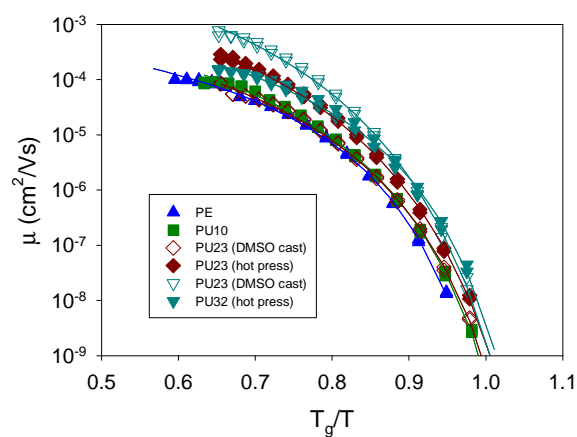


Figure 5-12: Cation mobility as a function of  $T_g/T$ . Solid lines are fit to VFT equation (Eq. 5-12)

## 5.4 Conclusion

In this chapter, sulfonate group containing PEO-based diol (SC-diol) was synthesized and used as the soft segment for PU ionomers. It was found that > 20wt% of hard segment is required for SC-diol based PU ionomers to microphase separate, even with symmetric pPDI and butane diol as hard segment components, because both sulfonate group and ether oxygens can compete for hydrogen bonds between urethane linkages. Microphase separation of PU23 and PU32 was probed by both SAXS and rheology. Time-temperature superposition fails for both PU23 and PU32 above 140°C suggesting the morphology changes above 140°C but storage modulus remains constant until ~200°C. Sample preparation is very critical for both morphology and ionic conductivity. However, the effect of DMSO solution casting depends on composition of PU ionomers and does not have a clear rule: it helps microphase separation in PU32 but reduces microphase separation for PU23.

It was found that fractal DSE equation works in this ion-in-soft-segment PU system. Ionic conductivity is strongly coupled with PEO chain relaxation as reported in our previous ion-in-hard-segment PU ionomer study<sup>18</sup>. It was also found that microphase separation can trap ions in the hard domain but at the same time, the interface perhaps provides a well-ordered “path” for higher cation mobility. Throughout this chapter, it was demonstrated that the requirements of both mechanical strength and ionic conductivity can be reached by microphase separated polyurethane ionomers. In all samples studied in this chapter, hot pressed PU32 has the best balance between ionic conductivity and mechanical strength. It has storage modulus of 4 MPa up to 200°C with ionic

conductivity of  $4 \times 10^{-5}$  S/cm at 150°C. For future direction, increasing PEO spacer length in the SC-diol should help decrease soft phase  $T_g$  to increase conductivity as well as microphase separation<sup>52</sup> and further improve both mechanical strength and ionic conductivity.

## 5.5 References

1. Fenton, D. E.; Parker, J. M.; Wright, P. V. *Polymer* **1973**, 14, 589.
2. Meyer, W. H. *Advanced Materials* **1998**, 10, (6), 439-448.
3. Song, J. Y.; Wang, Y. Y.; Wan, C. C. *Journal of Power Sources* **1999**, 77, 183-197.
4. Snyder, J. F.; Carter, R. H.; Wetzel, E. D. *Chemistry of Materials* **2007**, 19, 3793-3801.
5. Chandrasekhar, V. *Advances in Polymer Science* **1998**, 135, 139-205.
6. Singh, M.; Odusanya, O.; Wilmes, G. M.; Eitouni, H. B.; Gomez, E. D.; Patel, A. J.; Chen, V. L.; Park, M. J.; Fragouli, P.; Iatrou, H.; Hadjichristidis, N.; Cookson, D.; Balsara, N. P. *Macromolecules* **2007**, 40, (13), 4578-4585.
7. Gomez, E. D.; Panday, A.; Feng, E. H.; Chen, V.; Stone, G. M.; Minor, A. M.; Kisielowski, C.; Downing, K. H.; Borodin, O.; Smith, G. D.; Balsara, N. P. *Nano Letters* **2009**, 9, (3), 1212-1216.
8. Soo, P. P.; Huang, B.; Jang, Y.-I.; Chiang, Y.-M.; Sadoway, D. R.; Mayes, A. M. *Journal of The Electrochemical Society* **1999**, 146, (1), 32-37.
9. Visser, S. A.; Cooper, S. L. *Macromolecules* **1991**, 24, 2576-2583.
10. Ding, Y. S.; Register, R. A.; Yang, C.-z.; Cooper, S. L. *Polymer* **1989**, 30, 1204-1212.
11. Yang, C.-Z.; Grasel, T. G.; Bell, J. L.; Register, R. A.; Cooper, S. L. *Journal of Polymer Science: part B: Polymer Physics* **1991**, 29, 581-588.
12. Krol, P.; Krol, B.; Holler, P.; Telitsyna, N. *Colloid and Polymer Science* **2006**, 284, (10), 1107-1120.
13. Kakati, D. K.; George, M. H. *Polymer* **1993**, 34, (20), 4319-4324.
14. Williams, S. R.; Wang, W.; Winey, K. I.; Long, T. E. *Macromolecules* **2008**, 41, 9072-9079.
15. Polizos, G.; Kyritsis, A.; Pissis, P.; Shilov, V. V.; Shevchenko, V. V. *Solid State Ionics* **2000**, 136, 1139-1146.
16. Xu, H.-S.; Yang, C.-Z. *Journal of Polymer Science: Part B: Polymer Physics* **1995**, 33, 745-751.
17. Fragiadakis, D.; Dou, S.; Colby, R. H.; Runt, J. *Macromolecules* **2008**, 41, 5723-5728.
18. Wang, S.-W.; Liu, W.; Colby, R. H. *Chemistry of Materials* **2011**, 23, 1862-1873.

19. Sheth, J. P.; Klinedinst, D. B.; Wilkes, G. L.; Yilgor, I.; Yilgor, E. *Polymer* **2005**, 46, 7317-7322.
20. Wang, X.; Li, H.; Tang, X.; Chang, F.-C. *Journal of Polymer Science Part B-Polymer Physics* **1999**, 37, 837-845.
21. Fragiadakis, D.; Dou, S.; Colby, R. H.; Runt, J. *The Journal of Chemical Physics* **2009**, 130, 064907.
22. Wang, W.; Liu, W.; Tudryn, G. J.; Colby, R. H.; Winey, K. I. *Macromolecules* **2010**, 43, 4223-4229.
23. McLennaghan, A. W.; Pethrick, R. A. *European Polymer Journal* **1988**, 24, (11), 1063-1071.
24. Lee, D.-c.; Register, R. A.; Yang, C.-z.; Cooper, S. L. *Macromolecules* **1988**, 21, 1005-1008.
25. Koberstein, J. T.; Leung, L. M. *Macromolecules* **1992**, 25, 6205-6213.
26. Koberstein, J. T.; Galambos, A. F.; Leung, L. M. *Macromolecules* **1992**, 25, (23), 6195-6204.
27. Choi, T.; Weksler, J.; Padsalgikar, A.; Runt, J. *Polymer* **2009**, 50, 2320-2327.
28. Bonart, R.; Muller, E. H. *Journal of Macromolecular Science, Physics* **1974**, B10, (1), 177-189.
29. Lam, P. K. H.; George, M. H.; Barrie, J. A. *Polymer* **1989**, 30, (12), 2320-2323.
30. Velankar, S.; Cooper, S. L. *Macromolecules* **2000**, 33, 395-403.
31. Han, C. D., Linear Dynamic Viscoelasticity of TPUs. In *Rheology and Processing of Polymeric Materials*, Oxford University Press: New York, 2007; Vol. 1, pp 484-486.
32. Han, C. D., Rheology of flexible homopolymers. In *Rheology and Processing of Polymeric Materials: Polymer Rheology*, Oxford University Press: New York, 2007; Vol. 1.
33. Yoon, P. J.; Han, C. D. *Macromolecules* **2000**, 33, 2171-2183.
34. Rubinstein, M.; Colby, R. H., Unentangled polymer dynamics. In *Polymer Physics*, Oxford University Press: New York, 2007.
35. Sheth, J. P.; Klinedinst, D. B.; Pechar, T. W.; Wilkes, G. L.; Yilgor, E.; Yilgor, I. *Macromolecules* **2005**, 38, (24), 10074-10079.
36. Kremer, F.; Schonhals, A., *Broadband Dielectric Spectroscopy*. Springer: 2003.
37. Pissis, P.; Polizos, G., Molecular dynamics and ionic conductivity studies in polyurethane thermoplastic elastomers. In *Handbook of condensation thermoplastic elastomers*, Fakirov, S., Ed. Wiley-VCH: 2005; pp 381-429.
38. Wubbenhorst, M.; van Turnhout, J. *Journal of Non-Crystalline Solids* **2002**, 305, (1-3), 40-49.
39. Angell, C. A. *Proceedings of the National Academy of Sciences of the United States of America* **1995**, 92, 6675-6682.
40. Tsonos, C.; Apekis, L.; Zois, C.; Tsonos, G. *Acta Materialia* **2004**, 52, 1319-1326.
41. North, A. M.; Reid, J. C.; Shortall, J. B. *European Polymer Journal* **1969**, 5, 565-573.
42. North, A. M.; Reid, J. C. *European Polymer Journal* **1972**, 8, 1129-1138.
43. Kanda, D. H. F.; Nagashima, H. N.; Malmonge, J. A.; Sakamoto, W. K.; Chierice, G. O. *Journal of materials science* **2008**, 43, 5436-5440.

44. Pissis, P.; Kanapitsas, A.; Savelyev, Y. V.; Akhranovich, E. R.; Privalko, E. G.; Privalko, V. P. *Polymer* **1998**, 39, (15), 3431-3435.
45. Georgoussis, G.; Kyritsis, A.; Pissis, P.; Savelyev, Y. V.; Akhranovich, E. R.; Privalko, E. G.; Privalko, V. P. *European Polymer Journal* **1999**, 35, 2007-2017.
46. Borodin, O.; Smith, G. D. *Macromolecules* **2006**, 39, 1620-1629.
47. Corezzi, S.; Campani, E.; Rolla, P. A.; Capaccioli, S. *Journal of Chemical Physics* **1999**, 11, (20), 9343-9351.
48. Becker, S. R.; Poole, P. H.; Starr, F. W. *Physical Review Letters* **2006**, 97, 055901.
49. Macdonald, J. R. *Physical Review* **1953**, 92, 4-17.
50. Coelho, R. *Journal of Non-Crystalline Solids* **1991**, 131-133, 1136-1139.
51. Klein, R. J.; Zhang, S.; Dou, S.; Jones, B. H.; Colby, R. H.; Runt, J. *The Journal of Chemical Physics* **2006**, 124, 144903.
52. Chu, B.; Gao, T.; Li, Y.; Wang, J.; Desper, C. R.; Byrne, C. A. *Macromolecules* **1992**, 25, 5724-5729.

## Chapter 6

### Conclusion and Future Work

Throughout this thesis, pPDI/PEO polyurethane ionomers with ions in either hard segment or soft segment were synthesized and characterized in terms of (1) morphology by SAXS; (2) mechanical properties by linear viscoelastic methods; (3) thermal analysis by DSC; (4) ion conduction and segmental relaxation by DRS. In polyurethane ionomers with ions in the hard segment, a carboxylate group was attached between two pPDI molecules. The effect of various counterions from  $\text{Na}^+$  to large ionic liquid type cations was discussed. It was found that there is no discrete microphase separation between hard and soft phase even with 40wt% hard segment content, because the ions in the hard segment significantly interrupt hydrogen bonding between urethane linkages and this promotes phase mixing. However, more than 50% of the counterions are trapped in pPDI-carboxylate-pPDI and are not able to respond to the electric field and contribute to ionic conductivity. With increasing counterion size, the DSC  $T_g$  decreases and ionic conductivity increases, as expected. All ionomers have ionic conductivity strongly coupled to polymer relaxation and follow the Debye-Stokes-Einstein equation perfectly, meaning that ionic conductivity is proportional to segmental relaxation of PEO because the dielectric strength of the segmental relaxation is nearly independent of temperature.

To solve the problem of ion trapping by the hard segment, ion containing (sulfonate-centered) diols (SC-diols) were synthesized by reacting sulfonated fumarate with an excess of PEO, and these SC-diols were then used to prepare polyurethane

ionomers with ions in the soft segment. Still no discrete microphase separation was detected by SAXS for SC-diol based polyurethane ionomers without chain extender, even with 39wt% hard segment content for PU200s with short SC-diol, but no ions are trapped in the hard segment as in Chapter 2. Significantly higher  $T_g$  of polyurethane ionomers compared to SC-diols was measured due to strong hydrogen bonding between urethane linkages and PEO. Unlike polyurethane ionomers with ions in the hard segment, samples with ions in the soft segment show ionic conductivity slightly decoupled from polymer segmental relaxation. But a perfect coupling with the slower ion mode relaxation was found. On the other hand, Barton-Nakajima-Namikawa relation provides better correlation and scales the relationship between relaxation and conductivity better, which would be an excellent topic and method for future analysis.

To enhance microphase separation, polyurethane ionomers with PEO 600 based SC-diols with different amounts of butane diol chain extender were synthesized. Samples with more than 23wt% of hard segment microphase separate and have a soft phase  $T_g$  at  $\sim 0^\circ\text{C}$ , independent of hard segment content. These microphase separated samples are solids with modulus  $\sim \text{MPa}$  up to  $200^\circ\text{C}$  (Figure 6-1). The degree of microphase separation also depends on the preparation method: DMSO cast PU32 films show better microphase separation than hot pressed film while PU23 has opposite behavior. The films with better microphase separation were found to trap more ions in the hard phase and result in lower ionic conductivity. Overall, the hot pressed PU32 has shear modulus of 4 MPa and ionic conductivity of  $2 \times 10^{-5} \text{ S/cm}$  at  $150^\circ\text{C}$ , which demonstrates the potential of microphase separated polyurethane ionomers compared to PEO-based homopolymers in Figure 6-1.

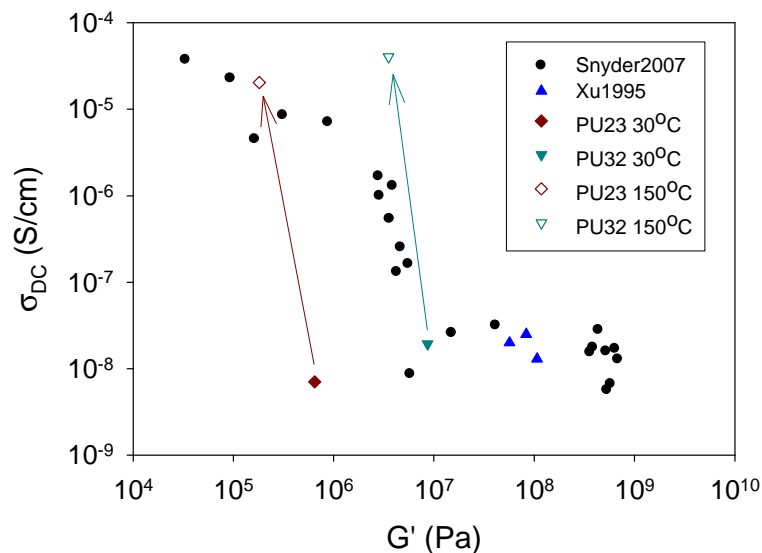


Figure 6-1: Relationship between ionic conductivity and mechanical strength for PEO-based ion-containing homopolymers and PU23 and PU32 in Chapter 5. (Please see Figure 1-1 for references)

To further improve the desired properties of polyurethane ionomers and understand the detailed structure property relationship, I suggest the following six potential topics for the future work.

**1. Longer PEG spacers.** It has been proved in Chapter 4 that with short PEG spacer, the polyurethane ionomers have high  $T_g$  and no microphase separation. Note that although short PEG gives the products high hard segment content, it does not help microphase separation between hard and soft segment possibly because the urethane linkages cannot effectively form ordered hydrogen bonds. At the same time, both ionic groups and urethane linkages behave as physical crosslinks in polyurethane ionomers, so with short PEG spacer, the ionomers have a high crosslink density. Without microphase separation, PEG in these ionomers can only relax after breakdown of these crosslinks

leading to high  $T_g$  and low ionic conductivity. Increasing PEG length will for sure decrease the total ion density but since we know that there is only a very small fraction of these ions are conducting in a given instant, the increasing EO/cation ratio would improve the conducting ion fraction. At the same time, longer PEG and lower total ion density will lower  $T_g$  and increase segmental relaxation rate and ion mobility. Also, the longer PEG may help urethane linkages form ordered hydrogen bonds more easily and improve microphase separation. One thing needs to be noticed is that PEG tends to crystallize with a molecular weight larger than 1000 and the  $T_m$  increases with precursor molecular weight. However, both urethane linkages and ions interact strongly with PEG and should reduce the crystallinity. PEGs with a molecular weight less than 2000 can be very good candidates. Besides, adding a small amount of PEG with different molecular weight may also help to reduce crystallinity.

**2. Polyurethane-ureas and polyureas.** It is well known that urea linkages have much stronger hydrogen bonding than urethane linkages and polyureas have more pronounced microphase separation than polyurethanes. By introducing a small amount of urea linkage, the ionomer may be able to microphase separate at smaller hard segment content. The better microphase separation would also lead to purer soft phase and reduce soft phase  $T_g$ , boosting ionic conductivity. Polyurethane-urea ionomers can be prepared by either using a diamine chain extender or curing the prepolymer (oligomer prepared by reacting diols with excess of diisocyanates) in the air (see Figure 1.2). Take pPDI as example diisocyanate, using a diamine chain extender would place a short spacer in the hard segment as pPDI-urea-spacer-urea-pPDI, while curing prepolymer in the air would connect two diisocyanate groups with urea linkage like pPDI-urea-pPDI without any

spacer in between. The advantage of curing the prepolymer is that prepolymer usually has low viscosity compared to the final polyurethane-urea product and can be processed easily. The polyurethane-urea film can be prepared by coating the prepolymer on a substrate and then letting it be cured by air. However, the side product of this method is  $\text{CO}_2$  and  $\text{CO}_2$  may result in bubbles in the film. Polyurethane-urea prepared by using a diamine chain extender will not have this problem but notice should be taken that urea linkages form very strong hydrogen bonds and can precipitate from the solution or form gel during the reaction so the amount of diamine used should be carefully calculated. Another method is to use SC-diamines instead of SC-diols. By this method a polyurea can be prepared and it is possible to have microphase separation without chain extender. It would be very interesting to compare ionomers prepared by these two methods, with the same amount of urea linkages. One important thing to keep in mind of these polyurethane-urea or polyurea is that too much urea linkage would make the materials completely insoluble in solvents and make the process after synthesis extremely difficult.

**3. Large ionic liquid type counterions.** It has been proved in Chapter 2 that large counterions can help to reduce  $T_g$  and increase ionic conductivity. We have found that cations like phosphonium have negatively charged  $\alpha$  carbons and they effectively screen the positively charged phosphorus center and reduce the interaction with anions. Phosphanzenium is an analog of phosphonium with  $\alpha$  carbons replaced by nitrogens. Since nitrogen is more electronegative than carbon (and much more electronegative than phosphorus), we can expect phosphanzenium would have even more negatively charged  $\alpha$  nitrogens and may further reduce the interaction with anions.

**4. FTIR.** In Chapter 3, FTIR was used to probe the hydrogen bonding condition of both urethane and carbonyl groups. The primary results suggest polyurethane ionomers with different counterions can be distinguished by FTIR and curve resolving will help us to further understand the hydrogen bonding of urethane and carbonyl groups with and without the presence of ionic groups. And unlike metal ions, ionic liquid cations like imidazolium also have absorbance in IR, and this gives us a very good chance to study the interaction between these counterions with the polymer matrix. Rheology and DRS suggest that there is a significant amount of counterions trapped in pPDI-carboxylate-pPDI, so it would be very useful if we can see specific interaction or change in hydrogen bonding through FTIR. It would also be useful to do FTIR on the ions-in-soft-segment samples prepared in Chapter 4 and 5. These samples have sulfonate groups instead of carboxylate groups and is better for understanding the interactions with cations. The sulfonate stretching band shifts when coupled with ions so it provides a good method to study the interaction of the ionic liquid cations. In Chapter 5, we found that samples with stronger SXAS peak show more ions trapped in hard phase in DRS analysis. Since SXAS cannot tell us how large the fraction of the peak is from hard/soft microphase separation, FTIR can be a useful tool to probe if there is different amount of microphase separation between samples prepared by different methods.

**5. TEM, AFM and morphology.** Techniques used in this thesis to probe microphase separation are all indirect methods, which cannot provide a “real picture” of the morphology. To actually see the morphology and the hard and soft phases, AFM and TEM can be useful tools. Both AFM and TEM can show the shape, size and the real distribution of hard phase which is difficult to get from other techniques. AFM is a

common tool to study microphase separation and the resolution is very good so even small hard phase can be seen. The biggest disadvantage is that AFM only characterizes material surface and it is debatable that if the surface morphology is the same with the bulk. TEM with ultramicrotomed samples can provide the information of the bulk materials. However, the contrast between hard and soft phases is usually too low to be seen in bright field images and dyes like RuO<sub>4</sub> or OsO<sub>4</sub> may be necessary. TEM EELS (Electron Energy Loss Spectroscopy) is another powerful tool to study the bulk morphology. By EELS, an element map can be obtained and the distribution of specific atoms can be acquired. So we can see the distribution of sulfur, carbon and nitrogen atoms and find out the correlation if there is sulfonate group trapped in the hard phase or on the interface. From primary results for PU32, no microphase separation was seen in the bright field images but aggregation of sulfur was observed.

**6. Cationic polyurethane ionomers.** Only anionic polyurethane ionomers were synthesized and characterized in this thesis. However, cationic polyurethane ionomers would also be very interesting materials. Ether oxygens in PEG are well known to interact/solvate cations so although this helps cations to leave anions the interactions also slows the cations down. Anions move faster than cations in PEO with dissolved alkali metal salts. By attaching cations on polyurethane, PEG can solvate the cations on the chain and release anions but not slow down these conducting anions. At the same time, it is easier to attach cationic groups on the polymer chain through S<sub>N</sub>2 chemistry and there is a larger variety of cationic groups to choose from: ammonium, phosphonium and imidazolium, etc. There are also large amount of anions can be used as counterions in

cationic polyurethane ionomers like TFSI, triflate,  $\text{BF}_4^-$ ,  $\text{PF}_6^-$  and  $\text{AlCl}_4^-$  and these anions are difficult to be attached on polymers.

## Appendix A

### NMR Spectra of Materials Prepared

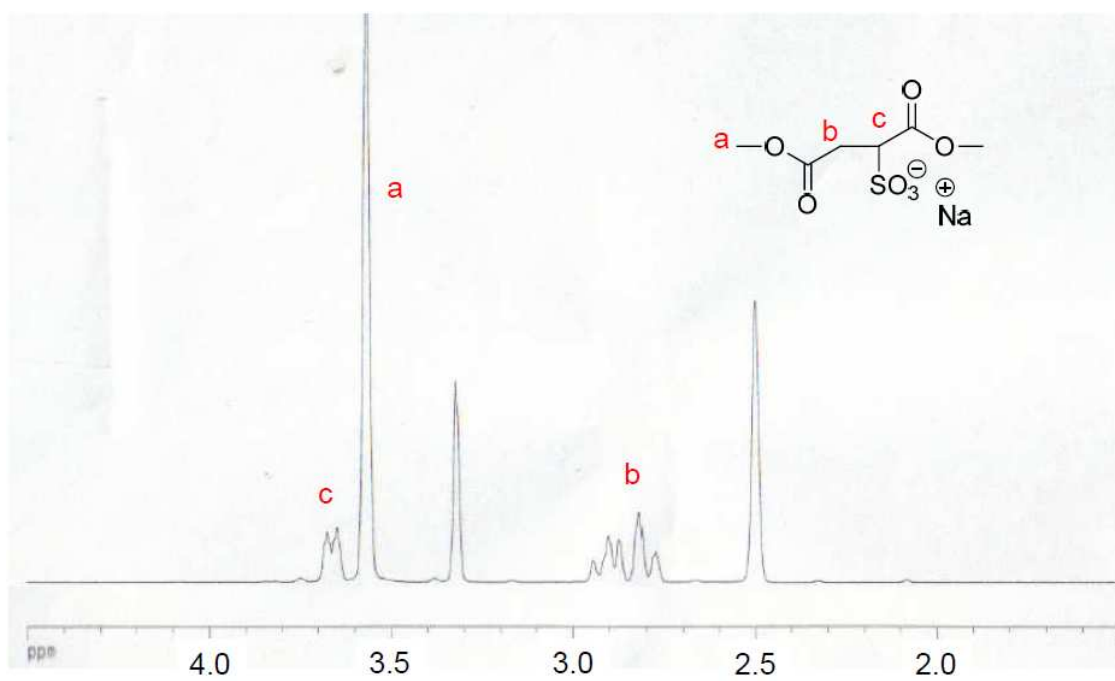


Figure A-1: <sup>1</sup>H-NMR of sulfonated dimethyl fumarate in DMSO-d<sub>6</sub>.

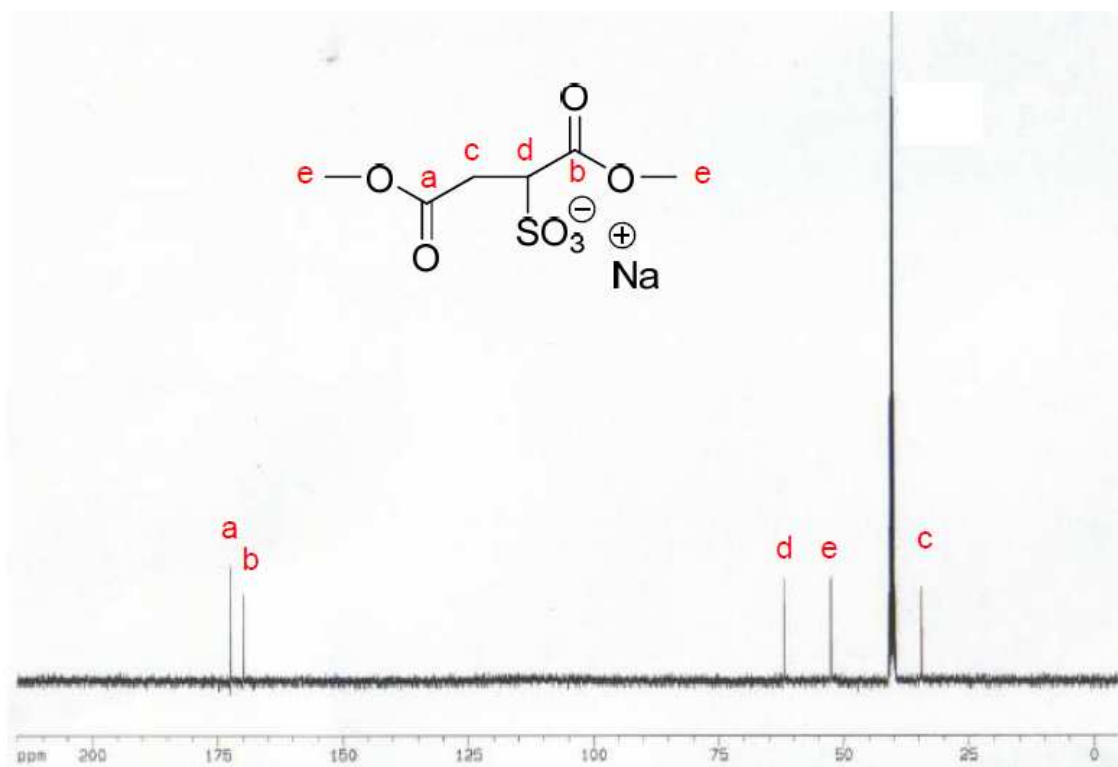


Figure A-2:  $^{13}\text{C}$ -NMR of sulfonated dimethyl fumarate in DMSO- $d_6$ .

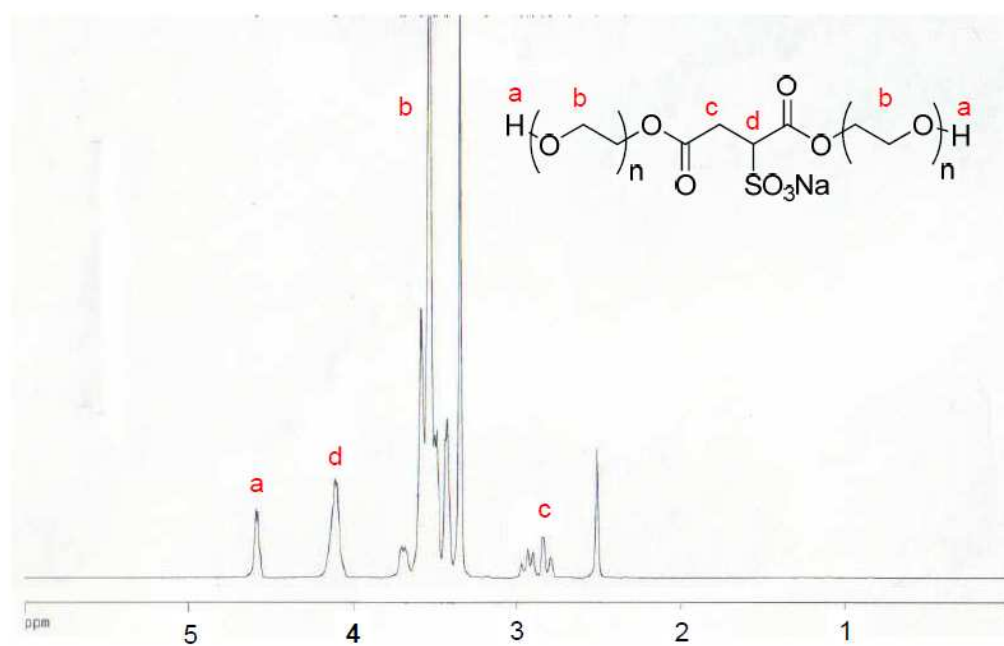


Figure A-3:  $^1\text{H-NMR}$  of SC-diol200 in  $\text{DMSO-d}_6$ .

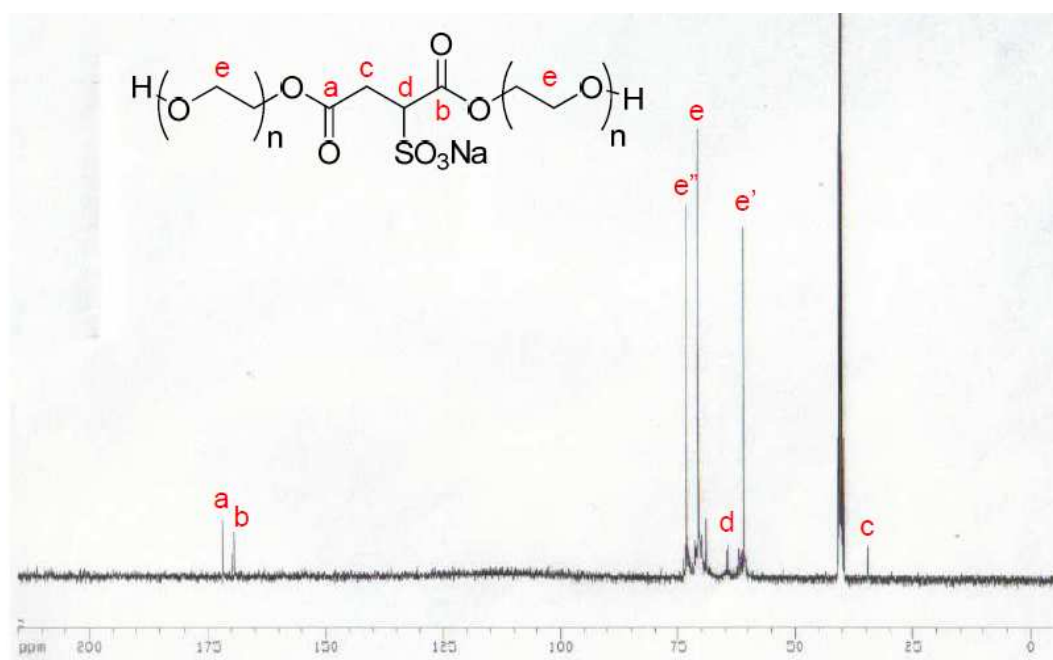


Figure A-4:  $^{13}\text{C-NMR}$  of SC-diol200 in  $\text{DMSO-d}_6$ .

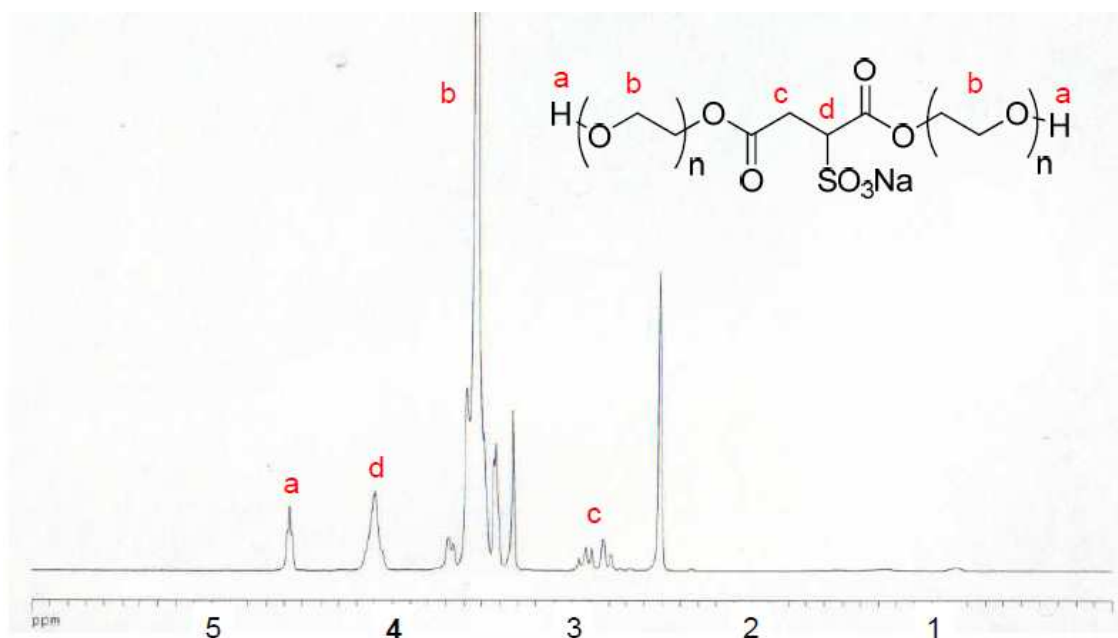


Figure A-5:  $^1\text{H-NMR}$  of SC-diol400 in  $\text{DMSO-d}_6$ .

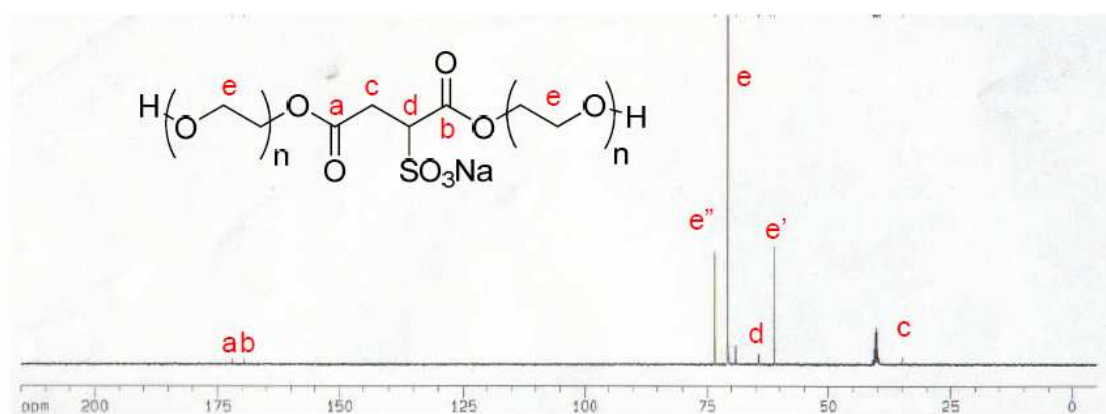


Figure A-6:  $^{13}\text{C-NMR}$  of SC-diol400 in  $\text{DMSO-d}_6$ .

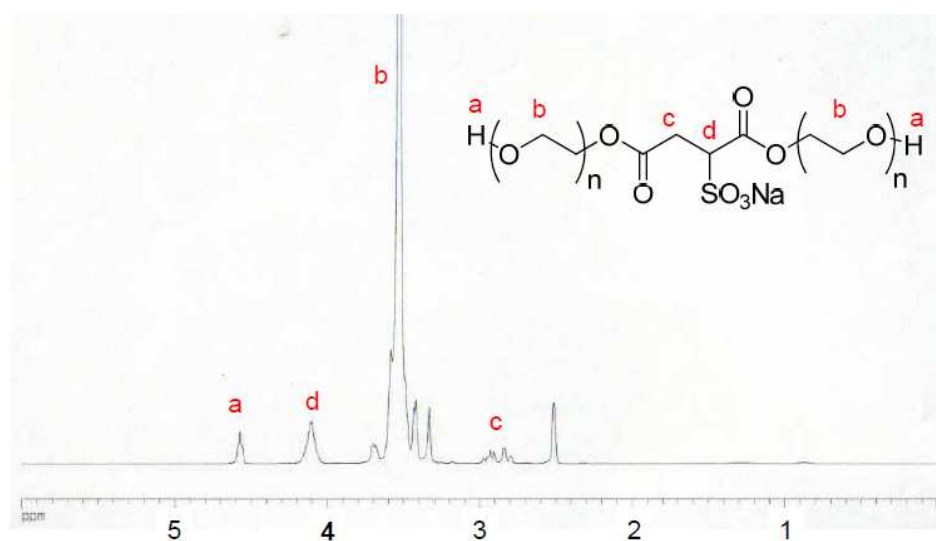


Figure A-7:  $^1\text{H-NMR}$  of SC-diol600 in  $\text{DMSO-d}_6$ .

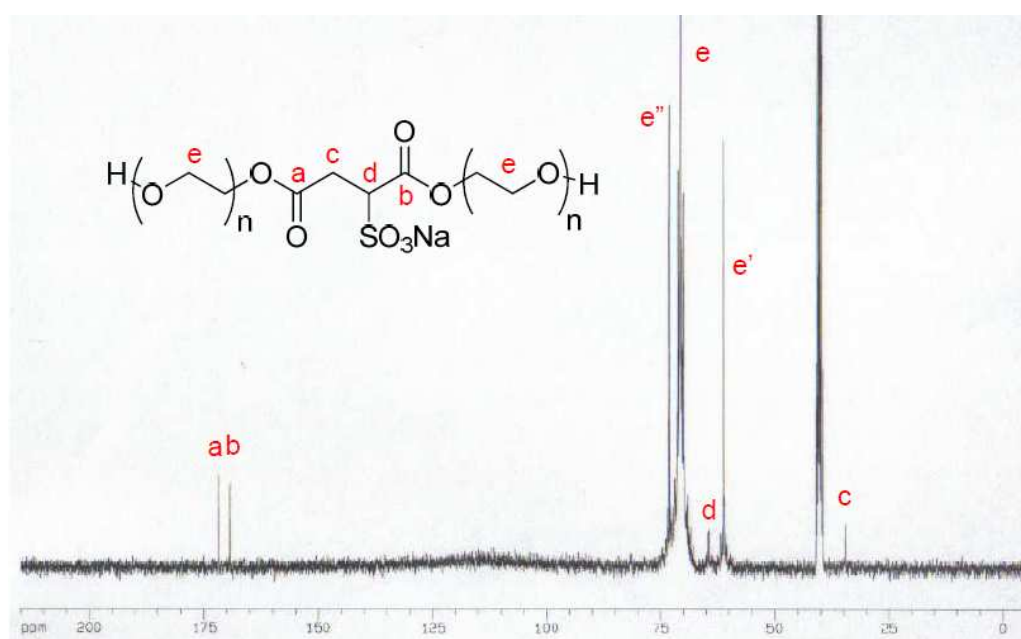


Figure A-8:  $^{13}\text{C-NMR}$  of SC-diol600 in  $\text{DMSO-d}_6$ .

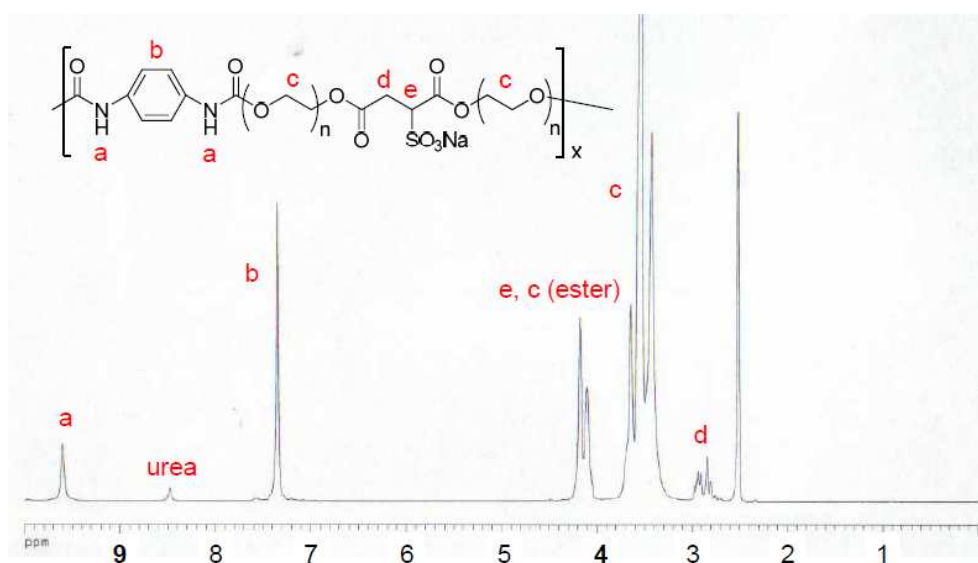


Figure A-9: <sup>1</sup>H-NMR of PU200s in DMSO-d<sub>6</sub>.

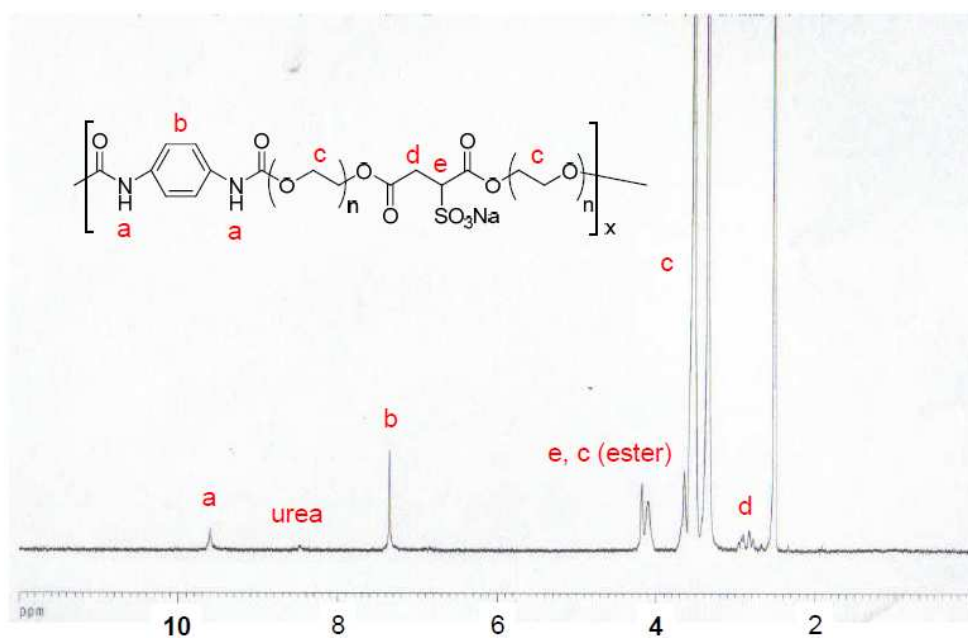


Figure A-10: <sup>1</sup>H-NMR of PU400s in DMSO-d<sub>6</sub>.

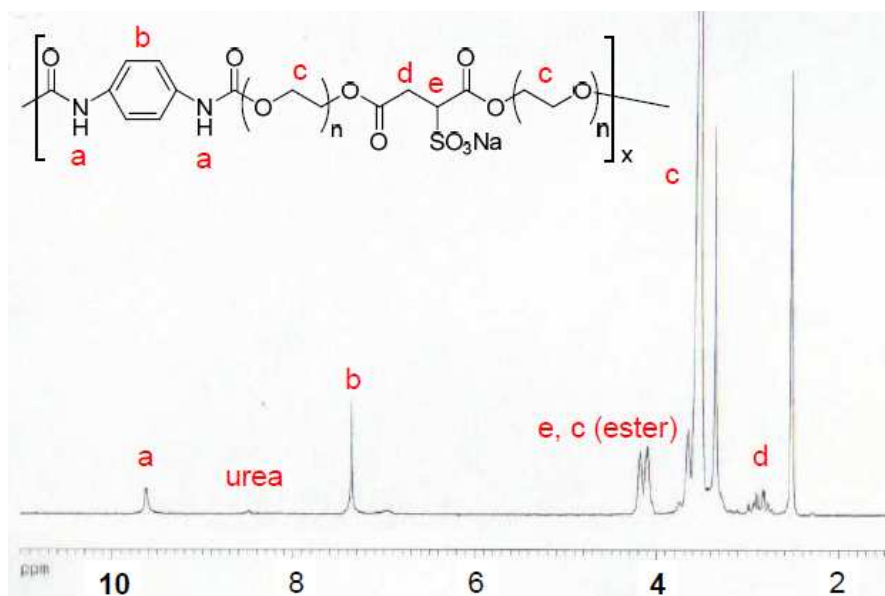


Figure A-11: <sup>1</sup>H-NMR of PU600s/PU10 in DMSO-d<sub>6</sub>.

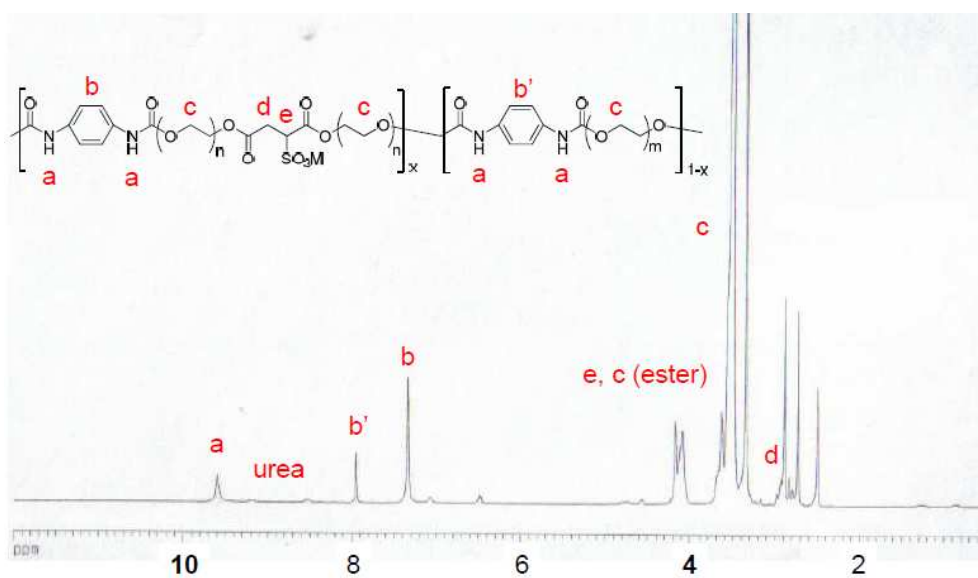


Figure A-12: <sup>1</sup>H-NMR of PU200sd400 in DMSO-d<sub>6</sub>.

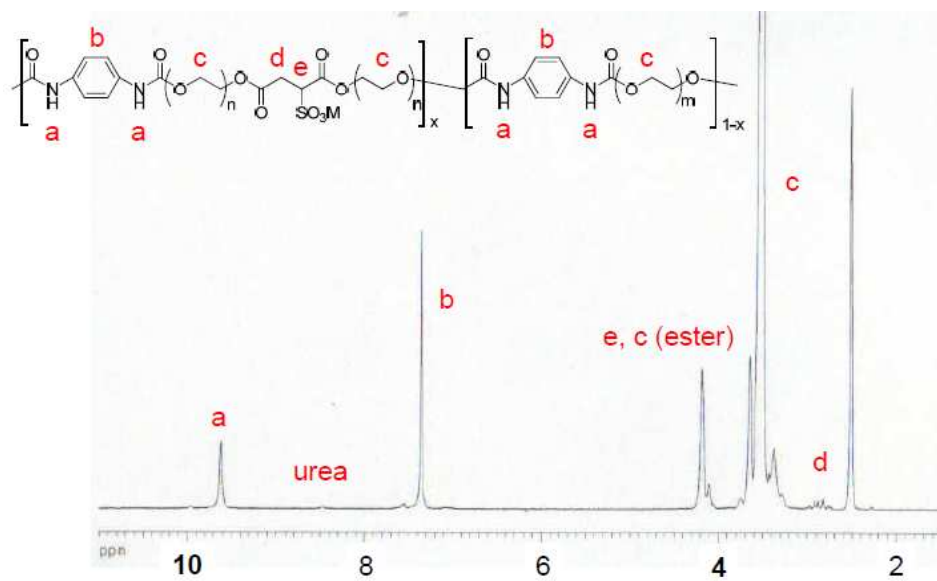


Figure A-13: <sup>1</sup>H-NMR of PU600sd600 in DMSO-d<sub>6</sub>.

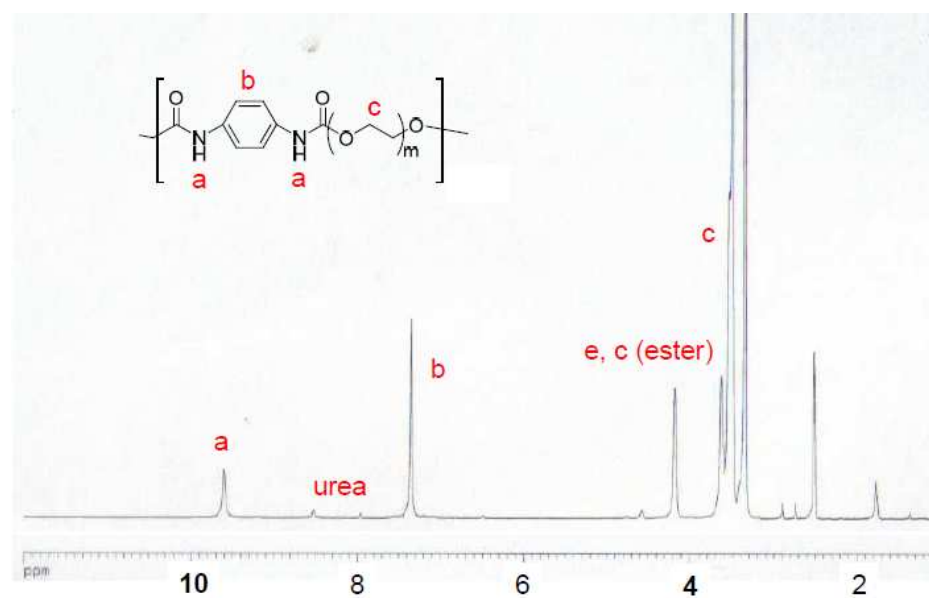


Figure A-14: <sup>1</sup>H-NMR of PUd400 in DMSO-d<sub>6</sub>.

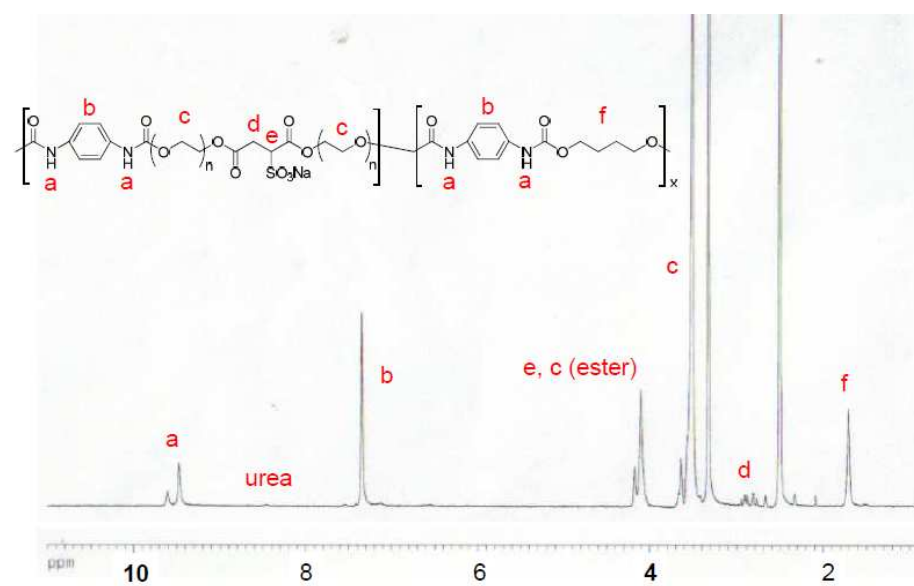


Figure A-15: <sup>1</sup>H-NMR of PU23 in DMSO-d<sub>6</sub>.

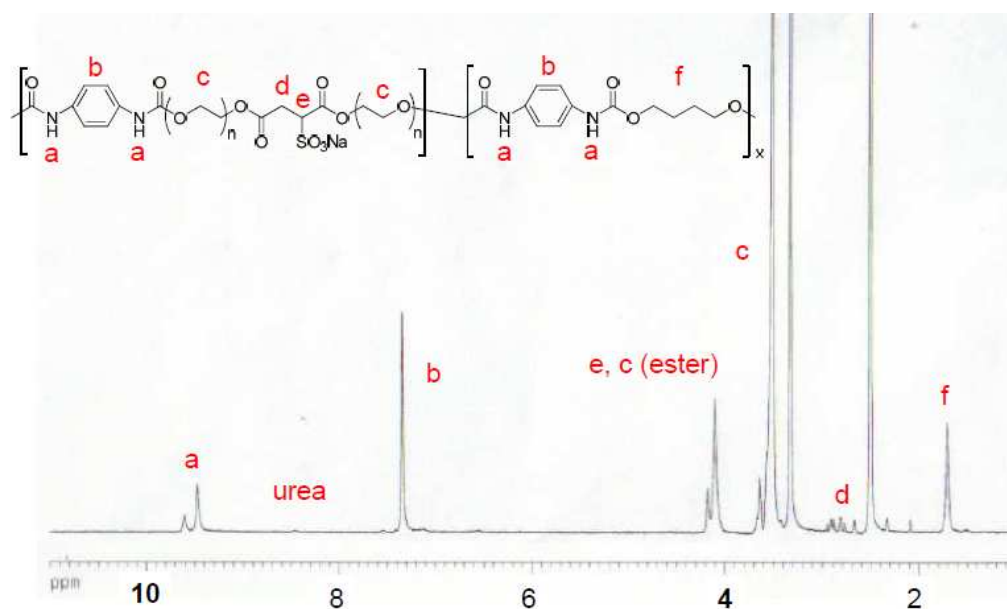


Figure A-16: <sup>1</sup>H-NMR of PU32 in DMSO-d<sub>6</sub>.

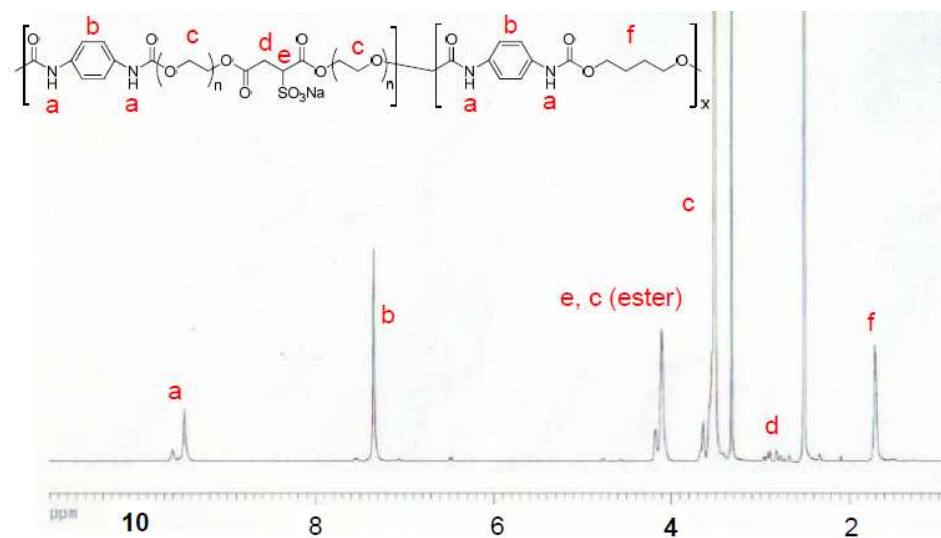


Figure A-17: <sup>1</sup>H-NMR of PU40 in DMSO-d<sub>6</sub>.

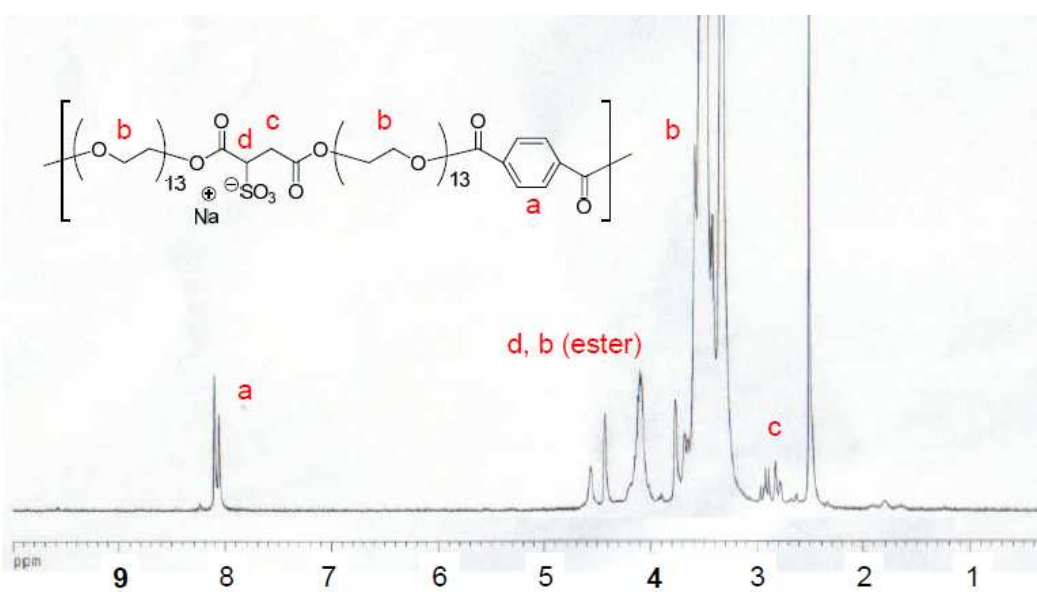


Figure A-18: <sup>1</sup>H-NMR of PE in DMSO-d<sub>6</sub>.

## **VITA**

### **Shih-Wa Wang**

Shih-Wa Wang was born and raised in Taipei, Taiwan. She entered National Taiwan University in 2000 and received her BS degree in Chemical Engineering in 2004. The same year she attended Department of Chemical Engineering in Pennsylvania State University. She earned a master degree in 2007 on the topic of “Development of polymeric nanocarriers for hydrophilic drugs”. In the following years, she was working on understanding the structure-property relationship of polyurethane ionomers with Dr. Ralph Colby. She is currently working in PPG Industry in Pittsburgh, PA.